HETEROGENEOUS CATALYSTS IN AQUEOUS PHASE REFORMING ENVIRONMENTS: AN INVESTIGATION OF MATERIAL STABILITY

A Dissertation
Presented to
The Academic Faculty

by

Ryan M. Ravenelle

In Partial Fulfillment
of the Requirements for the Degree
of Doctor of Philosophy in the
School of Chemical and Biomolecular Engineering

Georgia Institute of Technology
December, 2011

HETEROGENEOUS CATALYSTS IN AQUEOUS PHASE REFORMING ENVIRONMENTS: AN INVESTIGATION OF MATERIAL STABILITY

Approved by:

Dr. John C. Crittenden, Advisor
School of Chemical & Biomolecular Engineering
Georgia Institute of Technology

Dr. Charles Liotta
School of Chemistry & Biochemistry
Georgia Institute of Technology

Dr. Carsten Sievers
School of Chemical & Biomolecular Engineering
Georgia Institute of Technology

Dr. Yongsheng Chen
School of Civil & Environmental Engineering
Georgia Institute of Technology

Dr. Christopher W. Jones
School of Chemical & Biomolecular Engineering
Georgia Institute of Technology

Date Approved: November 11, 2011

To my family and friends who have helped me through this journey more than they can know.

ACKNOWLEDGEMENTS

My deepest thanks go out to my advisor, Dr. John C. Crittenden. Without his support, this achievement would never have been realized. I want to especially express my gratitude for his faith in me early on in graduate school and affording me the unbelievable opportunity to follow him to Georgia Tech. Your knowledge, input and friendship have been invaluable on this journey. I also want to extend sincere thanks to my co-advisor Dr. Carsten Sievers. Your intellectual contributions to my development as a Ph.D. student cannot be recognized with enough gratitude. I want to give special acknowledgement to all of my lab mates and peers, especially John Copeland, Max Hahn, Tobias Tengler and Jared McGrath. Not only have you provided me with research guidance, but you have been outstanding friends. I have no doubt that without your friendship and support I would not be where I am today. I offer my sincerest wishes of luck and success to all of you, though I know you will all accomplish much in your careers. All of my work would not have been possible without the help of countless other people: Johannes Liesen, Mariefel Olarte, Guangxuan Zhu, Fatoumata Diallo just to name a few. The outstanding support from both students and faculty in this department will be forever appreciated.

Lastly, I need to thank my family from the bottom of my heart. To my father, who has been extremely supportive of everything I've done. To my sister, who is the most honest, caring and dedicated person I know. You have been both my friend and role-model. And finally to my mother, to whom I owe so much: I have been so blessed to have you by my side. You have been the crutch that has held me up for so long, and you are the biggest reason I have made it this far. I love you all so much.

TABLE OF CONTENTS

LIST OF TABLES

Page

LIST OF FIGURES

Page

LIST OF SYMBOLS AND ABBREVIATIONS

δ	Chemical Shift
θ	Diffraction Angle
APR	Aqueous Phase Reforming
CLD	Chemical Liquid Deposition
CVD	Chemical Vapor Deposition
EFAL	Extraframework alminum
FTS	Fischer-Tropsch Synthesis
IR	Infrared
MCC	Microcrystalline Cellulose
NMR	Nuclear Magnetic Resonance
NREL	National Renewable Energy Laboratory
PDMS	Poly-dimethylsiloxane
SA	Surface Area
TEOS	Tetraethylorthosilicate
TMOS	Tetramethoxysilane
TOF	Turnover Frequency
TON	Turnover Number
TPD	Temperature Programmed Desorption
XRD	X-Ray Diffraction
WGS	Water-Gas Shift

SUMMARY

The use of fossil fuel derived fuels and chemicals is problematic for a variety of reasons including depletion of known reserves, adverse effects on the environment, and political complications. Lignocellulosic biomass stands as a promising alternative to potentially replace a significant portion of fossil derived resources, and it can be locally grown in a sustainable fashion. In the foreseeable future, biorefineries will compete with traditional refineries that convert fossil feedstocks using mostly heterogeneously catalyzed processes at elevated temperatures. It therefore seems that in order to realistically process biomass on a large scale, it is highly likely that heterogeneous catalysis will play a significant role.

One challenge associated with the processing of lignocellulosic biomass is that it is comprised of oxygen rich carbohydrates, while coal and oil are carbon and hydrogen rich. Carbohydrates are polar molecules which typically have low vapor pressure which in turn makes them difficult to process via gas phase reactions. Therefore, large scale processing will likely take place in liquid phase, and water is a good solvent candidate due to its availability and the polar nature of carbohydrates. However, the presence of high temperature liquid phase water poses many challenges for catalytic processes especially considering that many common catalysts were developed for gas-phase reactions. Of specific interest is the material stability of these catalysts in high temperature aqueous phase environments.

This dissertation aims to investigate the structural integrity of some common catalytic materials under typical biomass reforming conditions. There are 3 main objectives of this study: 1) identify potentially stable candidates from commonly used materials, 2)

understand the mechanism(s) by which these catalysts degrade, 3) design/modify catalysts in an effort to increase their hydrothermal stability.

The first thrust investigates the behavior of zeolites in hot liquid water. Zeolites are aluminosilicate materials with highly ordered porous structures, and are used in many common catalytic upgrading processes (i.e. fluid catalytic cracking). Two framework types, faujasite and ZSM-5, with different Si/Al ratios were subjected to hot water treatment at 200 °C. It was found that the ZSM-5 framework was highly stable over the course of treatment, independent of the Si/Al ratio, which is consistent with its high stability in steaming environments. The stability of faujasite is highly dependent on the Si/Al ratio, where silicon rich materials are less stable. These findings are opposite that of stability trends in steam, and therefore highlight the importance of investigating catalyst degradation in aqueous environments. The integrity of the aluminum rich materials was attributed to the higher number of Si-O-Al bonds which are less susceptible to cleavage than Si-O-Si bonds. It was also found that the addition of lanthanum modifier was effective in increasing hydrothermal stability.

In the second thrust, the hydrothermal stability of γ-Al_2O_3 based catalysts in water at 200 °C are thoroughly investigated, as γ-Al_2O_3 is used as a catalyst support for many aqueous phase reforming reactions. It was found that the alumina support hydrates and undergoes a phase transformation to form crystalline boehmite (AlOOH) with a subsequent loss in surface area and Lewis acid sites. When metal particles are present on the support, the phase change kinetics are slowed. This behavior is attributed to metal particles adsorbed on “basic” surface OH groups, which are presumed to play a key role in the formation of boehmite. It was also observed that as the support crystallized, metal

particles underwent sintering. It is therefore concluded that γ-Al_2O_3 suffers detrimental changes in aqueous phase reforming environments associated with the material phase change, but capping specific surface hydroxyls presents a viable route to increase the hydrothermal stability.

The third thrust examines how metal precursor affects the stability of a γ-Al_2O_3 supported catalyst and in turn what effect this has on a model biomass reaction (aqueous phase conversion of cellulose to sorbitol). It was found that the metal precursor used in catalyst synthesis changes the boehmite formation kinetics and also affects alumina support dissolution. It was demonstrated that dissolved aluminum cations are active for cellulose hydrolysis which is the first step in the formation of sorbitol; therefore, catalyst integrity was shown to directly affect activity for a model biomass reforming reaction. This again highlights the importance of hydrothermal stability as it can influence reaction mechanisms.

The fourth and final thrust aims to stabilize a γ-Al_2O_3 supported catalyst for aqueous phase reforming of sorbitol to produce hydrogen. The information gained from the previous thrusts was used to modify a Pt/γ-Al_2O_3 catalyst. A silicon layer was deposited on the catalyst with two different silicon containing precursors. It was found that these silicon treatments are effective in protecting the catalyst from boehmite formation upon exposure to hot liquid water. The increase in stability is attributed to resilient Si-O-Al linkages and an observed decrease in basic surface hydroxyls which were previously found to play a key role in boehmite formation. In addition to increased stability, the silicon treatments result in stabilization against metal particle sintering and an increase in turnover number for hydrogen production. These results illustrate an effective method of

increasing the hydrothermal stability of a γ-Al_2O_3 supported catalyst for use in aqueous phase reforming reactions. This method may be applicable to other catalyst supports.

CHAPTER 1

INTRODUCTION

1.1 Fossil Fuels and Biomass as a Fuel/Chemical Feedstock

The quality of life enjoyed by those of us fortunate enough to live in developed nations strongly depends on a steady supply of energy. The bulk of this energy, whether for transportation or power and electricity, comes exclusively from fossil fuels including oil, coal and natural gas. Fossil fuels are also the primary feedstock for multiple chemical precursors to synthesize common materials such as plastics and other commodity chemicals. The use of fossil resources presents major problems associated with climate change mainly from the release of greenhouse gases. This is in addition to political complications and national security concerns. Whether one is a skeptic of climate change or not, the fact remains that the fossil fuel supply is limited and world energy demands are steadily rising. Oil accounts for about 40% of the world's primary energy and nearly all of the fuel for the world's transportation sector, and peak oil is commonly thought to be reached within the next 20 years (Table 1.1).[1]

Table 1.1 List of forecasts of global peak oil production.

Author	Year of global peak oil
Hubbert (1956)	1995
Campbell (2003)	2010
Duncan-forecast 1 (2003)	2003
Duncan-forecast 2 (2003)	2006
Duncan-forecast 3 (2003)	2016
Loram (2004)	2024
Hoffman (2005)	2020
Feng et. al. (2006)	2020
Greene et. al. on USGS data (2006)	2023
Greene et. al on Campbell's data (2006)	2006
Motomura (2006)	2015
International Energy Assessment (2008)	2030
Average	2014

The same dilemma applies to coal and natural gas. Data collected from the Annual Energy Review (2007), British Petroleum and the International Energy Outlook (2007) is compiled to illustrate the ratio of world consumption to proven reserves for oil, coal and natural gas from 1980 to 2006 (Figure 1.1).[2]

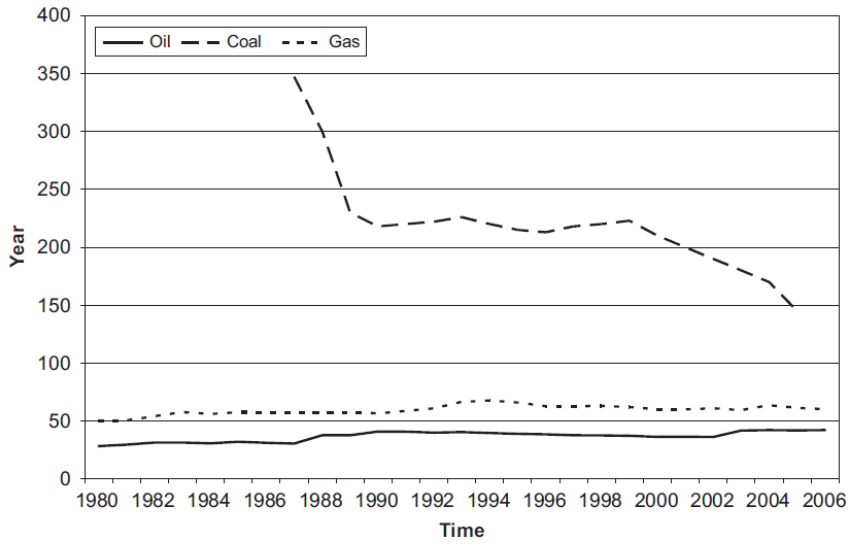

Figure 1.1 The ratios of world consumption to reserves for oil, coal and gas from 1980 to 2006.

From the previous figure, it is seen that the ratios of consumption to known reserves for oil and gas were constant at around 40 and 60 years, respectively. This implies that known reserves of these resources has increased over time to meet projected consumption while coal reserve estimates have decreased. This means that if no new reserves are discovered and world consumption of oil, coal and gas remain at 2006 levels, these supplies will last another 40, 200 and 60 years, respectively.[2] Therefore, the need to find a replacement for fossil fuels is eminent, especially for oil and gas based solely on availability and not on detrimental environmental impacts. This is in addition to many advantages of having domestic clean energy production.

Biomass stands to be an attractive replacement for fossil fuel resources, especially in the transportation fuel sector. Though utilization of biomass for fuels and chemicals may be a promising strategy to mitigate the problems associated with fossil fuel use, it must be done in a sustainable fashion to avoid resource depletion. Conversion of non-edible

biomass (lignocellulosics) is the best strategy for large scale biofuel production to avoid the fuel vs. food complication.

A major distinction between biomass and fossil feedstocks is the high oxygen content in the former. Lignocellulosic biomass is complex in nature, but it is mainly composed of three fractions, namely cellulose, hemicellulose and lignin (Figure 1.2).[3] Cellulose is the most abundant component and is comprised of glucose chains with β-1,4-glycosidic linkages and extensive hydrogen bonding between individual chains. This makes cellulose crystalline in nature and resistant to chemical attack. Hemicellulose resembles cellulose except that instead of exclusively containing glucose units, it contains other six carbon sugars as well as five carbon sugars. Hemicelluloses are more readily hydrolyzed compared to crystalline cellulose. Lignin is a complex polymer comprised of phenol alcohol units with no organized structure. An important step in the utilization of biomass is to find efficient methods to utilize all of the main fractions; however, the work in this dissertation mainly addresses catalytic processes applied to cellulose and oxygenates derived from glucose.

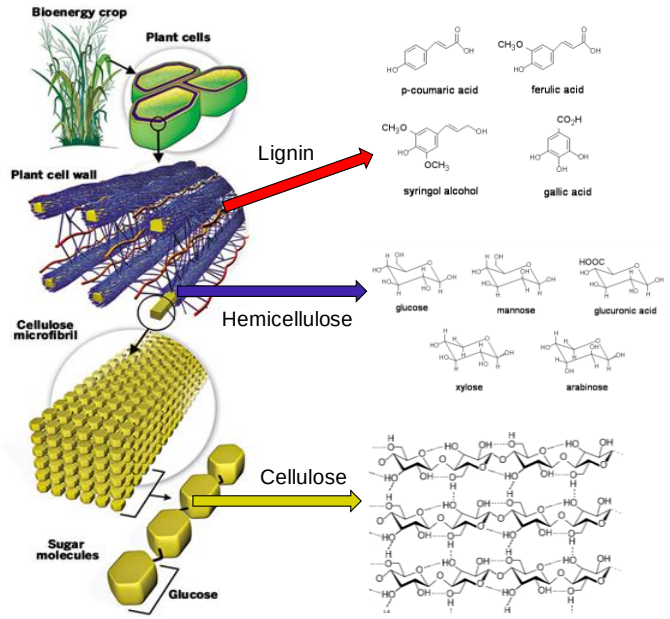

Figure 1.2: Major components of lignocellulosic biomass.

1.2 Heterogeneous Catalysis in Biomass Processing

The use of heterogeneous catalysis is currently widely employed in the petroleum industry to produce liquid fuels and chemicals. Therefore, the concept of using catalytic processing to produce fuels and chemicals from lignocellulosic biomass seems to be a sensible ambition. One of the challenges with biomass is that many of the components found in these feedstocks have relatively low vapor pressures, and sugars and other oxygenates tend to degrade at temperatures lower than their boiling points.[4] Therefore, processes for conversion of carbohydrates will likely take place in liquid phase. In light of this issue, a recent NSF report has concluded that improving liquid-phase processes for biomass-derived compounds is necessary to enable large scale production.[5] Water is the likely solvent of choice because it is cheap, abundant, and readily dissolves polar

oxygenates from biomass including monosaccharides and oligomeric species as well as sugar alcohols (e.g. glycerol, sorbitol).

Possible routes to make biomass derived fuels utilize both chemical and biological catalysts, though chemical catalysts are more common (Figure 1.3).[5]

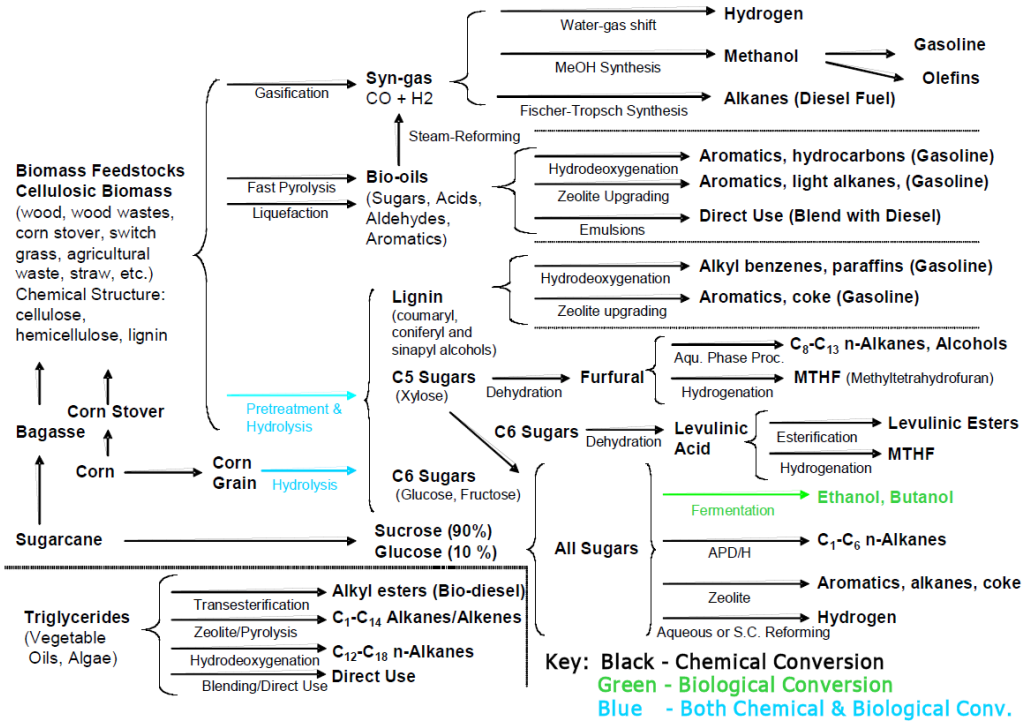

Figure 1.3: Chemically and biologically catalyzed routes to produce fuels from lignocellulosic biomass.

Chemical catalysts can usually operate under harsher conditions compared to biological catalysts leading to reduced residence times, though the latter may have superior selectivity. In addition, biological catalysts are usually more expensive. Chemical catalysts can be in two forms: homogeneous, where the catalyst is in the same phase as the reactants or heterogeneous, where the catalyst is in a different phase. Heterogeneous catalysts have the distinct advantage when it comes to separating them from the desired

products and regenerating them for reuse. Therefore, heterogeneous chemical catalysts seem to represent an attractive option.

As demonstrated in Figure 1.3, there are a variety of chemical catalytic processes that are used in biomass upgrading. There are a few key catalytic reactions that are briefly mentioned as the catalytic materials used are relevant to this dissertation. These processes include hydrolysis, dehydration and hydrogenation. It should be noted that these are typically applied to the cellulose and hemicellulose fractions, as lignin is subjected to other upgrading processes or burned for process heat.

Hydrolysis is the first step to break down the main carbohydrate polymers (cellulose and hemicelluloses) into elementary sugars for further upgrading. This is typically done commercially via hydrolysis by homogeneous liquid acids,[6-8] though these processes suffer the drawback of acid recovery in addition to the need for expensive equipment to avoid corrosion.[9] Therefore, the use of heterogeneous acids (e.g. zeolites) is desirable. Some observations have been made in literature regarding solid acid catalyzed hydrolysis of solid cellulose substrate. Onda et. al. showed hydrolysis of cellulose to glucose with a maximum yield of around 40% over sulfonated activated carbon, which is similar to the yields they observed with dilute sulfuric acid treatment at the same conditions (423 K, 24 hrs) [10]. Suganuma et. al. also demonstrated cellulose hydrolysis to glucose and water soluble β-1,4-glucans (glucose polymers) with amorphous carbon bearing $–SO_3H$, -COOH, and –OH groups.[11] These groups enhance the Brønsted acidity and consequently enhance the activity of these catalysts for hydrolysis. Competing technologies include hydrolysis of cellulose to water soluble sugars in ionic liquids and supercritical water. [12-

[15] However, ionic liquid separation is challenging while supercritical water requires specialized equipment.

Once a concentrated sugar stream is produced by hydrolysis, a variety of catalyzed processes are available for upgrading. Hydroxymethylfurfural (HMF) is produced via the acid-catalyzed dehydration of fructose which is an isomer of glucose. Direct production of HMF from glucose via acid catalysis is difficult due to low isomerization to fructose; however, a mixure of solid acid and base catalysts (Amberlyst-15 & hydrotalcite) has been shown effective for producing HMF from mono- and di-sachharides in *N*,*N*-dimethylformamide.[16] HMF is valuable because it can undergo aqueous phase dehydration/hydrogenation (Pt/SiO_2-Al_2O_3 catalyst) to synthesize liquid alkanes.[17] In addition, HMF can be oxidized to form furan-2,5-dicarboxylic acid (FDCA) which can be used as a replacement for terephthalic acid to produce plastics.[18] Hydrogenation of sugars to form the respective poly-alcohols is also a viable route as these chemicals are used in the food and cosmetic industry, and sugar alcohols can undergo aqueous phase reforming to produce hydrogen and/or alkanes selectively (transition metals on γ-Al_2O_3, SiO_2-Al_2O_3).[19-20] The hydrogenation of glucose to sorbitol has been studied quite extensively, and is typically done with metal oxide supported Pt, Pd or Ru catalysts or Raney Nickel type catalysts.[21-22]

There are a host of other useful chemicals that can be produced via heterogeneously catalyzed conversion of biomass. In 2004, the National Renewable Energy Laboratory (NREL) released a list of 12 potential biomass based platform chemicals that can act as building blocks for useful molecules.[23] These sugar based building blocks are 1,4-diacids (succinic, fumaric, malic), furan-2,5-carboxylic acid, 3-hydroxypropionic acid, aspartic

acid, glucaric acid, glutamic acid, itaconic acid, levulinic acid, 3-hydroxybutyrolactone, glycerol, sorbitol, and xylitol/arabinatol.

The purpose of section 1.2 is not to be a detailed overview of all catalytic processes being researched for biomass upgrading. Excellent reviews of this nature are available in the literature.[24-27] However, the goal is to illustrate that the field is rapidly expanding with many opportunities to produce key platform chemicals from biomass. It is also important to note than many of the processes to date utilize very similar catalytic materials including transition metals supported on carbons, solid acids and metal oxides and these materials will likely be considered in future investigations.

1.3 Relevance of Catalyst Stability Studies

As the search for new catalysts and catalytic processes continues, it can be easy to overlook simple yet important issues such as material durability while focusing only on yields. Of the multiple catalytic processes discussed in section 1.2, many take place in aqueous phase. While many publications have reported remarkable reactivity of solid catalysts in water, little is known about their stability in aqueous media at temperatures above 100 °C. A recent US-DOE report identified the need for catalysts that are stable under these conditions as one of the key challenges for the development of economical processes for biofuel production.[28]

The use of aqueous media imposes new requirements on the stability of heterogeneous catalysts that were typically developed for use in gas phase reaction. However, only few publications have addressed the stability of solid catalysts and supports under conditions that are relevant for biomass reforming.[29-30] Therefore, the purpose of the current research is to investigate catalyst material stability at conditions that are relevant to biomass

reforming processes in an effort to learn how quickly and by what mechanisms catalysts can degrade in solution.

In Chapter 2, two common solid acids (zeolites ZSM-5 and Faujasite) are hydrothermally treated and the materials analyzed as a function of time to measure structural changes. This investigation is unique in that few publications have considered the stability of zeolites in liquid medium, though many have focused on steaming effect. The mechanism of structural degradation in liquid water is discussed as well as the effects of Si/Al ratio, framework type and incorporation of lanthanum dopant.

In Chapter 3, a similar study is performed on γ-Al_2O_3 based catalysts as this material is one of the most widely used supports. The structural changes of the support and the fate of metal particles in the catalyst are investigated in an effort to understand how γ-Al_2O_3 degrades in water and the subsequent impact on catalyst activity. The focus of Chapter 4 is to investigate how the degradation of γ-Al_2O_3 can contribute to potential mechanistic effects. The effect of metal precursor salt on dissolution behavior as well as point of zero charge in solution is examined, and these attributes are related to activity for aqueous phase production of sorbitol from cellulose.

Chapter 5 focuses on stabilization of γ-Al_2O_3 catalysts via a post-synthesis surface silylation procedure. This method is chosen in light of conclusions based on the previous chapters. Two different silicon precursors at different weight loadings are examined for both impact on hydrothermal stability and activity for aqueous phase production of hydrogen from sorbitol.

In Chapter 6, the final conclusions of the dissertation are presented along with recommendations for future work. The potential impact of this work on the field is discussed along with how the current studies may be applied to other materials.

1.4 References

[1] Aftabuzzaman, M.; Mazloumi, E. *Transport Policy* **2011**, *18*, 695-702.

[2] Shafiee, S.; Topal, E. *Energy Policy* **2009**, *37*, 181-189.

[3] Ritter, S. K. Calling All Chemists; Chemical & Engineering News, **2008**.

[4] Yan, W.; Suppes, G. J. *Journal Of Chemical And Engineering Data* **2008**, *53*, 2033-2040.

[5] Huber, G. W. "NSF, 2008. *Breaking the Chemical and Engineering Barriers to Lignocellulosic Biofuels: Next Generation Hydrocarbon Biorefineries.*," National Science Foundation, **2008**.

[6] Fagan, R. D.; Grethlein, H. E.; Converse, A. O.; Porteous, A. *Environmental Science & Technology* **1971**, *5*, 545-547.

[7] Calvini, P.; Gorassini, A.; Merlani, A. *Cellulose* **2008**, *15*, 193-203.

[8] W. Qi; S. Zhang; Q. Xu; H. Li; Z. Ren; T. Li; Y. Yan *Chemical Engineering & Technology* **2009**, *32*, 534-540.

[9] Rinaldi, R.; Schüth, F. *ChemSusChem* **2009**, *2*, 1096-1107.

[10] Onda, A.; Ochi, T.; Yanagisawa, K. *Topics in Catalysis* **2009**, *52*, 801-807.

[11] Suganuma, S.; Nakajima, K.; Kitano, M.; Yamaguchi, D.; Kato, H.; Hayashi, S.; , M. H. *Journal of the American Chemical Society* **2008**, *130*, 12787-12793.

[12] Sasaki, M.; Adschiri, T.; Arai, K. *AIChE Journal* **2004**, *50*, 10.

[13] Swatloski, R. P.; Spear, S. K.; Holbrey, J. D.; Rogers, R. D. *Journal of the American Chemical Society* **2002**, *124*, 4974-4975.

[14] Roberto Rinaldi, R. P., Ferdi Schüth, *Angewandte Chemie International Edition* **2008**, *47*, 8047-8050.

[15] Sievers, C.; Valenzuela-Olarte, M. B.; Marzialetti, T.; Musin, I.; Agrawal, P. K.; Jones, C. W. *Industrial & Engineering Chemistry Research* **2009**, *48*, 1277-1286.

[16] Takagaki, A.; Ohara, M.; Nishimura, S.; Ebitani, K. *Chemical Communications* **2009**, 6276-6278.

[17] Huber, G. W.; Chheda, J. N.; Barrett, C. J.; Dumesic, J. A. *Science* **2005**, *308*, 1446-1450.

[18] Kamm, B. *Angewandte Chemie International Edition* **2007**, *46*, 5056-5058.

[19] Huber, G. W.; Cortright, R. D.; Dumesic, J. A. *Angewandte Chemie - International Edition* **2004**, *43*, 1549-1551.

[20] Huber, G. W.; Dumesic, J. A. *Catalysis Today* **2006**, *111*, 119-132.

[21] Crezee, E.; Hoffer, B. W.; Berger, R. J.; Makkee, M.; Kapteijn, F.; Moulijn, J. A. *Applied Catalysis A: General* **2003**, *251*, 1-17.

[22] Castoldi, M.; Câmara, L.; Monteiro, R.; Constantino, A.; Camacho, L.; de Carneiro, J.; Aranda, D. *Reaction Kinetics and Catalysis Letters* **2007**, *91*, 341-352.

[23] Werpy, T.; Peterson, G. Top Value Added Chemicals from Biomass; Laboratory, N. R. E., Ed., **2004**.

[24] Juben N. Chheda, George W. H., James A. Dumesic, *Angewandte Chemie International Edition* **2007**, *46*, 7164-7183.

[25] Huber, G. W.; Iborra, S.; Corma, A. *Chemical Reviews* **2006**, *106*, 4044-4098.

[26] Corma, A.; Iborra, S.; Velty, A. *Chemical Reviews* **2007**, *107*, 2411-2502.

[27] MÃ¤ki-Arvela, P. i.; Holmbom, B.; Salmi, T.; Murzin, D. Y. *Catalysis Reviews* **2007**, *49*, 197 - 340.

[28] Bell, A. T.; Gates, B. C.; Ray, D. "Catalysis for Energy," DOE BES report, **2008**.

[29] Ravenelle, R. M.; Schüβler, F.; D'Amico, A.; Danilina, N.; van Bokhoven, J. A.; Lercher, J. A.; Jones, C. W.; Sievers, C. *The Journal of Physical Chemistry C* **2010**, *114*, 19582-19595.

[30] Li, H.; Xu, Y.; Gao, C.; Zhao, Y. *Catalysis Today* **2010**, *158*, 475-480.

CHAPTER 2

ZEOLITES

2.1 Background

2.1.1 Zeolite Structure and Use: Faujasite and ZSM-5

Zeolites are attractive catalysts because they have a well defined structure, large surface area, and can be produced at a reasonable price. The primary building blocks of zeolites are tetrahedra with silicon or aluminum atoms in the center and oxygen atoms in the corners.[1] These tetrahedra can be combined into a variety of framework structures. Approximately 200 different zeolite structures have been synthesized to date.[2]

Zeolites play a key role in many petroleum upgrading processes. Most zeolites contain charge compensating cations that can function as Brønsted or Lewis acid sites.[1,3] In particular, the Brønsted acid proton form is often used in industry, for example in fluid catalytic cracking units.[3-4] The ability to tailor the acid functionality and pore size of zeolites makes them excellent not only for catalysts and catalyst supports, but also as sorbents.

Two commonly used zeolites are faujasite, or zeolite Y, and ZSM-5. A list of all of the catalytic operations performed by these materials would be quite exhaustive, and so only a few are briefly mentioned. Faujasite is a fluid catalytic cracking catalyst and is also used as a support for Fe and Cu for use in Fischer-Tropsch synthesis.[5] It is considered a large pore zeolite with 12 member ring pores 7.4Å in diameter (Figure 2.1A).[6]

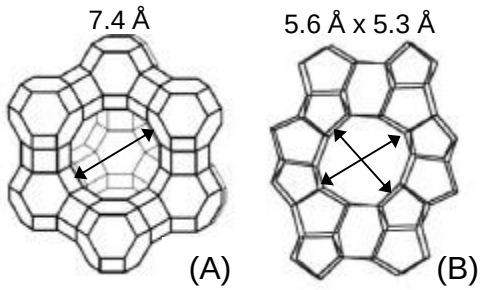

Figure 2.1: Pore geometries of faujasite (A) and ZSM-5 (B) zeolites.

ZSM-5 is a medium pore zeolite and has 10 member ring channels with dimensions of 5.6 x 5.3Å.[6] While ZSM-5 zeolites are useful in cracking and hydrocracking, they are also widely used in other processes including isomerization of n-parrafins and napthenes, reforming, alkylation, and disproportionation of aromatics.[5]

As previously mentioned, the acidic character of these materials is one of the key components of their catalytic activity. For this reason, they stand as attractive alternatives to homogeneous acid in aqueous phase media for a variety of reactions including hydrolysis and dehydration reactions.

2.1.2 Zeolite Hydrothermal Stability

Due to the conditions in typical refining processes, the hydrothermal stability of zeolites is a concern, and modifications of zeolites by steaming have been investigated in numerous publications.[7-10] In the presence of steam, framework aluminum atoms can be removed from the zeolite lattice. This results in the formation of a defect site – a so-called "silanol nest." The "silanol nests" are "healed" by incorporation of silicon atoms that are released by partial collapse of the zeolite framework, which results in the formation of mesopores.[7-8] The aluminum atoms that are removed from the framework

form so-called extraframework aluminum (EFAl) species, which have been associated with the observation of octahedrally coordinated aluminum by ^{27}Al MAS NMR spectroscopy.[11] There is an ongoing debate regarding the fate of these aluminum atoms.[12] It has been suggested that they form a separate alumina phase outside the crystal.[12-13] Alternatively, it was proposed that they are present as isolated charge compensating cations in the zeolite cages.[7,13] It was also shown that some octahedrally coordinated EFAl species can be reintroduced into the zeolite lattice by treatment with bases.[14-15] The degree to which zeolites are affected by steaming increases with increasing Al content.[16] The presence of EFAl leads to improved hydrothermal stability and increased Lewis acidity. Moreover, enhanced catalytic activity was reported for reactions that require strong Brønsted acid sites (e.g. cracking), although the way in which these reactions are promoted remains unclear.[7,17] Similar effects were reported upon introduction of rare earth cations (e.g. La^{3+}) by ion exchange.[17-18] While steaming under well controlled conditions is an important tool for post-synthesis modifications of zeolites, harsh conditions (high temperature, high partial pressure of water) lead to complete destruction of the zeolite.

In contrast to the considerable number of publications on hydrothermal stability in the presence of steam, little work has been published on the behavior of zeolites in hot liquid water.[19-20] However, related studies were performed on mesoporous materials. Incorporation of aluminum into MCM-41[21-23] and MCM-48[23-24] increased the stability of these materials in boiling water (at ambient pressure). A maximum in stability was observed at a certain aluminum content, which was small for MCM-41 (Si/Al = 40.1) and larger for MCM-48 (Si/Al = 8-15). For MCM-48, it was suggested that an increasing

number of Si-O-Al bonds prevents decomposition of the material by hydrolysis, whereas a high aluminum concentration lowers the stability of the framework.[24]

In this chapter, the stability of zeolites in hot liquid water is investigated. These conditions affect zeolites in a way that is different from the effect of steaming. The framework type and the Si/Al ratio have a pronounced influence on the stability. The degradation pathway is elucidated by characterization of zeolite samples after different treatment times.

2.2 Materials and Methods

Zeolites with different Si/Al ratios were obtained from Zeolyst. The material specifications and sample codes are shown in Table 2.1.

Table 2.1: List of zeolite material specifications and codes.

Zeolyst ID	Zeolite Type	Si/Al	Na content / wt%	Sample Code
CBV 712	Y (FAU)	5[a]	0.04	Y5
Prepared by La exchange of CBV 712	Y (FAU)	5[a]	0.04	LaY5
CBV 720	Y (FAU)	14[a]	0.02	Y14
CBV 780	Y (FAU)	41[a]	0.02	Y41
CBV 3024E	ZSM-5 (MFI)	15[b]	0.04	ZSM5-15
CBV 5524G	ZSM-5 (MFI)	25[b]	0.04	ZSM5-25
CBV 8014	ZSM-5 (MFI)	40[b]	0.04	ZSM5-40

[a] Measured by AAS, [b] Determined by the manufacturer

All materials were received in their proton or ammonium form with residual sodium cations on less than 2% of the cationic sites. The lanthanum-exchanged sample, LaY5, was prepared from Y5 by ion exchange with 0.2 M $La(NO_3)_3$ solution. Two ion exchange steps were performed at 80 °C for 2 h using a solution-to-zeolite ratio of 11 $ml \cdot g^{-1}$. After the second ion exchange step, the zeolite was thoroughly washed with bidistilled water and dried at room temperature. All zeolites were calcined under flowing ultra zero purity air (Airgas) at one SLPM in a box furnace prior to aqueous treatments. The temperature was ramped from room temperature to 120 °C (1 $K \cdot min^{-1}$) then held for two hours. The temperature was then ramped to 500 °C (1 $K \cdot min^{-1}$) and held for four hours after which it was allowed to cool. During this treatment the ammonium form of zeolite is converted into the proton form. In case of LaY5, the final calcination temperature was 450 °C.

2.2.1 Stability Tests

For the stability studies, 1 g of the zeolite was suspended in 20 ml of distilled water. Each mixture was poured in an autoclave with a Teflon liner, which was placed in a preheated oven at 150 or 200 °C under constant agitation. Note that at these temperatures, the vapor pressure of water is approximately 5 and 17 bar, respectively.[25] It is therefore safe to assume that the treatments occur in liquid phase. After a specific heating time, the reaction was quenched by placing the autoclave in an ice bath. The mixture was filtered (0.2 μm Nylon filter) and the modified zeolite was washed with distilled water. The samples were dried in air at room temperature for 16 h prior to analysis to remove physisorbed water so that they could be analyzed as solids rather than slurries.

2.2.2 Elemental Analysis

For atomic absorption spectroscopy (AAS) measurements, 20-40 mg of the zeolite sample were dissolved in 0.5 ml of hydrofluoric acid (48%) and heated to 70 °C until the entire liquid had evaporated. An aqueous solution of the residue was analyzed using a UNICAM 939 atomic absorption spectrometer.

2.2.3 XRD

Powder X-ray diffraction (XRD) patterns were measured on a Philips X'pert diffractometer equipped with an X'celerator module using Cu Kα radiation. Diffractograms were obtained from $2\theta = 5$ to 75° with a step size of 0.033°. The relative crystallinity of faujasite samples was determined based on comparing eight peak intensities according to ASTM method D3906, where the untreated samples were assumed to be 100% crystalline.[26]

2.2.4 Scanning Electron Microscopy

Field Emission Scanning Electron Microscopy (FE-SEM) images were obtained using a JEOL LEO-1530 at a landing energy of 10kV and 9 mm of working distance using 'In Lens' detector mode. The powder samples were spread on a carbon coated sample mount and gold-coated to prevent surface charging effects.

2.2.5 Argon Physisorption

The pore volume distribution was determined by argon physisorption at -186 °C using a Micromeritics ASAP 2420 with micropore option. The treated zeolites were evacuated at 375 °C for 8 h prior to analysis. The pore volume was determined using non-local

density functional theory (NLDFT) calculations for argon on oxides with cylindrical pore geometry.

2.2.6 Solid-State NMR Spectroscopy

NMR measurements were performed on fully hydrated samples. ^{27}Al MAS NMR measurements were performed on a Bruker DSC 400 spectrometer. The samples were packed into a 4 mm zirconia rotor and spun at 12 kHz. The resonance frequency for ^{27}Al was 104.2 MHz. A $\pi/12$ pulse was used for excitation and the recycling delay was 250 ms. For each spectrum, a minimum of 2400 scans were accumulated. Solid $Al(NO_3)_3$ was used as a reference compound (δ = -0.543 ppm). ^{27}Al MQMAS NMR experiments were carried out on a Bruker Avance 700 NMR spectrometer using a 2.5 mm double-resonance probe. The resonance frequency for ^{27}Al was 182.4 MHz. The length of the creation pulse and the first conversion pulse were 4.2 and 2.4 μs, respectively. The central transition selective soft $\pi/2$ pulse was 6 μs. A 2D Fourier transformation followed by shearing gave a pure absorption mode 2D contour plot, where the one-dimensional projection of the 2D contour plot on the F1 axis gives the isotropic spectra. All spectra were obtained at a spinning speed of 15 kHz and had a recycle delay of 1.0 s. The ^{27}Al chemical shifts were referenced to Alum, $(NH_4)Al(SO_4)_2 \cdot 12H_2O$. ^{29}Si MAS NMR measurements were performed on a Bruker DSX 300 spectrometer at a resonance frequency of 59.6 MHz for ^{29}Si. The samples were spun at 5 kHz and referenced against the sodium salt of 3-trimethylsilyl-1-propanesulfonic acid (δ = 0 ppm). The concentration of different Al species was obtained by peak fitting of the ^{27}Al MAS NMR spectra. The quadrupolar-induced shift was obtained from the ^{27}Al MQMAS NMR spectra.

2.2.7 Temperature-Programmed Desorption of Ammonia

The concentration of acid sites was determined by temperature-programmed desorption of ammonia in a six-fold reactor setup. The samples were granulated into particles between 500 and 700 μm. After activation in vacuum ($p = 10^{-3}$ mbar) at 450 °C for 1 h (heating rate 10 $K \cdot min^{-1}$), ammonia was adsorbed at 100 °C (p = 1 mbar) for 1 h. Outgassing of physisorbed ammonia occurred for 2 h. The desorption signal $m/z^+ = 16$ was monitored from 100 °C to 770 °C (heating rate 10 $K \cdot min^{-1}$) with a Pfeiffer QMS 200 mass spectrometer. The acid site concentration was calculated by normalization to the dry sample weight and comparison to a standard MFI material (Si/Al = 90, 360 μmol acid $sites \cdot g^{-1}$).

2.2.8 Pyridine Adsorption Followed by IR Spectroscopy

The nature and concentration of acid sites was also analyzed by adsorption of pyridine followed by IR spectroscopy. For this purpose, the samples were pressed into self-supporting wafers and activated in vacuum at 450 °C for 1 h. A heating rate of 10 $K \cdot min^{-1}$ was used. Pyridine was adsorbed at 150 °C with a pressure of 0.1 mbar until no changes were observed in the spectrum (approximately 20 min). After outgassing for 1 h (to remove weakly physisorbed pyridine), a spectrum was recorded. This spectrum was used to determine the total concentration of Brønsted and Lewis acid sites. The strength of the acid sites was probed by increasing the temperature to 450 °C for 1 h. Acid sites that retained pyridine under these conditions were classified as strong acid sites. The concentration of Brønsted and Lewis acid sites was determined based on the integrals of the IR bands at 1540 cm^{-1} (characteristic for pyridinium ions) and 1450 cm^{-1} (characteristic for pyridine adsorbed on Lewis acid sites). For quantification, molar

integral extinction coefficients of 0.73 and 0.96 were used for Brønsted and Lewis acid sites, respectively. These were determined for a reference material using a combination of IR spectroscopy of adsorbed pyridine and micrograviметric measurements of the thermal stability of pyridine.[27]

2.3 Results

2.3.1 AAS

The Si/Al ratio of Y41 increased slightly from 40.7 to 41.5 over 6 h at 200 °C, whereas a ratio of 40.6 was measured after 6 h at 150 °C. In case of Y14, the Si/Al ratio decreased from 14.3 to 13.4 during treatment at 200 °C for 6 h indicating that more silicon than aluminum might have been removed from the sample. The Si/Al ratio of Y5 decreased from 5.4 to 4.9 during 6 h at 200 °C. Note that all of these changes are within the error margin of the measurements.

2.3.2 XRD

The diffractograms of the untreated Y zeolites were as expected, with the major reflections located at $2\theta = 6.3°$, 10.3°, and 15.9° corresponding to the (111), (220), and (331) lattice planes, respectively (Figure 2.2a).[28] The untreated ZSM-5 samples also showed the expected reflections at $2\theta = 7.9°$, 8.9°, and 23.1° corresponding to the (011), (200), and (051) lattice planes, respectively (Figure 2.5a).[28]

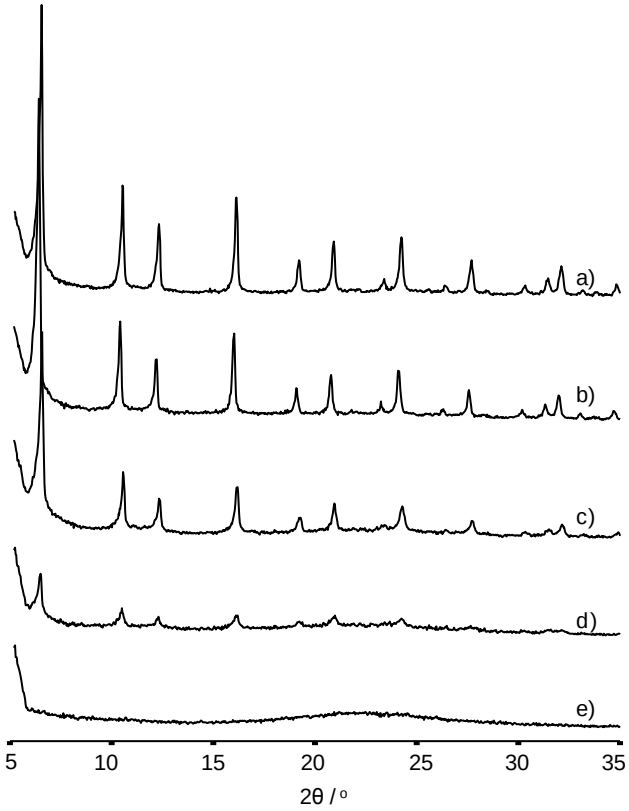

Figure 2.2: X-ray diffractograms of zeolite Y41 treated at 200 °C: a) untreated, b) 1 h, c) 2 h, d) 4 h, e) 6 h.

When Y41 was treated at 200 °C, the intensity of all reflections decreased over time indicating a decrease in crystallinity (Figures 2.2 and 2.3).

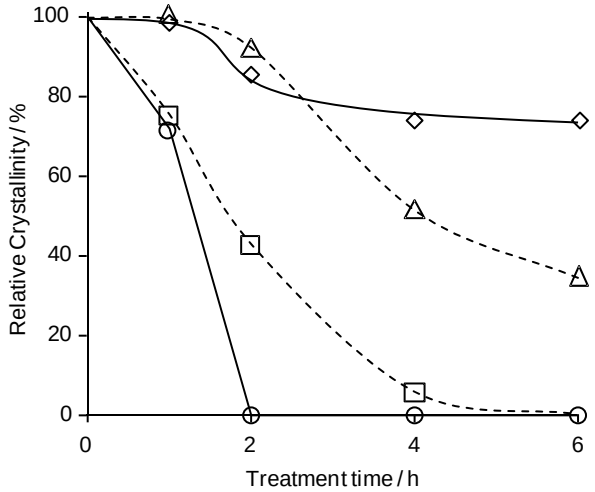

Figure 2.3: Relative crystallinity of zeolite Y41 treated at 150 °C (○) and 200 °C (□) and Y14 treated at 150 °C (◊) and 200 °C (Δ).

The reflections also increased in width, which suggests a decreasing crystallite size.[29] The relative crystallinity decreased linearly over the first 4 h, and after 6 h, the sharp reflections had disappeared and only a broad signal, centered at $2\theta = 22°$, was found. These observations are attributed to the conversion of the crystalline zeolite into an amorphous phase. Treating Y41 at 150 °C resulted in a relative crystallinity of 72% after 1 h followed by complete loss of the crystalline signature after only 2 h, while the broad amorphous signal remained throughout the remainder of the treatment (Figure A.1).

The intensity of the XRD peaks also decreased when Y14 was treated at 200 °C, and the peaks broadened (Figures 2.3 and A.2). After 2 h, the relative crystallinity was 93%. It dropped to 51% and 35% after 4 and 6 h, respectively (Figure 2.3). In contrast to Y41, the peaks were still clearly observable after 6 h indicating that a part of the crystalline structure endured the entire treatment. A broad peak, similar to the one observed for Y41 was observed upon closer inspection of the diffractograms. The relative crystallinity of Y14 decreased to 86% in the first 2 h of treatment at 150 °C. After 4 h, it had a relative crystallinity of 74%, which remained constant throughout the rest of the treatment (Figures 2.3 and A.3).

Zeolite Y5 exhibited an increase in the relative crystallinity after the first hour of treatment at both temperatures. The material retained a relative crystallinity of 78% and 66% after 6 h of treatment at 150 °C and 200 °C respectively, which were both higher as compared to the Y14 zeolite samples (Figures 2.3 and 2.4).

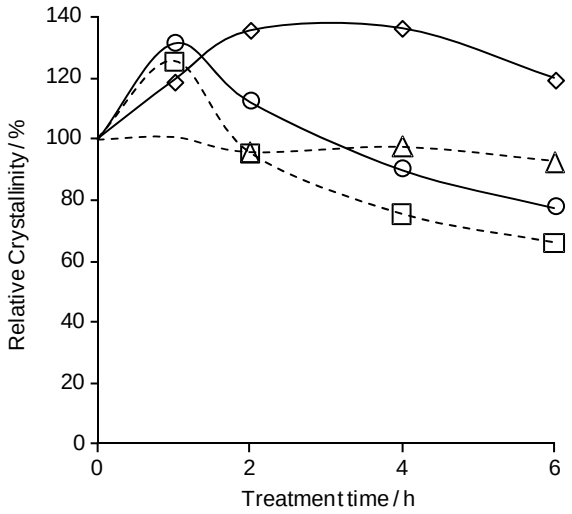

Figure 2.4: Relative crystallinity of zeolite Y5 treated at 150 °C (○) and 200 °C (□) and LaY5 treated at 150 °C (◊) and 200 °C (Δ).

Peak broadening was also observed at both treatment temperatures (Figures A.4 and A.5). The LaY5 sample treated at 200 °C exhibited the same behavior as the parent Y5 material, yet the material retained a relative crystallinity of 93% compared to 66% for the Y5 (Figures 2.4 and A.6). The sample treated at 150 °C maintained a relative crystallinity above 100% throughout the entire course of treatment.

The ZSM-5 samples showed no appreciable change in the signature peaks, which indicates that the underlying crystalline structure was maintained throughout the entire treatment. This behavior occurred in all ZSM-5 samples regardless of the treatment temperature and is illustrated by the ZSM-5-25 sample (Figure 2.5).

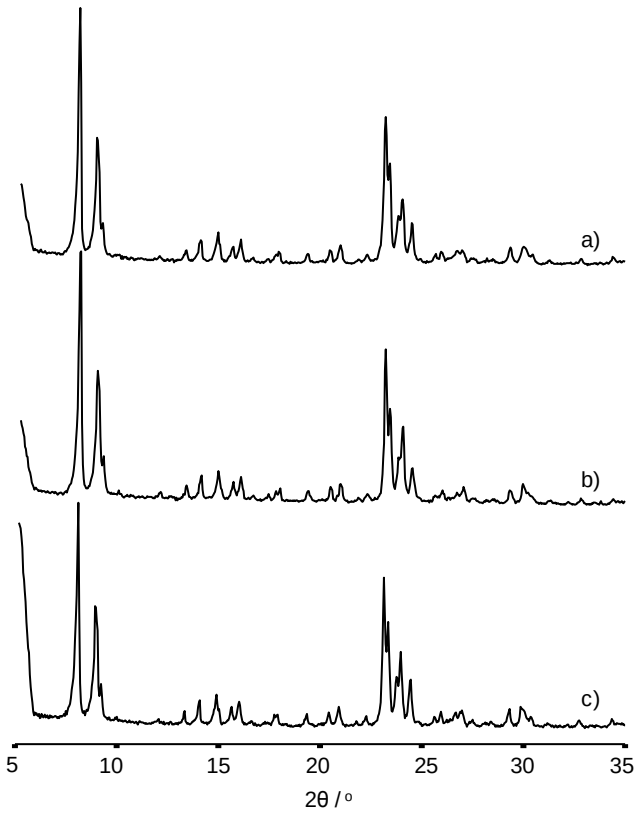

Figure 2.5: X-ray diffractograms of zeolite ZSM-5-25: a) untreated, b) treated at 200 °C for 6 h, c) treated at 150 °C for 6 h.

2.3.3 Scanning Electron Microscopy

The scanning electron micrograph of untreated Y41 shows distinct individual zeolite crystals in the size range of ca. 250 – 700 nm with an average size of ca. 500 nm (Figure 2.6I).

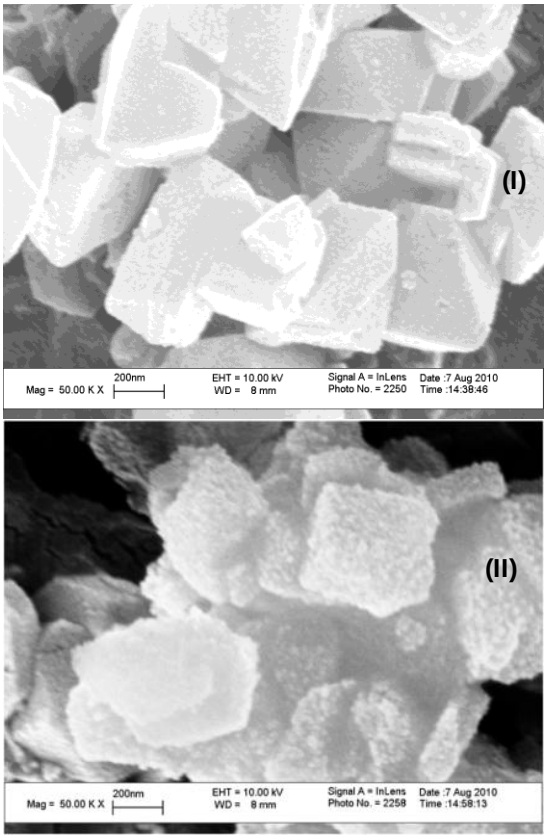

Figure 2.6: Scanning electron micrograph of untreated Y41 (I) and Y41 treated at 200 °C for 6 h (II).

The crystals had a well-defined structure with a smooth surface. The sample treated at 200 °C for 6 h showed signs of degradation of the crystal structure (Figure 2.6II). In addition to losing their sharp edges, the particles showed extensive pitting. There was no noticeable change in the particle size compared to the untreated material.

2.3.4 Argon Physisorption

The changes in the micropore volume of all ZSM-5 samples were within the error margin of the experiment, but a slight increase of the mesopore volume was observed for ZSM-5-40 (Table 2.2).

Table 2.2: Micropore and mesopore volume measured by Ar physisorption for zeolite samples before and after 6 h of treatment at 150 and 200 °C.

Zeolite	$V_{micropore}$ untreated (cm^3/g)	$V_{mesopore}$ untreated (cm^3/g)	$V_{micropore}$ 6 h, 200 °C (cm^3/g)	$V_{mesopore}$ 6 h, 200 °C (cm^3/g)	$V_{micropore}$ 6 h, 150 °C (cm^3/g)	$V_{mesopore}$ 6 h, 150 °C (cm^3/g)
Y41	0.32	0.13	0.00	0.18	0.04	0.23
Y14	0.31	0.16	0.19	0.26	0.27	0.19
Y5	0.34	0.13	0.22	0.15	0.29	0.13
LaY5	0.32	0.10	0.27	0.09	0.29	0.10
ZSM-5-40	0.24	0.03	0.22	0.07	0.23	0.06
ZSM-5-25	0.21	0.03	0.19	0.04	0.22	0.04
ZSM-5-15	0.21	0.04	0.21	0.04	0.21	0.05

More noticeable changes were observed for all faujasite materials (Table 2.2, Figure 2.7). The reduction of the micropore volume intensified with increasing Si/Al ratio. In all cases, the remaining micropore volume was larger after treatment at 150 °C compared to 200 °C. In fact, Y14, Y5, and LaY5 retained more than 80% of their micropore volume during treatment at 150 °C for 6 h.

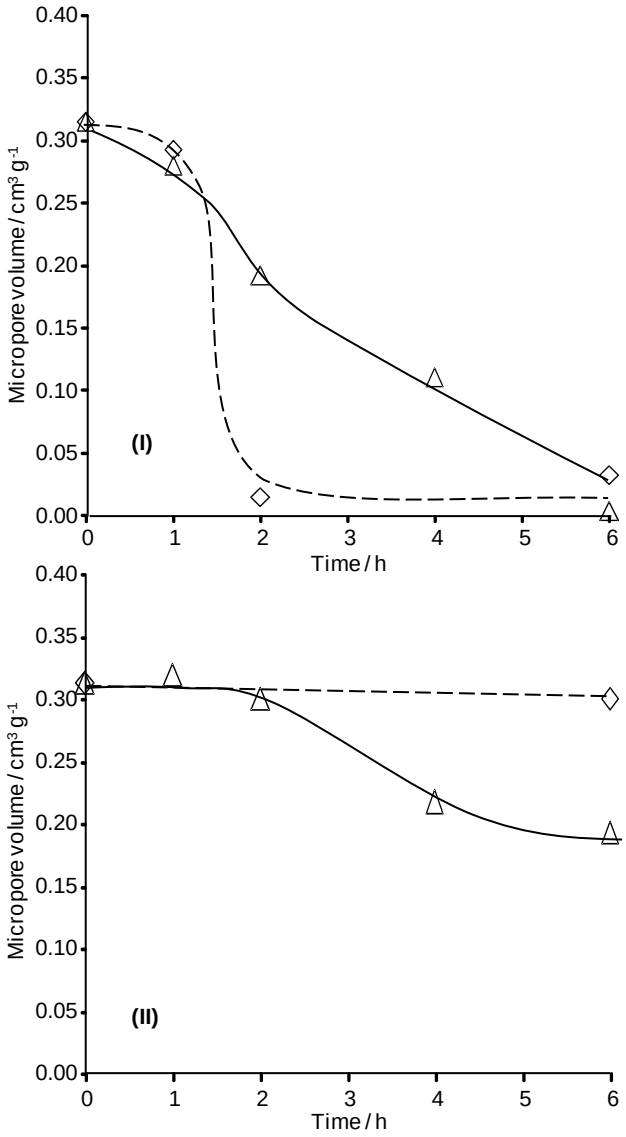

Figure 2.7: Micropore volume of zeolite Y41 (I) and Y14 (II) treated at 200 °C (Δ) and 150 °C (◊).

It is noteworthy that the micropore volume of LaY5 decreased less than that of its parent material Y5. The greatest reduction in micropore volume was observed for Y41, with almost no measurable micropore volume remaining after 6 h at 200 °C or 150 °C. At the same time, the mesopore volume exceeded that of untreated Y41 by ca. 40% and 80%, respectively. The only other faujasite sample to show an increased mesopore volume was Y14 after treatment at 200 °C.

2.3.5 ^{27}Al MAS NMR Spectroscopy

The ^{27}Al MAS NMR spectra of all untreated Y zeolite samples contained resonances at 60 ppm and 0 ppm, which are attributed to tetrahedrally and octahedrally coordinated aluminum species, respectively (Figures 2.8a, A.7a-A.11a).[9]

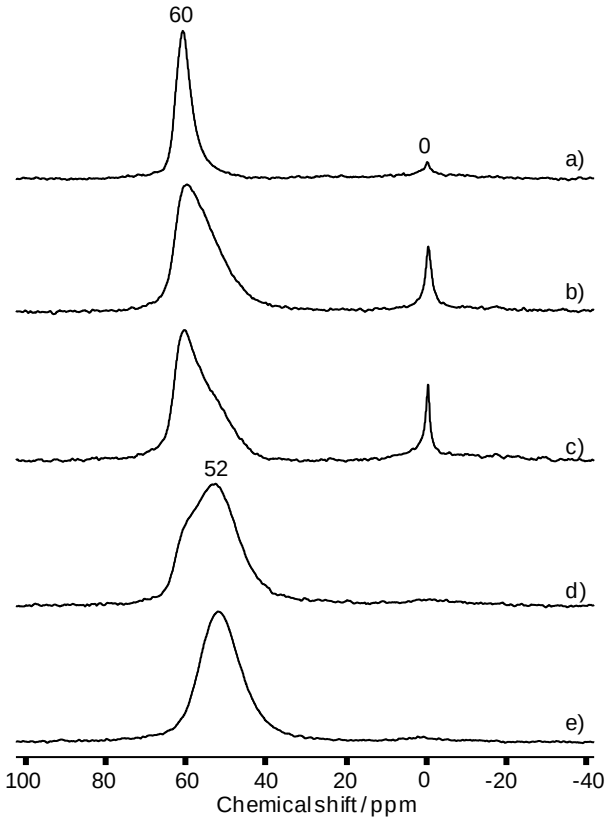

Figure 2.8: ^{27}Al MAS NMR spectra of zeolite Y41 treated at 200 °C: a) untreated, b) 1 h, c) 2 h, d) 4 h, e) 6 h.

Framework aluminum species are tetrahedrally coordinated and resonate at 60 ppm for faujasite type zeolites. Extra-framework aluminum (EFAl) species are primarily found in octahedral coordination in hydrated samples.[12,30] It is important to note that the untreated samples contained both tetrahedrally and octahedrally coordinated EFAl, which was likely generated during the steaming process in the synthesis of ultrastable zeolite Y.[8] A

chemical shift of 52 ppm was observed for tetrahedrally coordinated EFAl. Except for LaY5 (Figure 2.12I), the resonances at 0 ppm were sharp. These features are commonly assigned to cationic Al species that are associated with the framework and can be quantitatively reinserted into the framework in basic media.[15,31]

In untreated Y41, 82% of the aluminum nuclei were tetrahedrally coordinated framework species, whereas 9% were tetrahedrally coordinated EFAl (Figure 2.9). Octahedrally coordinated EFAl species comprised 9% of the Al nuclei.

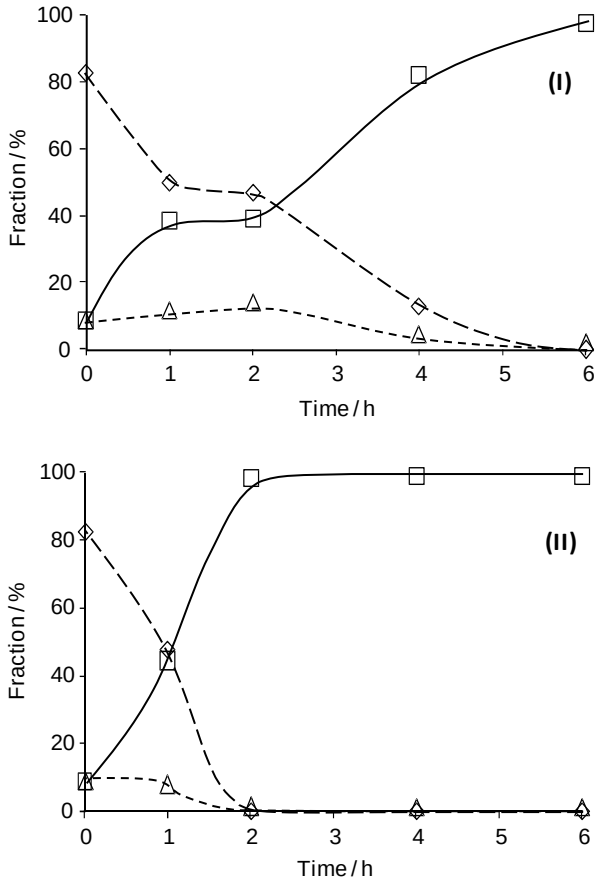

Figure 2.9: Distribution of aluminum in Y41 treated at 200 °C (I) and 150 °C (II): □ = tetrahedral extraframework Al, ◊ = tetrahedral framework Al, Δ = octahedral extraframework Al.

During the first hour of the treatment at 200 °C, the fraction of framework aluminum atoms decreased to 50%. At the same time, the concentration of octahedrally coordinated EFAl increased to 12%, and the concentration of tetrahedrally coordinated EFAl species increased to 39% (Figure 2.9I). Only small changes occurred during the second hour of the treatment, but after 4 h, the resonance corresponding to octahedrally coordinated Al had broadened and decreased to 5% while the remaining framework aluminum was converted into tetrahedrally coordinated EFAl (Figure 2.9I). The concentration of this species was 82 and 97% after 4 and 6 h of treatment, respectively.

At a treatment temperature of 150 °C, the transformation of the tetrahedrally coordinated aluminum species was faster than treatment at 200 °C (Figures 2.9II, A.7). The signal at 60 ppm completely disappeared within 2 h while the new species resonating at 52 ppm was formed. The concentration of octahedrally coordinated Al decreased from 9% to 8% during the first hour of the experiment. After 2 h, only 1% of the Al nuclei were octahedrally coordinated. The disappearance of this species coincided with the transformation of the framework aluminum species to tetrahedrally coordinated EFAl (Figure A.7).

In the case of Y14, a similar conversion of tetrahedrally coordinated framework aluminum to a new tetrahedrally coordinated aluminum species was observed during treatment at 200 °C (Figure A.8). However, even after 6 h of treatment, 23% of the aluminum nuclei remained in framework positions, whereas 72% had been converted to tetrahedrally coordinated EFAl (Figure 2.10I).

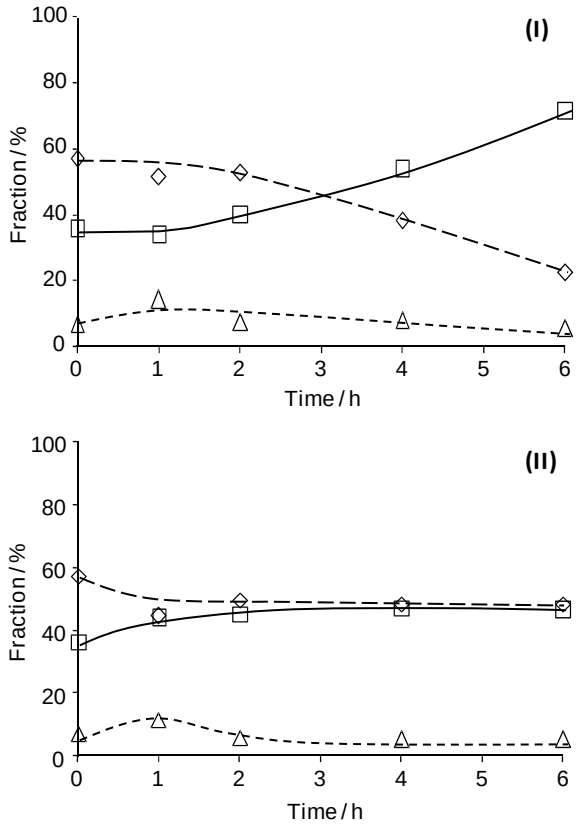

Figure 2.10: Distribution of aluminum in Y14 treated at 200 °C (I) and 150 °C (II): □ = tetrahedral extraframework Al, ◊ = tetrahedral framework Al, Δ = octahedral extraframework Al.

The concentration of octahedrally coordinated Al increased from 7% to 14% in the first hour of the treatment and gradually decreased as the treatment continued. After 6 h, only 6% of the Al nuclei were octahedrally coordinated. It is interesting to note that the width of the peak at 0 ppm increased from 4.9 ppm (untreated sample) to 7.6 ppm after treatment for 6 h. When Y14 was treated at 150 °C, the concentration of tetrahedrally coordinated framework decreased from 57% to 45% while the concentration of tetrahedrally coordinated EFAl aluminum content increased from 36% to 44% (Figures 2.10II, A.9). At the same time, the octahedrally coordinated aluminum content increased from 7% to 11%. After 2 h, the octahedral EFAl species accounted for 5% of the

aluminum nuclei, which remained constant for the remainder of the treatment. The tetrahedral framework aluminum increased to ca. 49% where it remained, while no major changes were observed for the non-framework species.

In addition to the peaks at 60 and 0 ppm, the spectrum of untreated Y5 (Figure 2.11Ia) contained a broad resonance at 30 ppm, which could be assigned to distorted tetrahedral Al or pentahedrally coordinated Al.[15,30]

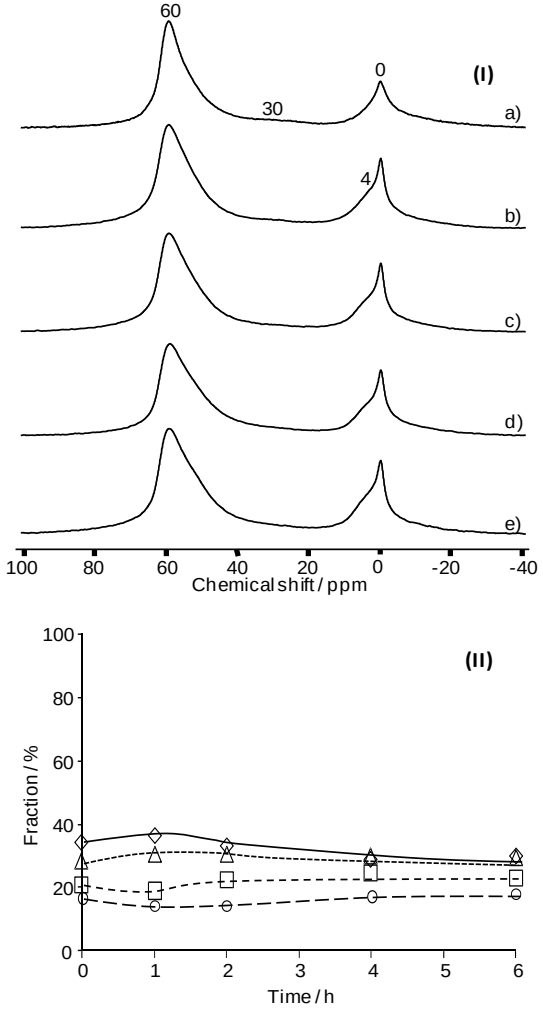

Figure 2.11: ^{27}Al MAS NMR spectra of zeolite Y5 (I) treated at 200 °C: a) untreated, b) 1 h, c) 2 h, d) 4 h, e) 6 h. Distribution of aluminum in Y5 treated at 200 °C (II): ◊ = tetrahedral framework Al, □ = tetrahedral extraframework Al, Δ = octahedral extraframework Al, ○ = heavily distorted framework Al.

This peak represented 14 to 17% of the Al nuclei. Additionally, a shoulder was observed at 52 ppm indicating the presence of non-framework species with tetrahedral coordination (Figures 2.11, A.10). The concentration of this species increased from 21% to 23% during 6 h at 200 °C. The shape of the peak corresponding to octahedrally coordinated Al clearly changed during the first hour of the treatment as evidenced by an increase of a peak at 4 ppm. This species accounted for 6% of the Al in the untreated sample and 11% in the sample after 6 h at 200 °C. However, the concentration of octahedrally coordinated Al only increased from 28 to 30% during 6 h at 200 °C. The change of the peak corresponding to octahedrally coordinated Al species was the only significant change during the treatment of Y5 at 150 °C (Figure A.10).

The spectrum of La^{+3} exchanged Y5 (i.e. LaY5) contained a broad resonance in the 30-40 ppm range (Figure 2.12Ia) representing 32% of the Al nuclei.

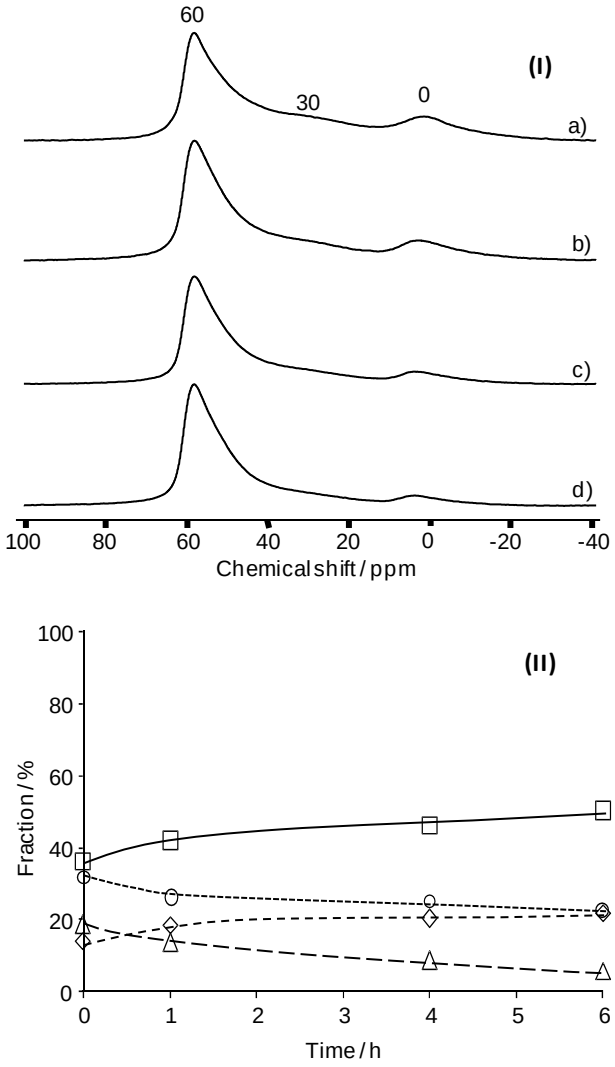

Figure 2.12: ^{27}Al MAS NMR spectra of zeolite LaY5 (I) treated at 200 °C: a) untreated, b) 1 h, c) 4 h, d) 6 h. Distribution of aluminum in LaY5 treated at 200 °C (II): ◊ = tetrahedral framework Al, □ = tetrahedral extraframework Al, Δ = octahedral extraframework Al, ○ = heavily distorted framework Al.

This resonance is attributed to distortion of the zeolite framework by the multivalent lanthanum cations.[32-33] The concentration of this species decreased to 26% after 1 h of treatment at 200 °C and was between 22% and 25% as the treatment time was extended to 6 h. The concentration of octahedrally coordinated EFAl decreased from 19% to 14% in the first hour and then to 6% after 6 h at 200 °C (Figure 2.12II). The concentration of non-distorted framework Al and tetrahedrally coordinated EFAl increased during the first

hour. It is noteworthy that the ratio between the concentrations of these species remained constant as the treatment time was extended from 1 to 6 h. The sample treated at 150 °C showed no changes over the course of a six hour treatment other than the decrease of the resonance corresponding to framework aluminum in the vicinity of lanthanum cations (Figure A.11).

The aqueous treatments were also performed on three ZSM-5 samples with Si/Al ratios of 15, 25, and 40. The untreated samples contained much less octahedral Al than in any of the zeolite Y samples, and the resonance of tetrahedrally coordinated Al was located at ca. 54 ppm as typical for ZSM-5 (Figures 2.13a, A.12a, A.13a).[10]

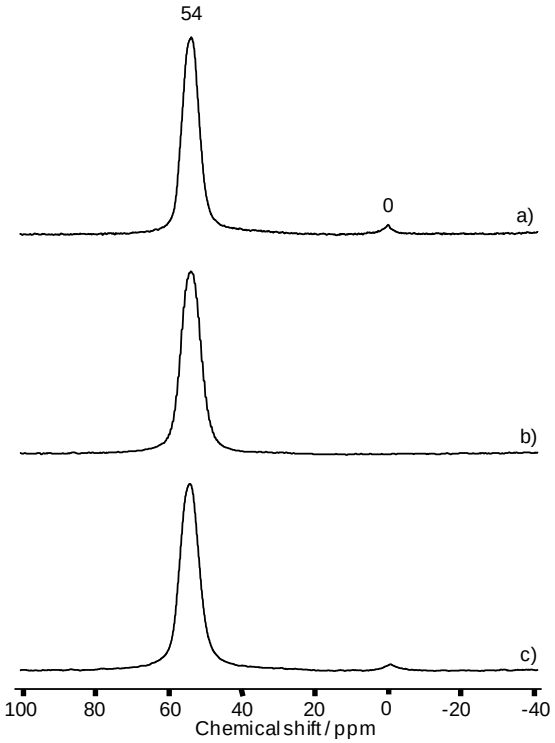

Figure 2.13: ^{27}Al MAS NMR spectra of zeolite ZSM-5-25: a) untreated, b) treated at 200 °C for 6 h, c) treated at 150 °C for 6 h.

None of the ZSM-5 samples showed a significant change of the resonance corresponding to tetrahedrally coordinated framework aluminum or formation of any new

species after treatments at both 150 °C and 200 °C for up to 6 h. However, the peaks of octahedral Al species disappeared for each sample after 6 h at 200 °C, whereas no significant change was observed after 6 h at 150 °C (Figure 2.13, A.12, A.13).

2.3.6 ^{27}Al MQMAS NMR Spectroscopy

Zeolite Y14 after treatment at 200 °C for 4 h was further investigated by ^{27}Al MQMAS NMR to differentiate between electrostatic and quadrupolar contributions in the ^{27}Al MAS NMR spectra (Figure 2.14).

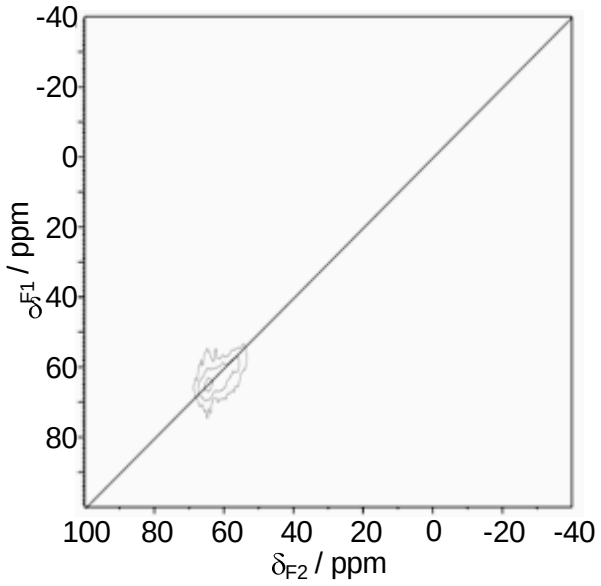

Figure 2.14: ^{27}Al MQMAS NMR spectrum of Y14 after treatment at 200 °C for 4 h.

The spectrum was dominated by the resonance corresponding to aluminum in the framework (δ_{F1} = δ_{F2} = 64 ppm). Additionally, the peak corresponding to the new tetrahedrally coordinated aluminum species was observed at δ_{F1} = δ_{F2} = 59 ppm. The chemical shift in F1 and F2 dimension was identical for both species. This indicates that the chemical shift is only influenced by electrostatic effects.[34] A quadrupolar-induced

shift, which would result from a distortion of the coordination sphere of the aluminum nuclei,[32-33] is essentially absent. The resonance corresponding to octahedrally coordinated aluminum was not resolved in the ^{27}Al MQMAS NMR spectrum due to the low concentration of this species.

2.3.7 ^{29}Si MAS NMR Spectroscopy

The ^{29}Si MAS NMR spectra for untreated zeolites Y41 and Y14 contained resonances at -103 ppm and -109 ppm (Figures 2.15a, 2.16a). The resonance at -103 ppm is assigned to framework Si atoms with three Si and one Al atoms as next-nearest neighbors, whereas the resonance at -109 ppm is attributed to a Si atom surrounded by four neighboring Si atoms.[12,35]

Significant changes were observed for Y41 after treatment at 150 and 200 °C after 6 h. The spectra of the treated samples were dominated by a broad peak at -113 ppm (Figure 2.15).

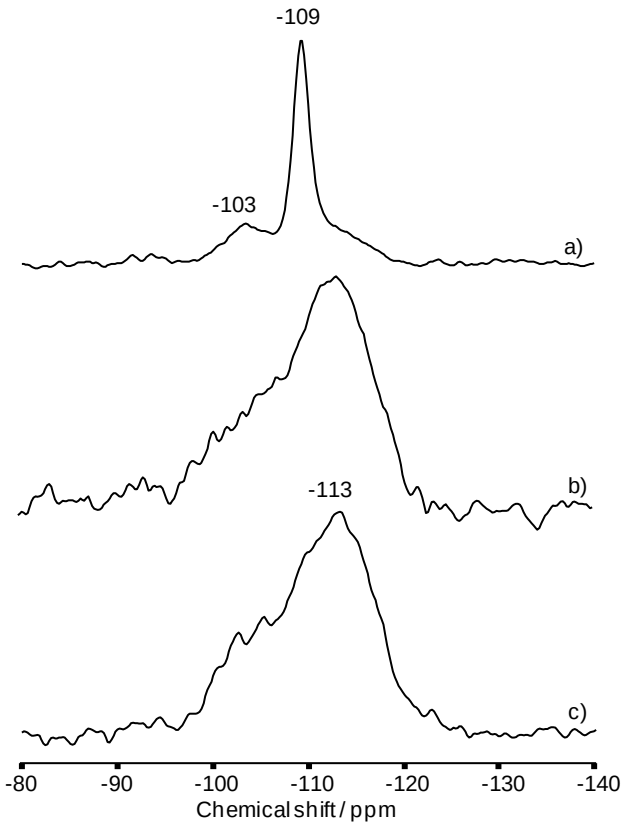

Figure 2.15: ^{29}Si MAS NMR spectra of zeolite Y41: a) untreated, b) treated at 200 °C for 6 h, c) treated at 150 °C for 6 h.

This position is upfield from the resonance at -109 ppm (Si nuclei with four next-nearest Si neighbors). Typically, an upfield shift indicates a higher degree of condensation (fewer protons or Al nuclei as next-nearest neighbors). However, a silicon atom with four next-nearest Si neighbors is already in the environment with the highest possible degree of condensation within a zeolite framework. Therefore, the upfield shift is likely attributed to formation of an amorphous silica or silica-alumina phase.[12]

Untreated Y14 contained 23% of Si atoms with three Si and one next nearest Al neighbor, while 77% had only Si as next nearest neighbors (Figure 2.16a).

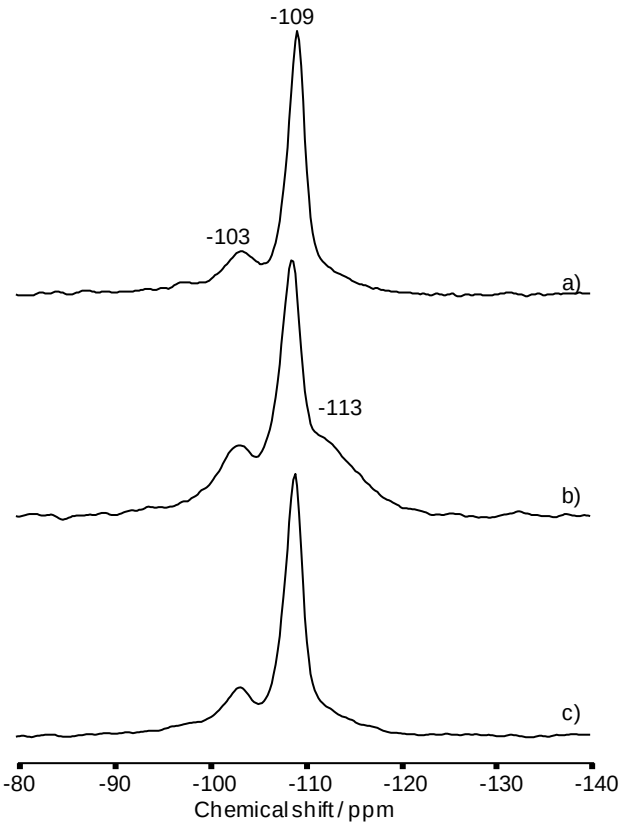

Figure 2.16: ^{29}Si MAS NMR spectra of zeolite Y14: a) untreated, b) treated at 200 °C for 6 h, c) treated at 150 °C for 6 h.

After 6 h at 200 °C, an upfield resonance was observed at -113 ppm indicating 24% of the Si nuclei were in an amorphous phase. The amount of Si with four next nearest Si atom neighbors decreased to 53%, while 23% of the available Si had three Si and one Al as next nearest neighbors (Figure 2.16b). After 6 h at 150 °C, there was no indication of amorphous silica phase, and the distribution between the Si atoms with three Si and one Al as next nearest neighbors and Si atoms surrounded by only Si as next nearest neighbors was unchanged from the untreated material (Figure 2.16c).

2.3.8 Temperature-programmed Desorption of Ammonia

As expected, the acid site concentration of the untreated materials increased with decreasing Si/Al ratio, and a higher concentration was measured for Y5 compared to its lanthanum-exchanged form LaY5 (Table 2.3).

Table 2.3: Acid site concentration measured by TPD of ammonia for zeolite samples before and after 6 h of treatment at 150 and 200 °C

Zeolite	C_{acid}, untreated (µmol/g)	C_{acid}, 6 h, 200 °C (µmol/g)	C_{acid}, 6 h, 150 °C (µmol/g)
Y41	185	28	28
Y14	523	654	627
Y5	725	1276	1051
LaY5	644	900	730
ZSM-5-40	395	419	379
ZSM-5-25	532	564	567
ZSM-5-15	920	1044	927

Interestingly, treatment for 6 h increased the concentration of acid sites for all faujasite samples, except Y41. For additional insight, the acid site concentration of Y41 and Y14 was analyzed for samples that had been exposed to liquid water at 150 or 200 °C for different times (Figure 2.17).

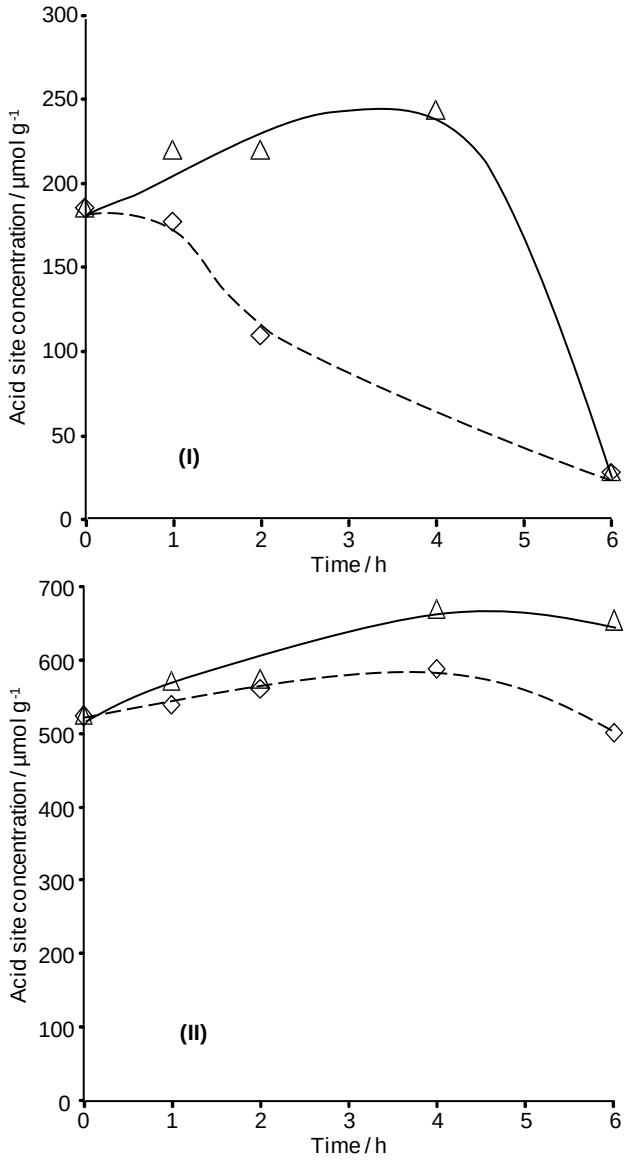

Figure 2.17: Acid site concentration (as measured by TPD of ammonia) of zeolite Y41 (I) and Y14 (II) treated at 200 °C (Δ) and 150 °C (◊).

When Y41 was treated at 200 °C, the concentration of acid sites increased over the first 4 h from 185 µmol·g^{-1} to 243 µmol·g^{-1} followed by a drastic decrease to 28 µmol·g^{-1} when the time was extended to 6 h (Figure 2.17I). In contrast, a steady decrease of the acid site concentration was observed during the treatment of the same material at 150 °C.

An initial increase in the acid site concentration was also found when Y14 was treated at both 150 and 200 °C (Figure 2.17II). After 4 h at 150 °C, the acid site concentration increased from 523 to 588 $\mu mol \cdot g^{-1}$ after which it declined to 500 $\mu mol \cdot g^{-1}$ after 6 h. A similar trend was observed for treatment at 200 °C where the acid site concentration increased to 670 $\mu mol \cdot g^{-1}$ after 4 h then decreased to a final value of 654 $\mu mol \cdot g^{-1}$. The acid site concentration of Y5 increased from 725 $\mu mol \cdot g^{-1}$ to 1051 and 1104 $\mu mol \cdot g^{-1}$ after 6 h of treatment at 150 °C and 200 °C, respectively. For LaY5, an increase from 644 $\mu mol \cdot g^{-1}$ to 730 and 900 $\mu mol \cdot g^{-1}$ was observed after 6 h of treatment at 150 °C and 200 °C, respectively.

An increase from 920 to 1044 $\mu mol \cdot g^{-1}$ was observed for the acid site concentration of ZSM-5-15 during 6 h at 200 °C. The acidity of all other ZSM-5 samples was within the error margin from their original acid site concentration.

2.3.9 Pyridine Adsorption

The adsorption of pyridine on Y14 was studied to differentiate between Brønsted and Lewis acid sites (Figure 2.18).

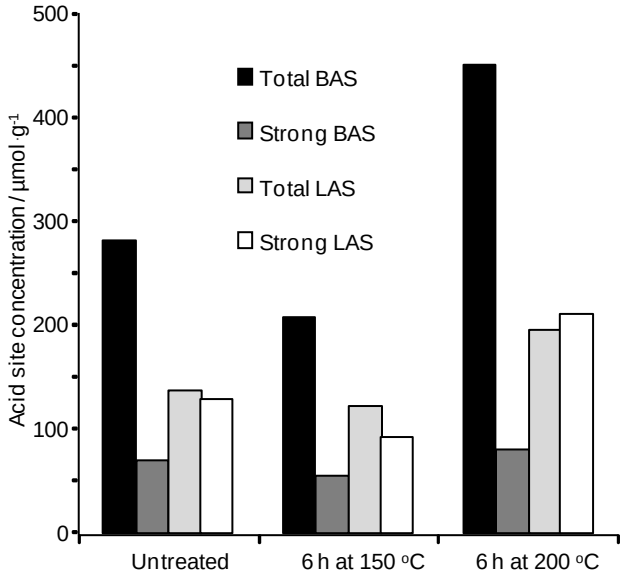

Figure 2.18: Acid site concentration (as measured by adsorption of pyridine) for treated and untreated zeolite Y14 (BAS = Brønsted acid sites, LAS = Lewis acid sites).

The untreated sample contained mostly Brønsted acid sites, with the majority being weak in nature. After 6 h of treatment at 200 °C, there was an increase in the concentration of Brønsted and Lewis acid sites adsorbing pyridine. Most of the additional Brønsted acid sites were weak acid sites, whereas all of the additional Lewis acid sites were strong. The sample treated at 150 °C exhibited a decrease in Brønsted and Lewis acid site concentration. Interestingly, mostly weak Brønsted acid sites and strong Lewis acid sites were lost.

2.4 Discussion

2.4.1 Mechanisms of Structural Changes Induced by Water

Two variants of hydrolysis, one at the Si-O-Si and the other at Si-O-Al sites exist for the reaction of the framework of zeolites and mesoporous silica-alumina with water.[19,21-22] The Si-O-Al hydrolysis is proton catalyzed, whereas hydroxyl ions catalyze siloxane bond cleavage (Figure 2.19).[19,36]

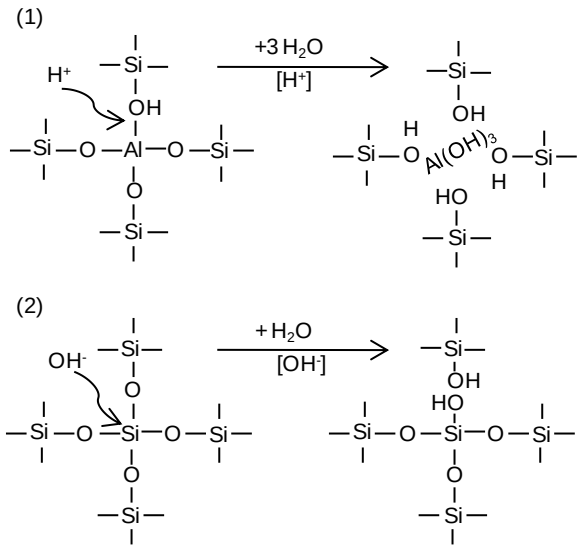

Figure 2.19: Mechanisms for acid-catalyzed dealumination (1) and base-catalyzed hydrolysis of siloxane bonds (2).

During the siloxane hydrolysis, a Si-O-Si bond is broken and two silanol groups are formed.[23] It has been suggested that this reaction accelerates upon formation of silanol groups because of their strong interaction with water molecules and hydroxyl ions.[37] At elevated temperatures, the reverse reaction of hydrolysis – dehydroxylation – becomes relevant. Base-catalyzed hydrolysis also occurs at Si-O-Al bonds, yet they are more

resistant to attack from water. In addition, Al in tetrahedral positions creates a net negative charge in the framework, which repels OH^- ions that are responsible for siloxane hydrolysis.[21] It has been suggested that framework aluminum atoms do not only protect their four Si-O-Al bonds from base-catalyzed hydrolysis but also siloxane bonds that are further away from the Al atoms.[20] Hydrolysis of Si-O-Al bonds is commonly referred to as dealumination. During this reaction, aluminum atoms are removed from their framework positions, and silanol "nests" are formed.[7] These consist of four Si-OH groups associated with the four Si atoms that previously surrounded the framework Al.[29] Silanol "nests" can be "healed" by incorporation of silicon atoms from other parts of the zeolite lattice, which are completely removed in the process. The consumption of entire portions of the zeolite framework leads to the formation of a secondary mesopore structure.[8,38-39] It is interesting to note that the removal of framework Al species appears to occur mostly once the zeolite samples are cooled down after steam treatment.[40]

In general, high-silica zeolites are strongly affected by basic solutions, whereas high-alumina zeolites transform more readily in acidic media.[16,19] However, it has to be taken into account that pK_W of water decreases from 14.0 at room temperature to 11.6 at 150 °C and 11.3 at 200 °C, respectively.[41] In other words, a significantly increased concentration of ionic species is present under the conditions applied in this study. Therefore, acid- and base-catalyzed reactions are facilitated.

Under the conditions applied here, transformation of ZSM-5 was not observed (*vide infra)*. Therefore, the discussion on structural changes is focused on zeolite Y, and in particular, the materials with higher Si/Al ratios. During the treatment of Y41 and Y14, a decrease of the ^{27}Al resonance corresponding to framework aluminum species and the

increase of a resonance at 52 ppm indicates that these materials are transformed as a result of the treatment (Figures 2.8 and A.8). The low quandrupolar-induced shift of both tetrahedrally coordinated species in the ^{27}Al MQMAS NMR spectrum of Y14 after treatment at 200 °C for 6 h (Figure 2.14) allows exclusion of a distortion of zeolite lattice as the explanation for the observed changes. Instead, it is concluded that the new aluminum species is present in a chemically different environment with almost perfectly symmetric tetrahedral coordination of the Al nuclei.

In parallel to the formation of the tetrahedrally coordinated EFAl species, the relative crystallinity of the samples decreased, which is consistent with the conversion of the crystalline zeolite phase into an amorphous material (Figures 2.3-2.4). It is interesting to note that there was a strong decrease of the relative crystallinity when the concentration of tetrahedrally coordinated EFAl reached 40-50% (Figure 2.20).

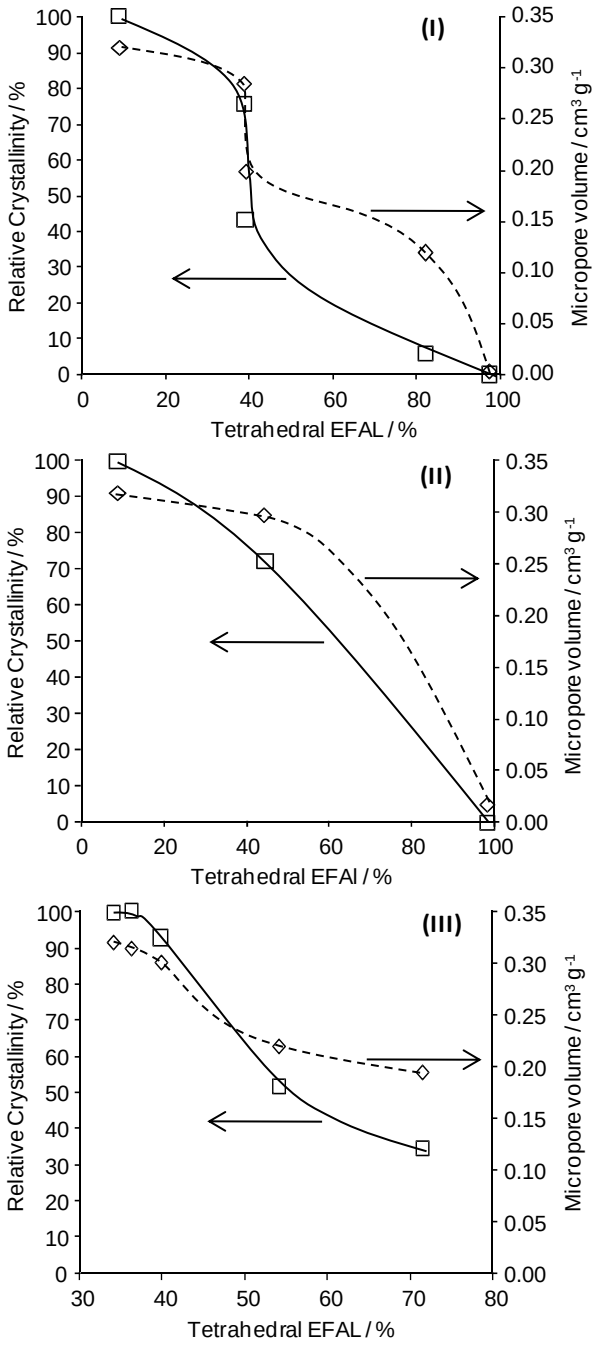

Figure 2.20: Correlation between remaining micropore volume (◊) and relative crystallinity (□) to tetrahedral EFAL for Y41 treated at 200 °C (I) and 150 °C (II) and Y14 treated at 200 °C (III).

In addition to a decrease in relative crystallinity, the XRD peaks broadened. This observation is attributed to a gradual decrease of the crystallite size by continuous

attrition of crystal structure. The micropore volume also decreased with increasing concentration of tetrahedrally coordinated EFAl, but the loss of microporosity was slower than the decrease of the relative crystallinity (Figure 2.20). A low micropore volume (< 0.05 $cm^3 \cdot g^{-1}$) was observed for samples that had been completely converted into amorphous material. In parallel to the decrease of the micropore volume, the mesopore volume increased (Table 2.2). Therefore, the decrease of the total pore volume of the faujasite samples was much less severe than the decrease of the micropore volume. This indicates that during the degradation, parts of the pore walls in the zeolite are removed resulting in the formation of a secondary mesopore structure. Similar changes occur under harsh steaming conditions.[38-39] These observations are in line with the fact that amorphous materials usually have very limited microporosity.

In the case of zeolite Y41, the conversion into an amorphous phase was completed over the course of our experiment. Although the newly formed phase appears to be completely amorphous, the aluminum atoms remain tetrahedrally coordinated, which suggests that their local environment does not change. Instead, it is suggested that the zeolite framework collapses in a way that only involves breaking a limited number of bonds in the lattice. The formation of an amorphous silica-alumina phase is also supported by the observation of a broad peak at -113 ppm in the ^{29}Si MAS NMR spectra of Y41 treated 6 h at both 150 and 200 °C and a smaller peak at -113 ppm for Y14 treated 6 h at 200 °C (Figures 2.15 and 2.16).[12-13] These observations clearly show that Y41 degrades faster than Y14 under the given conditions. Although Y14 is not completely converted into an amorphous phase, it is clearly affected by the treatment and cannot be considered as

"stable". The timescale in which the collapse occurs is on the order of hours, although the degree of collapse varies for both materials.

A comparison of the changes in the ^{27}Al and ^{29}Si MAS NMR spectra of Y14 and Y41 suggests that the local environment of the silicon atoms is modified to a considerably larger extent than that of the framework aluminum atoms. Specifically, the Si-O-Al bonds appear to show a considerable resistance against cleavage under the given conditions. This trend in reactivity implies that hydrolysis of siloxane groups is the main degradation pathway. Further evidence for this hypothesis is the fact that only 2% and 6% of octahedrally coordinated aluminum were observed in the ^{27}Al MAS NMR spectra of Y41 and Y14 treated for 6 h at 200 °C, respectively (Figures 2.8 and A.8). If dealumination played a significant role, a considerable amount of these species would form. Once EFAl is formed, it is unlikely that it is reincorporated into the framework under the given conditions.[19] It is certainly possible that octahedrally coordinated EFAl would be dissolved and escape detection. However, elemental analysis by AAS showed minor changes of the Si/Al ratio after 6 h of treatment. It is therefore safe to conclude that siloxane hydrolysis plays a dominant role in the transformation of Y41 and Y14. Additional evidence for this degradation pathway is provided by the scanning electron micrographs of Y41 (Figure 2.6). After 6 h at 200 °C, the sample shows clear signs of pitting. We speculate that this change of the morphology results from siloxane hydrolysis, which starts at terminal Si-OH groups and propagates from there.[20-21,23,36]

The degradation pathway proposed here is in line with reports on transformations of mesoporous materials, which are also mainly affected by siloxane hydrolysis when treated in condensed phase at 100 °C.[30-31] A similar amorphization mechanism has been

observed when zeolites were treated at very high temperatures and pressures (T > 1000 K, P > 3 GPa) .[42]

Only small changes were observed for the concentration of different Al species in Y5. An increase of the fraction of octahedrally coordinated Al from 28% in the untreated sample to 31% after 1 h at 200 °C indicated that dealumination might occur for this sample (Figure 2.11). Degradation by siloxane hydrolysis appears to occur to a limited extent as indicated by the decrease of the concentration of tetrahedrally coordinated framework Al from 34% in the untreated material to 30% after 6 h at 200 °C. The distribution of aluminum in LaY5 was more strongly influenced by exchange of charge compensating cations than by degradation of the sample (*vide infra*).

An initial increase of the relative crystallinity was observed for Y5 as well as for LaY5 during treatment at 150 °C (Figure 2.4). An increase in crystallinity could be due to removal of an amorphous phase present in the untreated sample. However, elemental analysis by AAS did not show a significant change in the Si/Al ratio. Instead, we suggest that the increase in crystallinity is caused by a reduced distortion of the zeolite framework. An examination of the aluminum balances of both the Y5 and LaY5 samples shows a decrease in heavily distorted framework aluminum in the beginning of the treatment (Figures 2.11, 2.12). It is suggested that this distortion results from the presence of multivalent lanthanum and aluminum ions as charge compensating cations.[32] Therefore, removing a fraction of these cations by ion exchange (*vide infra*) would revert the reduction of crystallinity that is observed during incorporation of these species.[43-44] After the first hour, the crystallinity steadily decreased indicating slow crystal degradation (Figure 2.4). A possible explanation for the decreasing crystallinity is that the

treatment temperature was too low for Si migration to the defect sites to occur, i.e. the mitigation of structural defects is kinetically blocked. It is worth mentioning that the dealumination of Y5 is slower than the degradation of Y14 and Y41 by hydrolysis. Therefore, Y5 is a promising starting material for testing a potential stabilization, for example by ion exchange (*vide infra*).

2.4.2 Changes of the Acidity of Zeolites in Water

During the treatment of Y41 and Y14 the concentration of acid sites varied. Initially, the acidity increased. This may be attributed to the formation of new acid sites or to morphological changes of the zeolite that allow ammonia to interact with acid sites not accessible in the untreated material. However, the latter scenario is unlikely, because it was shown that all cationic sites in faujasite type zeolites can be ion exchanged for ammonium ions.[45] The formation of Lewis acid sites has been reported under steaming conditions.[7] In the present case, however, the concentration of Brønsted acid sites increased by 170 $\mu mol \cdot g^{-1}$ for Y14 after treatment at 200 °C. The concentration of Lewis acid sites increased by only 57 $\mu mol \cdot g^{-1}$ during the treatment. Additional Brønsted acid sites could form by incorporating additional Al atoms into the zeolite framework, exchanging charge compensating metal cations for protons or dissociative adsorption of water on a framework independent alumina phase. The ^{27}Al MAS NMR spectra of Y14 and Y41 showed no evidence for the formation of framework Al species. Consequently, the first explanation is highly unlikely. Considering that the sodium cations occupy less than 2% of the cationic sites in Y14 and Y41, protons and some EFAl species[7,13] are the relevant charge compensating cations in these materials. Note that charge compensating aluminum cations can be present as Al^{3+}, $Al(OH)^{2+}$ or $Al(OH)_2^{+}$.[46] Consequently, up to

three protons are required to replace one of these cations. We speculate that a part of the increase in acidity is due to ion exchange. It is also possible that Brønsted acid sites form by dissociative adsorption of water on a framework independent alumina.[47] This reaction readily occurs under the conditions applied here.[48] Figure 16 shows that the amorphous material resulting from complete conversion of Y41 is low in acidity. However, the loss of acidity was slower than the decrease of the micropore volume. In particular, after treatment at 150 °C for 2 h, the micropore structure of Y41 had collapsed completely (Figure 2.7I), while the material still had considerable acidity (Figure 2.17I). Therefore, these acid sites cannot be associated with any crystalline phase as typically observed in zeolites. Consequently, we speculate that a fraction of the acid sites is located in mesoporous environments. Their exact nature will be the subject of future investigations.

2.4.3 Influence of the Si/Al Ratio and Framework Type on the Stability

Usually, steaming shows greater impact as the Si/Al ratio decreases.[16] Similar trends have been found for mesoporous materials. For example, it was reported that MCM-41 with a Si/Al ratio of 50 is less stable than the pure silica material when treated with steam.[22] However, an increased stability upon incorporation of aluminum was found in boiling water.[22] The addition of small amounts of aluminum (Si/Al = 40) increased the stability of MCM-41 in boiling water compared to the purely siliceous material, because under these conditions aluminum is incorporated near the surface of MCM-41.[21-22] In this position, aluminum atoms are capable of protecting the framework against hydrolysis, because the negative framework charge repels hydroxyl ions. When larger concentrations of aluminum are present in the synthesis mixture of MCM-41, aluminum occupies positions within the pore walls. The stabilizing effect of aluminum within the walls was

found to be much less than that of surface aluminum species.[21-22] In this context, it is important to mention that framework aluminum atoms in zeolites are always present in positions that are comparable to the "surface" positions in MCM-41.

Therefore, it is not surprising that in the present work the stability of zeolite Y increased with decreasing Si/Al ratio. Specifically, the material with the highest Si content (Y41) completely degraded within the time of the treatments, whereas the Y14 showed only partial degradation at 200 °C. Note, there were only minor changes of the Al distribution in Y14 at 150 °C and the decrease of the micropore volume was smaller than during treatment at 200 °C. For Y5, the resonances corresponding to tetrahedrally coordinated Al changed slightly indicating that siloxane hydrolysis is effectively prevented for this material even at 200 °C. However, an increase of the concentration of octahedrally coordinated EFAl from 28 to 30% over the course of treatment indicates that the material may be affected by dealumination. Despite the relatively minor changes in the ^{27}Al MAS NMR spectrum, the degree of crystallinity decreased along with a decrease in crystallite size. Based on these observations, it seems reasonable to suggest that the stability of faujasite type zeolites against hydrolysis in water at 150-200 °C increases with decreasing Si/Al ratio. This trend in Si/Al ratio and stability is opposite to its stability in steam. Faujasite materials with high aluminum concentrations (e.g. Y5) appear to be affected by dealumination even under the conditions applied here.

In addition to the Si/Al ratio, the structure of the zeolite framework has a strong influence on its stability. It is well established that in a gas phase environment, ZSM-5 is more stable than faujasite type zeolites. Even after severe dealumination, ZSM-5 retains most of its relative crystallinity and most of its micropore volume.[10] A possible

explanation for the high stability of ZSM-5 is that very few structural defects are produced during the synthesis of this material.[49] Alternatively, differences in the thermodynamic stability of the framework could play a key role. Petrovic et al. used high temperature solution calorimetry to show that the heat of formation of ZSM-5 exceeded that of faujasite by 5 kJ/mol.[50] They assigned this observation to the presence of four-membered rings in faujasite, which lead to a considerable number of relatively labile Si-O-Si bonds with bonding angles under 140°. It is also possible that the framework density plays a critical role on stability. Lutz et al. found that faujasite type zeolites were less stable in liquid water (T = 130-240 °C) than ZSM-5.[36] They assigned the instability to the larger cavities in faujasite framework, which provide more space for the formation of silica and amorphous aluminosilicate phases.

The present work also shows that ZSM-5 is significantly more stable than faujasite when the materials are treated with liquid water at elevated temperature. At a treatment temperature of 200 °C, a decrease in crystallinity was observed for all faujasite samples, while changes in other properties of the samples confirmed its conversion into an amorphous phase (*vide supra*). The properties (crystallinity, acidity, micropore volume) of the ZSM-5 samples before and after treatment at 200 °C or 150 °C for 6 h were identical independent of the Si/Al ratio of the zeolite (15-40) showing that no structural changes occur under these conditions. The only apparent difference was a slight decrease of the resonance corresponding to octahedrally coordinated Al, which indicates that a small amount of EFAl appears to be removed from these samples.

2.4.4 Stabilizing Effects of Extra-Framework Aluminum and Lanthanum Cations

In addition to stability of the Si-O-Si and Si-O-Al bonds, the nature and concentration of extraframework species (i.e. EFAl and charge compensating cations) influences the stability of zeolites. In particular, increased hydrothermal stability was reported for zeolites containing EFAl from dealumination or decomposition of $AlCl_3$ on the surface.[19,51] It was suggested that EFAl species interact with terminal Si-OH groups and energy rich Si-O-Si bonds near the surface, protecting them against attack by hydroxyl ions.[19,29] A stabilizing effect was also observed for polyvalent charge compensation cations (e.g. La^{3+}).[17-18,51]

Among the faujasite type zeolites used in this study, Y5 contained by far the largest amount of EFAl (Figure 2.11). The ^{27}Al MAS NMR spectra of this material showed that hydrolysis only occurred to a very limited extent (*vide supra*). We tentatively assign this effect in parts to the protective function of EFAl. Further evidence for this hypothesis was derived from analyzing the transformation of faujasite Y41. Only a small amount of octahedrally coordinated Al was present in the untreated form of this material. However, the corresponding ^{27}Al resonance (δ = 0 ppm) increased markedly during the first hour of the treatment at 200 °C indicating that EFAl was formed by dealumination (Figure 2.8). Octahedral aluminum was also formed during the treatment at 150 °C, but only to a very limited extent due to the high activation barrier for the dealumination reaction. In both cases, the resonance at 0 ppm disappeared as the treatment proceeded. The effect of the EFAl species becomes clearer when the intensity of the ^{27}Al NMR resonance at 0 ppm is correlated to the progress of the hydrolysis reaction. Specifically, the collapse of the zeolite lattice accelerates significantly once the octahedrally coordinated EFAl species

are removed. The stabilizing effect of these species is strong enough to delay the collapse of Y41 at 200 °C. Under these conditions, a complete transformation of Y41 into an amorphous material was only observed after 6 h, whereas the some conversion was reached within 2 h when Y41 was treated at 150 °C.

Motivated by reports that indicated an increased hydrothermal stability for rare earth exchanged faujasite under steaming conditions, we investigated the effect of lanthanum cations on the stability of Y5.[44,51] In the first hour of the treatment at both 200 and 150 °C, the broad ^{27}Al MAS NMR resonance corresponding to framework aluminum atoms with lanthanum as charge compensating cations decreased markedly. After that, its intensity remained unchanged. The behavior may be explained by the fact that lanthanum cations can be present in different positions within the zeolite. Weihe et al. reported that in calcined zeolite Y, lanthanum cations are distributed between the sodalite and supercages.[52] However, lanthanum cations cannot enter or leave the sodalite cages in an aqueous environment due to their large hydration sphere. Therefore, it is suggested that a significant fraction of the lanthanum cations is leached from the supercages while the lanthanum cations in the sodalite cages remain in the zeolite. Except for the changes associated with the removal of lanthanum cations, the ^{27}Al MAS NMR spectra of LaY5 remained constant during treatment at 200 and 150 °C (Figures 2.12, A.11). Moreover, the samples exhibited better retention of the crystalline structure compared to lanthanum-free Y5 (Figure 2.4). We conclude that EFAl species and lanthanum cations increase the stability of faujasite type zeolites in hot water.

2.5 Conclusions

The stability of zeolites in hot liquid water strongly depends on their framework type. ZSM-5 is stable at 150 and 200 °C independent of its Si/Al ratio, whereas various zeolite Y samples are degraded to a level that depends on their Si/Al ratio. The degradation of zeolite Y by condensed water mostly occurs through hydrolysis of Si-O-Si bonds rather than dealumination, which is the dominant degradation pathway under steaming conditions. Hydrolysis leads to the formation of an amorphous material, in which aluminum atoms retain their tetrahedral coordination from the zeolite framework. During the transformation, an increased number of acid sites are formed, possibly as the result of ion exchange with charge compensating aluminum cations and/or dissociative adsorption of water on framework independent alumina. However, the entirely amorphous material obtained from Y41 had a very low acid site concentration, and its micropore volume was much lower than that of the starting material. The extent to which hydrolysis affected the zeolite structure increased with increasing Si/Al ratio. This trend is the opposite of the stability of zeolites against steaming. In addition to hydrolysis, dealumination leads to the formation of a limited amount of octahedrally coordinated EFAl species. The present results indicate that these species have a stabilizing influence on the zeolite framework. A possible explanation is that EFAl blocks Si-OH groups and, thus, prevents the hydrolytic attack by hydroxyl ions. Likewise, the presence of lanthanum cations leads to an increased stability of aluminum-rich zeolite Y in liquid water at 150-200 °C.

The treatment conditions examined in this work are representative for biomass conversion processes, such as hydrolysis and aqueous phase reforming. The present results provide guidance for use of zeolites in these reactions. Most importantly, they

show that the stability of zeolite catalysts in high temperature aqueous environment needs to be considered carefully.

2.5 References

[1] Weitkamp, J. *Solid State Ionics* **2000**, *131*, 175-188.

[2] Meier, W. M.; Olson, D. H.; Baerlocher, C. *Atlas of Zeolite Structure Types*, 4th ed.; Elsevier: London, **1996**.

[3] Lercher, J. A.; Jentys, A. Catalytic Properties of Micro- and Mesoporous Nanomaterials. In *Encyclopedia of Nanoscience and Nanotechnology*; Schwarz, J. A., Contescu, C. I., Putyera, K., Eds.; Marcel Dekker, Inc.: New York, **2004**.

[4] Harding, R. H.; Peters, A. W.; Nee, J. R. D. *Applied Catalysis a-General* **2001**, *221*, 389-396.

[5] Scott, J., Ed. *Zeolite Technology and Applications: Recent Advances*; Noyes Data Corporation, **1980**; Vol. 170.

[6] Baerlocher, C.; Meier, W. M.; Olson, D. H. *Atlas of Zeolite Framework Types: Fifth Revised Edition*; Elsevier, **2001**.

[7] Beyerlein, R. A.; Choi-Feng, C.; Hall, J. B.; Huggins, B. J.; Ray, G. J. *Topics in Catalysis* **1997**, *4*, 27-42.

[8] van Donk, S.; Janssen, A. H.; Bitter, J. H.; de Jong, K. P. *Catalysis Reviews-Science And Engineering* **2003**, *45*, 297-319.

[9] Triantafillidis, C. S.; Vlessidis, A. G.; Evmiridis, N. P. *Industrial & Engineering Chemistry Research* **2000**, *39*, 307-319.

[10] Triantafillidis, C. S.; Vlessidis, A. G.; Nalbandian, L.; Evmiridis, N. P. *Microporous and Mesoporous Materials* **2001**, *47*, 369-388.

[11] Klinowski, J. *Progress in Nuclear Magnetic Resonance Spectroscopy* **1984**, *16*, 237-309.

[12] Sanz, J.; Fornes, V.; Corma, A. *Journal of the Chemical Society, Faraday Transactions I* **1988**, *84*, 3113-3119.

[13] Stockenhuber, M.; Lercher, J. A. *Microporous Materials* **1995**, *3*, 457-465.

[14] Bourgeat-Lami, E.; Massiani, P.; Di Renzo, F.; Espiau, P.; Fajula, F. *Applied Catalysis A: General* **1991**, *72*, 139-152.

[15] Omegna, A.; van Bokhoven, J. A.; Prins, R. *Journal of Physical Chemistry B* **2003**, *107*, 8854-8860.

[16] Breck, D. W.; Flanigen, E. M. *Molecular Sieves* Society of the Chemical Industry: London, **1968**.

[17] Carvajal, R.; Chu, P.-J.; Lunsford, J. H. *Journal of Catalysis* **1990**, *125*, 123-131.

[18] Sievers, C.; Onda, A.; Guzman, A.; Otillinger, K. S.; Olindo, R.; Lercher, J. A. *Journal of Physical Chemistry C* **2007**, *111*, 210-218.

[19] Lutz, W.; Gessner, W.; Bertram, R.; Pitsch, I.; Fricke, R. *Microporous Materials* **1997**, *12*, 131-139.

[20] Sano, T.; Nakajima, Y.; Wang, Z. B.; Kawakami, Y.; Soga, K.; Iwasaki, A. *Microporous Materials* **1997**, *12*, 71-77.

[21] Mokaya, R. *Journal Of Physical Chemistry B* **2000**, *104*, 8279-8286.

[22] Shen, S. C.; Kawi, S. *Journal of Physical Chemistry B* **1999**, *103*, 8870-8876.

[23] Kim, J. M.; Ryoo, R. *Bulletin of the Korean Chemical Society* **1996**, *17*, 66-68.

[24] Xia, Y. D.; Mokaya, R. *Journal of Physical Chemistry B* **2003**, *107*, 6954-6960.

[25] Liu, C.-T.; Lindsay, W. T. *Journal Of Chemical And Engineering Data* **1970**, *15*, 510-513.

[26] ASTM. Standard Test Method for Determination of Relative X-ray Diffraction Intensities of Faujasite-Type Zeolite-Containing Materials, **2008**; Vol. D3906-03.

[27] Ong, L.-H. *Dissertation*; TU München, **2009**.

[28] Treacy, M. M. J.; Higgins, J. B. *Collection of Simulated XRD Powder Patterns for Zeolites: 4th Edition*; Elsevier, **2001**.

[29] Weitkamp, J.; Puppe, L., Eds. *Catalysis and Zeolites: Fundamentals and Applications*; Springer, **1999**.

[30] Remy, M. J.; Stanica, D.; Poncelet, G.; Feijen, E. J. P.; Grobet, P. J.; Martens, J. A.; Jacobs, P. A. *Journal of Physical Chemistry* **1996**, *100*, 12440-12447.

[31] Bourgeatlami, E.; Massiani, P.; Direnzo, F.; Espiau, P.; Fajula, F.; Courieres, T. D. *Applied Catalysis* **1991**, *72*, 139-152.

[32] Sievers, C.; Liebert, J. S.; Stratmann, M. M.; Olindo, R.; Lercher, J. A. *Applied Catalysis A: General* **2008**, *336*, 89-100.

[33] van Bokhoven, J. A.; Roest, A. L.; Koningsberger, D. C.; Miller, J. T.; Nachtegaal, G. H.; Kentgens, A. P. M. *Journal Of Physical Chemistry B* **2000**, *104*, 6743-6754.

[34] Amoureux, J.-P.; Fernandez, C. *Solid State Nuclear Magnetic Resonance* **1998**, *10*, 211-223.

[35] Maciel, G. E.; Sindorf, D. W. *Journal of the American Chemical Society* **1980**, *102*, 7606-7607.

[36] Lutz, W.; Toufar, H.; Kurzhals, R.; Suckow, M. *Adsorption-Journal of the International Adsorption Society* **2005**, *11*, 405-413.

[37] Zhuravlev, L. T. *Colloids and Surfaces a-Physicochemical and Engineering Aspects* **1993**, *74*, 71-90.

[38] Zukal, A.; Patzelová, V.; Lohse, U. *Zeolites* **1986**, *6*, 133-136.

[39] Kawai, T.; Tsutsumi, K. *Journal of Colloid and Interface Science* **1999**, *212*, 310-316.

[40] Agostini, G.; Lamberti, C.; Palin, L.; Milanesio, M.; Danilina, N.; Xu, B.; Janousch, M.; van Bokhoven, J. A. *Journal of the American Chemical Society* **2010**, *132*, 667-678.

[41] Marshall, W. L.; Franck, E. U. *Journal Of Physical And Chemical Reference Data* **1981**, *10*, 295-304.

[42] Greaves, G. N.; Meneau, F.; Sapelkin, A.; Colyer, L. M.; ap Gwynn, I.; Wade, S.; Sankar, G. *Nat. Mater.* **2003**, *2*, 622-629.

[43] Moreira, C. R.; Homs, N.; Fierro, J. L. G.; Pereira, M. M.; de la Piscina, P. R. *Microporous and Mesoporous Materials* **2010**, *133*, 75-81.

[44] Xiao, S. Y.; Levanmao, R.; Denes, G. *Journal of Materials Chemistry* **1995**, *5*, 1251-1255.

[45] Suzuki, K.; Katada, N.; Niwa, M. *Journal of Physical Chemistry C* **2007**, *111*, 894-900.

[46] Martens, J. A.; Souvrijns, W.; van Rhijn, W. M.; Jacobs, P. A. In *Handbook of Heterogeneous Catalysis*; Ertl, G., Knozinger, H., Weitkamp, J., Eds.; Wiley-VCH: Weinheim, **1997**; pp 324-365.

[47] Kasprzyk-Hordern, B. *Advances in Colloid and Interface Science* **2004**, *110*, 19-48.

[48] Raybaud, P.; Digne, M.; Iftimie, R.; Wellens, W.; Euzen, P.; Toulhoat, H. *Journal of Catalysis* **2001**, *201*, 236-246.

[49] Kooyman, P. J.; van der Waal, P.; van Bekkum, H. *Zeolites* **1997**, *18*, 50-53.

[50] Petrovic, I.; Navrotsky, A.; Davis, M. E.; Zones, S. I. *Chemistry of Materials* **1993**, *5*, 1805-1813.

[51] Guzman, A.; Zuazo, I.; Feller, A.; Olindo, R.; Sievers, C.; Lercher, J. A. *Microporous and Mesoporous Materials* **2005**, *83*, 309-318.

[52] Weihe, M.; Hunger, M.; Breuninger, M.; Karge, H. G.; Weitkamp, J. *Journal of Catalysis* **2001**, *198*, 256-265.

CHAPTER 3

γ-AL_2O_3 BASED CATALYSTS

3.1 Background

3.1.1 γ-Al_2O_3 Synthesis and Structure

γ-Al_2O_3, also known as activated alumina, is very commonly used as a support for catalysts. This is due to the fact that it usually has a high surface area and the capability to catalyze a variety of chemical reactions including isomerization, dehydration and dehydrogenation. Catalytic activity arises from the presence of both electron acceptor centers (Lewis acid sites) attributed to coordinatively unsaturated (cus) aluminum ions, and electron donor centers (Brønsted acid sites) which are proposed to arise from strained oxygen bridges.[1] The preparation of γ-Al_2O_3 is typically performed by heating Gibbsite mineral, $Al(OH)_3$, which is accompanied by dehydroxylation and formation of internal surface area. It is noted that the temperature and heating rate can have a drastic effect on the phase development.[1] The structure of alumina is known as defect spinel, which consists of a fairly well ordered oxygen sublattice with aluminum present in both octahedral and tetrahedral coordination. In addition, tetrahedral cation vacancies are found throughout.[1]

3.1.2 γ-Al_2O_3 Hydrothermal Stability

Transition and noble metals supported on metal oxide supports have shown potential for catalytic upgrading of biomass derived feedstocks in aqueous phase.[2-4] Specifically, γ-Al_2O_3 supported catalysts have been used for aqueous phase reforming of biomass-derived oxygenates as well as hydrolysis/hydrogenation of microcrystalline cellulose to

sugar alcohols.[5-7] While these publications have clearly demonstrated the activity and selectivity of supported metal catalysts in water, they did not address their stability under reforming conditions (e.g., 150 °C < T < 265 °C, $P_{sat}(T) < P < 100$ bar).

It is well established that γ-Al_2O_3 will rehydrate in the presence of water, and that boehmite (AlOOH) is thermodynamically favored over gibbsite above 150 °C.[8-9] This transformation was also observed for supported metal catalysts, namely 0.9 wt% Pt/γ-Al_2O_3 used for glycerol reforming at 220 °C and 2.50 MPa over 14 h,[10] as well as for Ru/Al_2O_3 treated with H_2 saturated water at 200 °C and 40 atm over 5 h.[11] However, the design of novel catalysts and/or regeneration procedures depends on an improved understanding of the kinetics of these phase transitions and insight in how these changes affect the properties of the catalyst (e.g. surface acidity).

In the following chapter, the structural transformations as well as changes in acid site concentration and metal dispersion of 1 wt% Pt/γ-Al_2O_3 and 1 wt% Ni/γ-Al_2O_3 supported catalysts under conditions that are relevant for biomass reforming (i.e. liquid water at 200 °C and P^{sat}) as a function of treatment time are examined. In addition, the kinetics of boehmite formation and the effect of metal particles on this transition, as well as the importance of specific surface hydroxyl groups for alumina hydration are demonstrated.

3.2 Materials and Methods

3.2.1 Catalyst Preparation

The catalysts were prepared via incipient wetness procedure which consists in dissolving the required weight of metal precursor in the final solid with the minimum amount of water to wet the dry supports before a slurry is obtained. The slurry was mechanically stirred to achieve maximum homogeneity during the addition of water. The

metal precursors were $H_2PtCl_6 \cdot 6H_2O$ (ACS reagent grade, Sigma Aldrich) and $Ni(NO_3)_2 \cdot 6H_2O$ (99.999% metals basis, Aldrich) and the support was γ-Al_2O_3 (3μm APS powder, 99.97% metals basis, Alfa Aesar). The catalysts were then calcined in air at 500 °C (ramp $1K \cdot min^{-1}$) in air for 4 h followed by reduction in 10% H_2/He at 300 °C (ramp $5K \cdot min^{-1}$) for 3 h prior to treatment.

3.2.2 Catalyst Treatment

Catalyst treatments were performed similar to methods found elsewhere.[12] Briefly, 0.5 g of the solid was suspended in 30 ml of deionized water. Each mixture was poured in an autoclave with a Teflon liner, which was placed in a preheated oven at 200 °C under constant agitation. After a specific amount of time, the reaction was quenched by placing the autoclave in an ice bath. The mixture was filtered (0.45 μm Nylon filter), and the solids were dried in air prior to characterization.

3.2.3 X-ray Diffraction

Powder X-ray diffraction (XRD) patterns were measured on a Philips X'pert diffractometer equipped with an X'celerator module using Cu Kα radiation. Diffractograms were obtained from $2\theta = 5°$ to 70° with a step size of 0.0167°.

3.2.4 NMR Spectroscopy

^{27}Al MAS NMR measurements were performed on a Bruker DSC 400 spectrometer. The samples were packed into a 4 mm zirconia rotor and spun at 12 kHz. The resonance frequency for ^{27}Al was 104.2 MHz. A $\pi/12$ pulse was used for excitation and the recycling delay was 250 msec. For each spectrum, a minimum of 2400 scans were accumulated. Solid $Al(NO_3)_3$ was used as a reference compound (δ = -0.543 ppm). In

order to calculate the boehmite fraction, the normalized ^{27}Al spectra were fit as a linear combination between pure boehmite and pure alumina spectra.

^{1}H MAS NMR measurements were performed on the same instrument with adamantane as a reference compound (δ = 1.756 ppm). Prior to analysis, the samples were dried under vacuum at 200 °C overnight and packed into 4 mm zirconia rotors in a dry box. Samples were spun at 12 kHz for a total number of 64 scans. The obtained spectra were normalized by the sample mass and fit with Lorentzian peaks.

3.2.5 Pyridine Adsorption Followed by IR Spectroscopy

Adsorbed pyridine IR spectra were collected on a Nicolet 8700 FT-IR spectrometer with a MCTA detector and 64 scans at 1 wavenumber resolution. Each catalyst material was pressed into a self supported wafer and loaded into a custom built vacuum chamber operating at ca. 10^{-6} mbar with Teflon sealed ZnSe windows.

The self supported wafers were first activated at 200 °C for 1 h. The temperature was then decreased to 150 °C when the sample was dosed with 0.1 mbar of pyridine vapor. After evacuation, the relevant peaks were integrated to give total acid site concentration using the molar extinction coefficients reported by Datka.[13] The wafer densities were obtained by weighing ¼" diameter pieces of the sample wafer post pyridine analysis.

3.2.6 Nitrogen Physisorption

Physisorption measurements were performed on a Quantachrome Quadrasorb SI surface area and pore volume analyzer at the temperature of liquid nitrogen (-203 °C). Prior to analysis, samples were degassed at 200 °C for two hours under vacuum. The surface area was calculated utilizing the multi-point BET method from the adsorption isotherm in the relative pressure range ($0.05 \leq P/P_0 \leq 0.3$).

3.2.7 H_2-O_2 Titration

Hydrogen chemisorptions experiments were performed on a Micromeritics AutoChem II Chemisorption Analyzer equipped with a thermal conductivity detector. The samples were first treated at 200 °C for 1 h with argon as carrier gas to eliminate adsorbed water. Then the temperature was cooled to ambient after which the sample was ramped to 300 °C (5 K/min) under 10% H_2/Ar. After reduction, the sample was brought to 40 °C and dosed 20 times with 4% H_2/Ar followed by dosing with 10% O_2/He. A final dosing of 4% H_2/Ar was performed and used for the dispersion analysis. An H_2/Pt surface stoichiometry of 1.5 was assumed according to the proposed titration reactions.[14-15]

$$(1)\ Pt + (1/2)H_2 \rightarrow Pt\text{-}H$$

$$(2)\ Pt + (1/2)O_2 \rightarrow Pt\text{-}O$$

$$(3)\ Pt\text{-}O + (3/2)H_2 \rightarrow Pt\text{-}H + H_2O$$

3.2.8 Scanning Electron/Transmission Electron Microscopy

Field Emission Scanning Electron Microscopy (FE-SEM) images were obtained on a JEOL LEO-1530 at a landing energy of 10kV. The sample powder was spread on a carbon coated sample mount and gold-coated to prevent surface charging effects. Optimum images were taken with 'In Lens' detector mode and 9 mm of working distance.

Field Emission Tranmission Electron Microscopy (FE-TEM) images were taken with a Hitachi HF-2000 at 200 kV accelerating voltage. The powder samples were first dispersed in water sonication. A few drops of sample solution were placed on a carbon-coated TEM grid (lacey) followed by drying in an 80°C oven. The optimum images were

taken at the lowest contrast condition in the middle of over-focusing and under-focusing condition.

3.3 Results

3.3.1 XRD

Untreated γ-alumina shows the expected diffraction pattern characteristic of the defective spinel structure with the two main peaks located at 2θ = 45.8° and 67° corresponding to the (400) and (440) crystal planes, respectively (Figure 3.1).[1] The formation of small crystalline peaks is observable within the first hour of the treatment. These peaks increased in intensity with increasing treatment time. The crystal phase is identified as boehmite through comparison to a standard reference diffractogram with the main peaks located at 2θ = 14.5°, 28.2°, 38.3°, 49° and 49.3° corresponding to the (020), (120), (140, 031), (051) and (200) crystal planes, respectively (Figure 3.1).[1,16]

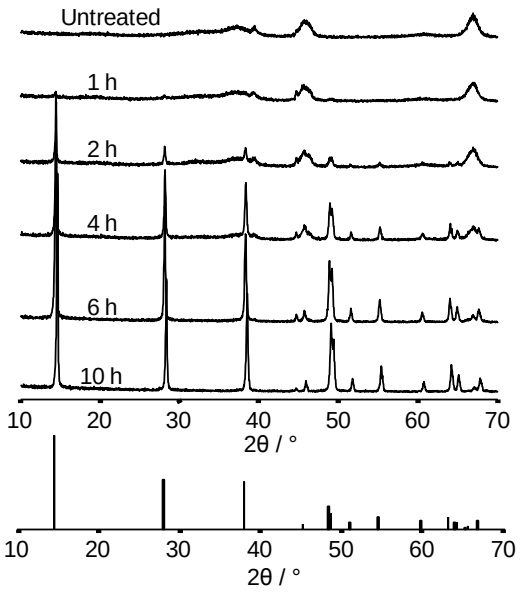

Figure 3.1: X-ray diffractograms of γ-Al_2O_3 treated at 200 °C and saturation pressure for various durations.

The x-ray diffractograms of the untreated supported metal catalysts did not exhibit distinct peaks corresponding to metal particles. Comparison of the x-ray diffractograms of bare γ-Al_2O_3 with the supported metal catalysts indicates that the crystallization occurs more slowly when metal particles are present (Figure B.1). After 10 h of treatment, Ni/γ-Al_2O_3 has more intense refraction of the main peaks at 2θ = 14.5°, 28.2°, and 38.3° compared to Pt/γ-Al_2O_3. The platinum loaded catalyst also shows evidence of the (400) crystal plane of γ-Al_2O_3 at 2θ = 45.8°.[1] Due to the limited quantitative information in the x-ray diffractograms, ^{27}Al NMR spectroscopy was used to measure the extent of phase transformation.

3.3.2 ^{27}Al MAS NMR Spectroscopy

The ^{27}Al MAS NMR spectra of the untreated samples contain resonances at 8 ppm and 70 ppm, which are attributed to octahedrally and tetrahedrally coordinated aluminum species, respectively (Figures 3.2 and B.2).[17-18]

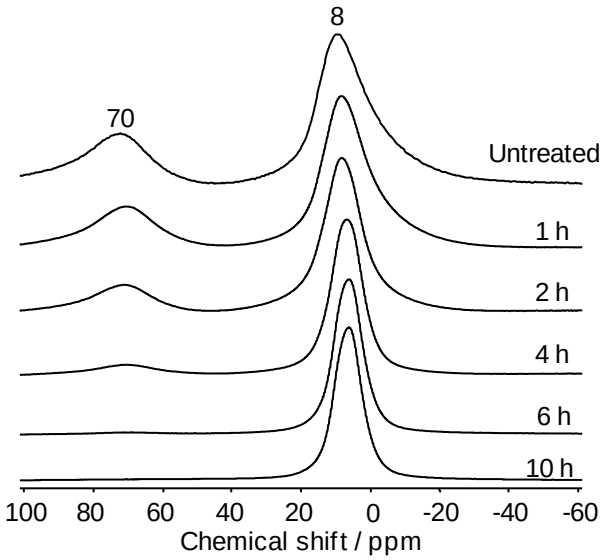

Figure 3.2: ^{27}Al NMR spectra of γ-Al_2O_3 treated at 200 °C and saturation pressure for various durations.

This shows an expected distribution of Al nuclei between two different positions in γ-alumina.[8] Untreated γ-Al_2O_3 contained 28% of aluminum in tetrahedral coordination (Al_T) consistent with previous investigations.[19-20] In contrast, all aluminum atoms in boehmite are octahedrally coordinated.[18] The fraction of Al present as boehmite in each sample was determined by linear combination of the ^{27}Al MAS NMR spectra of γ-Al_2O_3 and boehmite (Figure 3.3). In order to verify the quantitative validity of using the ^{27}Al MAS NMR spectra for kinetic analysis, it was necessary to discount the possibility of "invisible" distorted penta-coordinated aluminum contributing to signal intensity. Therefore, the boehmite fraction calculated from the ^{27}Al MAS NMR spectra was compared to thermogravimetic analysis and the values were in good agreement (Figure B.4, Table B.1). These results indicate that all aluminum was visible via NMR spectroscopy and that the spectroscopic method of boehmite quantification is valid.

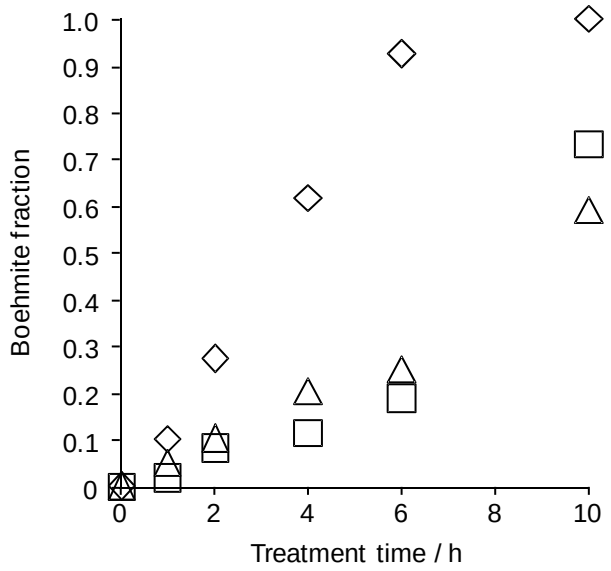

Figure 3.3: Kinetics of boehmite formation during treatment in liquid water at 200 °C: ◊ = γ-Al_2O_3, Δ = 1 wt% Pt/γ-Al_2O_3, □ = 1 wt% Ni/γ-Al_2O_3.

Alumina was essentially completely converted to boehmite over the first 6 h at a linear rate of 0.152 mole fraction·h^{-1}. It can also be seen that mostly octahedrally coordinated species (Al_O) were present after 6 h of treatment (Figure 3.2). For the metal loaded samples, the Al_T resonance was observable over longer treatment times than for the bare support (Figure B.2). This is consistent with the XRD results, indicating a delayed formation of boehmite for the metal containing samples. The metal loaded samples form boehmite particularly slowly during the first 6 h with linear rates of 0.045 and 0.031 mole fraction·h^{-1} for Pt/γ-Al_2O_3 and Ni/γ-Al_2O_3, respectively. After 6 h of treatment, Pt/γ-Al_2O_3 and Ni/γ-Al_2O_3 both increase to 0.086 and 0.136 mole fraction·h^{-1}, respectively. It is interesting to note the similarity in the phase transition kinetics for both catalyst materials with 73% conversion for Ni/γ-Al_2O_3 after 10 h compared to 60% for Pt/γ-Al_2O_3. Note that there are approximately 3.3 times as many metal atoms in the Ni catalyst.

3.3.3 ^{1}H MAS NMR Spectroscopy

The ^{1}H NMR spectra of γ-Al_2O_3 showed 6 peaks located at 5.8 ppm, 4.0 ppm, 2.4 ppm, 1.5 ppm, 0.7 ppm, -0.1 and -0.4 ppm (Figure 3.4).

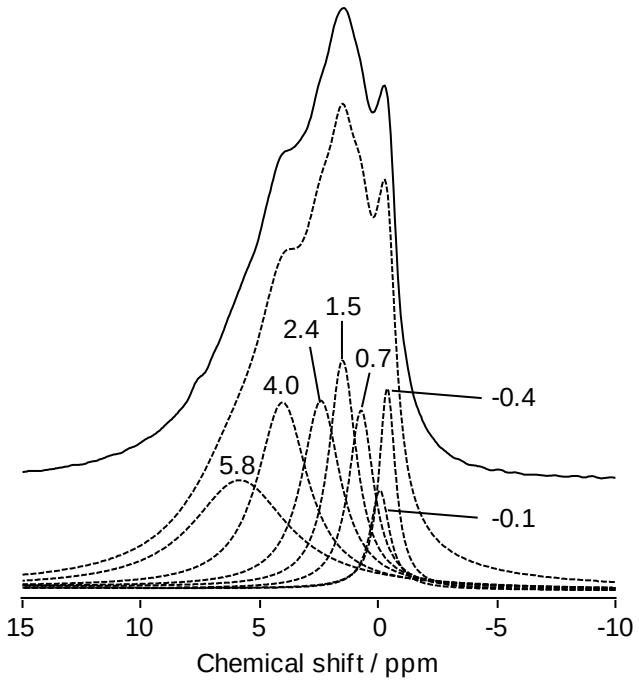

Figure 3.4: Normalized ^{1}H NMR spectra of untreated γ-Al_2O_3 (solid line) and peak deconvolution (dashed lines).

The peaks at 5.8 and 4.0 ppm are attributed to adsorbed water, leaving 5 OH surface species.[21] The high field signals at -0.4 and -0.1 ppm indicate hydroxyl groups attached to a single Al atom, whereas the resonances at 0.7 and 1.5 ppm are attributed to Al-OH-Al species and the peak at 2.4 ppm is assigned to an OH coordinated to three Al atoms.[21] This is consistent with the surface model of γ-Al_2O_3 proposed by Knözinger and Ratnasamy, which postulates 5 types of possible surface hydroxyl groups, 3 of which involve oxygen bridging neighboring aluminum atoms (Al_T-OH-Al_O, Al_O-OH-Al_O, and $3Al_O$-OH).[22]

In order to quantify hydroxyl group concentration, peak decomposition was performed and the areas compared to an adamantane standard (Figure 3.4, Table 3.1). From this comparison, the OH group density of untreated γ-Al_2O_3 is calculated to be 0.89

mmol·g^{-1}, or 5.9 OH groups·nm^{-2} (water signals not included). This value is lower than other ^{1}H NMR investigations of dehydrated γ-alumina that have shown a hydroxyl group density of 8.5 OH·nm^{-2}.[23] It should also be noted that different γ-alumina samples will have different hydroxyl group densities depending on their structure.

A comparison of the ^{1}H NMR spectra of untreated γ-alumina and the catalysts demonstrated a change in the hydroxyl group concentration upon addition of metal (Figure B.3, Table 3.1). Ni/γ-Al_2O_3 showed comparable decreases in all hydroxyl group concentrations in the range of 19 – 25%. The platinum catalyst showed the most significant decrease in the singly coordinated OH group resonating at -0.4 ppm with a 53% decrease in concentration. The rest of the hydroxyl groups did not change appreciably.

Table 3.1: Hydroxyl coverage of untreated materials as measured by ^{1}H MAS NMR spectroscopy.

^{1}H NMR Peak Resonance	**γ-Al_2O_3**	**1 wt% Ni/γ-Al_2O_3**		**1 wt% Pt/γ-Al_2O_3**	
	C_{OH} / mmol·g^{-1}	**C_{OH} / mmol·g^{-1}**	**Δ / %**	**C_{OH} / mmol·g^{-1}**	**Δ / %**
δ = 2.4 ppm *3Al(OH)*	0.27	0.20	-25.38	0.25	-7.80
δ = 1.5 ppm *2Al(OH)*	0.24	0.15	-38.45	0.25	5.85
δ = 0.7 ppm *2Al(OH)*	0.17	0.12	-27.89	0.17	0.01
δ = -0.1 ppm *Al(OH)*	0.07	0.04	-38.48	0.08	8.34
δ = -0.4 ppm *Al(OH)*	0.13	0.08	-34.63	0.06	-52.59

3.3.4 Pyridine Adsorption/IR Spectroscopy

The acidity of treated and untreated γ-Al_2O_3 samples was analyzed by pyridine adsorption followed by IR spectroscopy as described elsewhere.[13,24-25] The absence of a band at 1540 cm^{-1} indicated that there are no Brønsted acid sites capable of protonating pyridine on untreated γ-alumina, or any of the other samples.[13,26] The concentration of Lewis acid sites (LAS) was quantified based on the intensity of the characteristic band at 1451 cm^{-1} (Figure 3.5).

Untreated γ-Al_2O_3 had a LAS concentration of 342 μmol·g^{-1} (Figure 3.5). A notable decrease of the LAS concentration from 304 μmol·g^{-1} to 42 μmol·g^{-1} was observed between 2 and 6 h of treatment time.

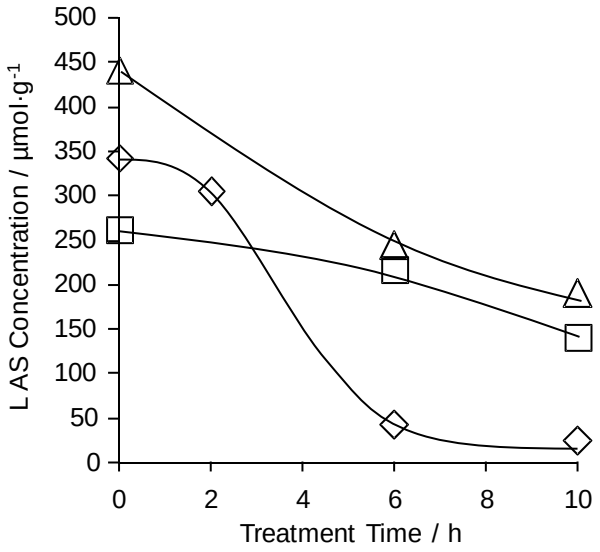

Figure 3.5: Change in Lewis acid site (LAS) concentration as a function of treatment time as measured by adsorbed pyridine: ◊ = γ-Al_2O_3, Δ = 1 wt% Pt/γ-Al_2O_3, □ = 1 wt% Ni/γ-Al_2O_3.

The LAS concentration of untreated Ni/γ-Al_2O_3 was lower than that of alumina at 262 μmol·g^{-1}. After 6 h of treatment, the total site count decreased to 216 μmol·g^{-1}. After 10 h,

140 μmol·g^{-1} total sites remained which is a 53% overall decrease compared to the untreated material. The untreated Pt/γ-Al_2O_3 catalyst contained a higher LAS concentration relative to untreated γ-alumina at 441 μmol·g^{-1}. After 6 h of treatment, the total LAS dropped to a value of 243 μmol·g^{-1}. At the end of the 10 h treatment, 189 μmol·g^{-1} total sites remained, 43% of the initial value. The platinum catalyst, like the nickel catalyst, exhibits a more steady decrease in acid site count over the course of treatment than alumina. The relative decrease in total LAS concentration correlated with increasing conversion of alumina to boehmite (Figure 3.6).

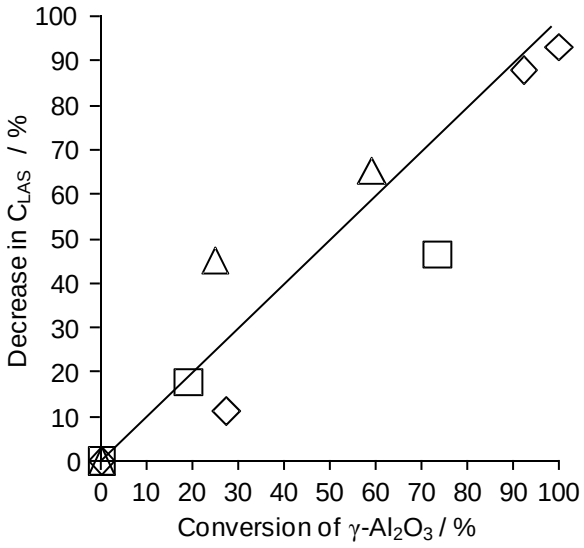

Figure 3.6: Decrease in Lewis acid site (LAS) concentration as a function of support conversion: ◊ = γ-Al_2O_3, Δ = 1 wt% Pt/γ-Al_2O_3, □ = 1 wt% Ni/γ-Al_2O_3.

3.3.5 Nitrogen Physisorption

Untreated γ-Al_2O_3 had an initial surface area of ca. 90 m^2·g^{-1} while the surface are of both metal containing samples was approximately 70 m^2·g^{-1} (Figure 3.7). Initially,

hydrothermal treatment led to an increase in surface area. For metal free γ-Al_2O_3 a maximum of 104 $m^2 \cdot g^{-1}$ was observed after 2 h of treatment followed a sharp decline to 32 $m^2 \cdot g^{-1}$ after 6 h.

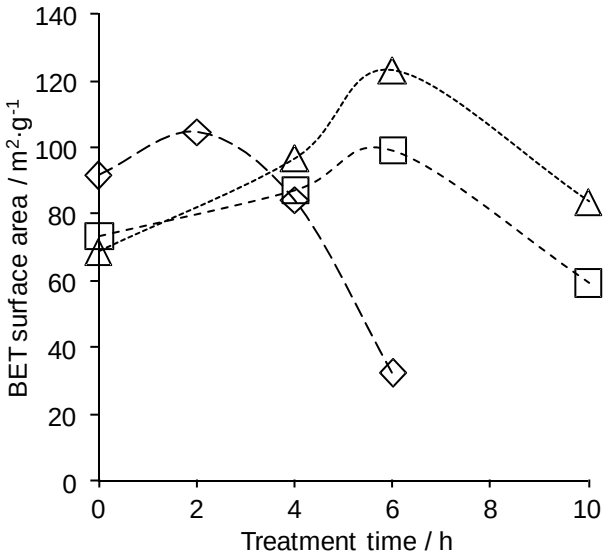

Figure 3.7: Changes in catalyst surface area relative to treatment time as measured by N_2 physisorption. (◊ = γ-Al_2O_3, Δ = Pt/γ-Al_2O_3, □ = Ni/γ-Al_2O_3).

In contrast, the surface area of both supported metal catalysts increased for the first 6 h of treatment and decreased less sharply when the treatment time was extended. Note that the platinum catalyst after 10 h of treatment retained a higher surface area (84 $m^2 \cdot g^{-1}$) than the untreated sample (69 $m^2 \cdot g^{-1}$) whereas the nickel catalyst had a surface area of 59 $m^2 \cdot g^{-1}$ after 10 h compared to 73 $m^2 \cdot g^{-1}$ for the untreated material. Although N_2 physisorption may potentially underestimate surface areas of poorly crystalline boehmite,[27] it provides a common indicator of surface areas.

3.3.6 H_2/O_2 Titration

The metal dispersion of the platinum catalysts was measured by pulse chemisorption method (Table 3.2). A slight increase in dispersion was observed over the first 4 hours, whereas the the dispersion was reduced to 21% after 10 hour of treatment. Ni/Al_2O_3 samples were not analyzed because it is difficult to obtain reliable estimation of Ni dispersions at low loadings (i.e. less than 3 wt%) due to strong metal support interactions.[28]

Table 3.2: Summary of metal particle characteristics for untreated platinum catalyst and samples treated for 4 h and 10 h at 200 °C and saturation pressure.

Catalyst	Dispersion (%)	Metallic surface area ($m^2 \cdot g^{-1}$)	Active particle diameter (nm)
Pt/γ-Al_2O_3, untreated	70.2	1.73	1.61
Pt/γ-Al_2O_3, treated 4 h	78.4	1.94	1.45
Pt/γ-Al_2O_3, treated 10 h	21.2	0.523	5.35

3.3.7 Electron Microscopy

TEM images of both untreated $Pt/\gamma\text{-}Al_2O_3$ and $Ni/\gamma\text{-}Al_2O_3$ indicate metal particle sizes between 0.5 and 2.0 nm with average sizes of 1.0 and 1.2 nm, respectively (Figure 3.8). The metal particles remained in the size range between 0.5 and 2.0 nm after 4 h of treamtent for $Pt/\gamma\text{-}Al_2O_3$ and $Ni/\gamma\text{-}Al_2O_3$ (Figure 3.9). After 10 h, the particle size distribution shifted to larger particles for both samples. Specifically, 12% of Pt particles and 16% of the Ni particles exceeded 2 nm while average metal particle sizes were 1.7 and 1.6 nm for $Pt/\gamma\text{-}Al_2O_3$ and $Ni/\gamma\text{-}Al_2O_3$, respectively. After treatment for 10 h, Pt

particles as large as 8 nm were observed in addition to enhanced contrast (Figure B.5). For Ni/γ-Al_2O_3, the contrast between nickel particles and alumina pore structure was less pronounced as has been observed by others with such low nickel loading.[29] This may be due to the presence of unreduced NiO particles which have similar extinction distances to the γ-Al_2O_3 (400) plane making contrast resolution more difficult.[15]

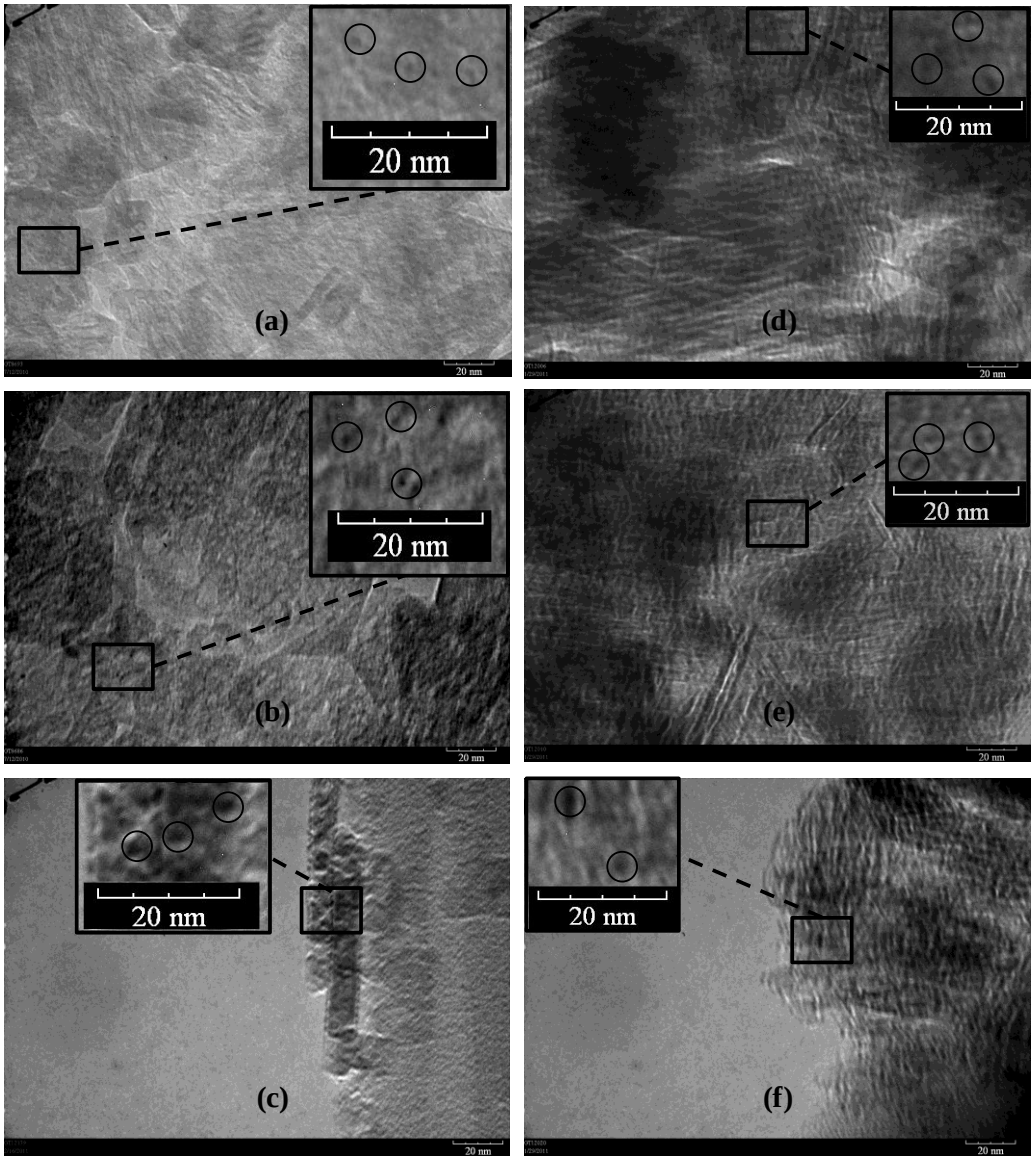

Figure 3.8: TEM analysis of 1 wt% Pt/γ-Al_2O_3 untreated (a), treated for 4 h (b) and treated for 10 h (c) and 1 wt% Ni/γ-Al_2O_3 untreated (d), treated for 4 h (e) and treated for 10 h (f) at 200 °C and saturation pressure.

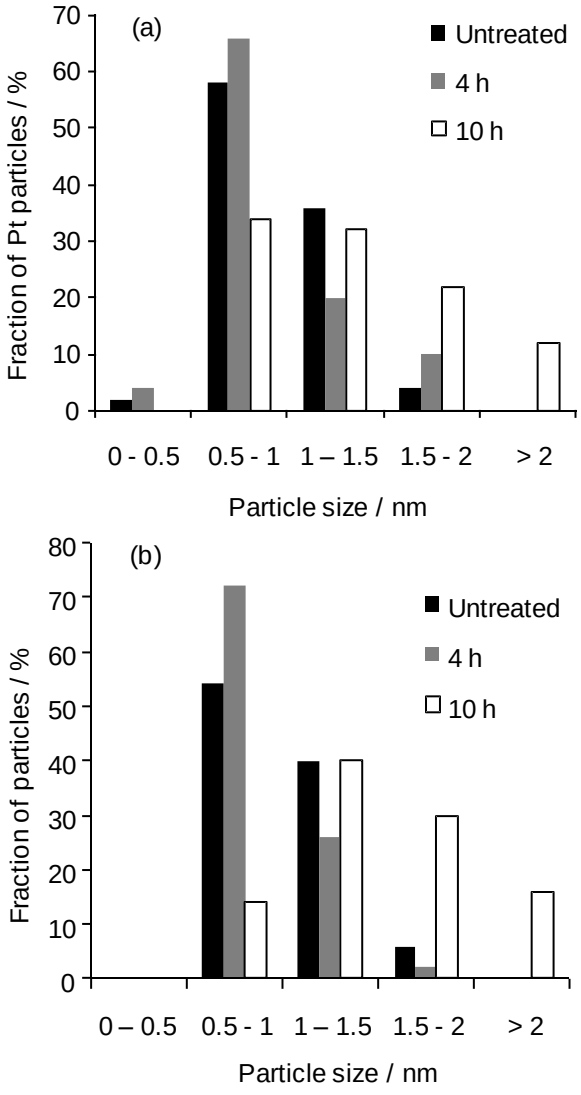

Figure 3.9: Metal particle histograms as measured by TEM for 1 wt% Pt/γ-Al_2O_3 (a) and 1 wt% Ni/γ-Al_2O_3 (b) for untreated and samples treated at 200 °C and saturation pressure.

SEM images of the Pt/γ-Al_2O_3 samples show that the alumina particles tend to agglomerate and form compact sheet-like structures over the course of treatment (Figure

3.10). The untreated Pt/Al_2O_3 had some large observable particles up to ca. 450 nm in size, while most were in the range of 100 nm or less. After 4 h of treatment, particles larger than 1100 nm were observed with many smaller clusters ca. 200 nm in diameter. At the same time the surface roughness decreased markedly.

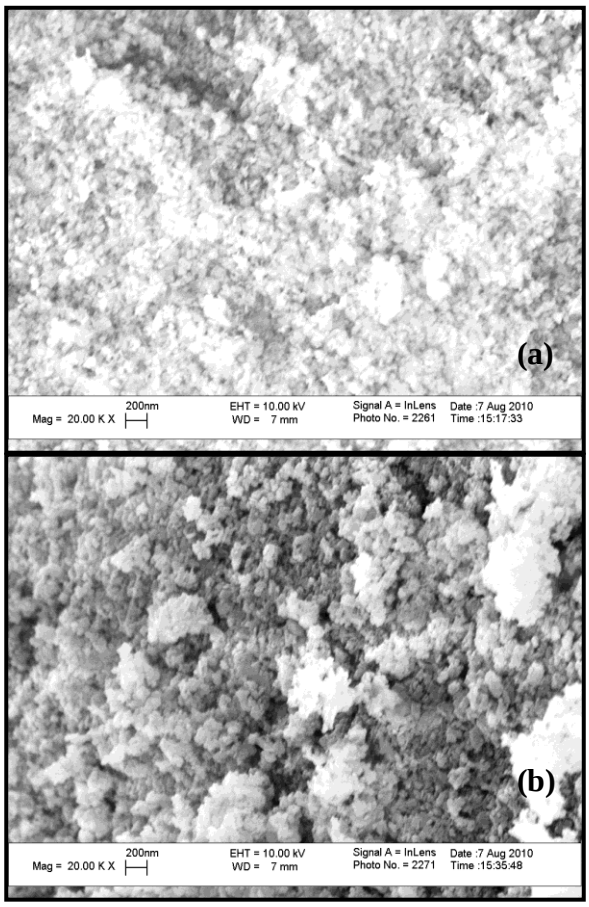

Figure 3.10: SEM analysis of 1 wt% $Pt/\gamma\text{-}Al_2O_3$ untreated (a) and the sample treated for 4 h (b) at 200 °C and saturation pressure.

3.4 Discussion

3.4.1 Stability of γ-Al_2O_3 in Hot Liquid Water

As γ-Al_2O_3 is prepared from the dehydration of gibbsite mineral,[8] $Al(OH)_3$, it is not surprising that under hydrothermal treatment it reverts to back to a hydrated form. The phase changes of aluminum oxides and hydroxides under steaming conditions are dependent on a number of factors including particle size, concentration of steam, and heating rate (Figure 3.11).[30-31]

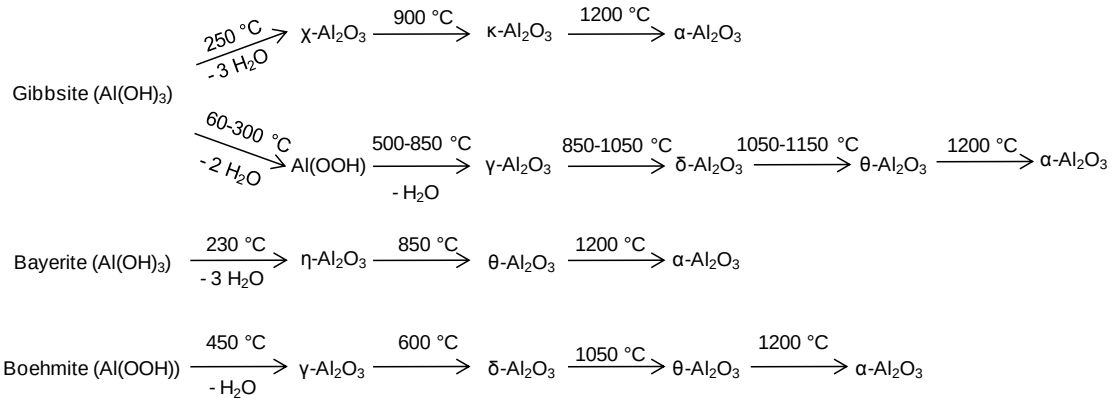

Figure 3.11: Dehydroxylation sequences of alumina hydrates.

The thermodynamic stability of different phases in liquid water depends on the temperature, pH, and potential of the solution.[9] However, these transformations have been overlooked in a considerable number of publications, particularly in studies utilizing alumina supported catalysts for conversion of biomass in water at elevated temperatures. This may be a critical oversight, as the alumina phase can have a significant impact on activity. For example, platinum supported on a mixed phase alumina support lead to ca. a six fold increase in the hydrogen production rate from aqueous phase reforming (APR) of glycerol compared to platinum supported on γ-alumina alone.[32] Therefore, the stability of

metal oxide supports and γ-Al_2O_3 in particular must be an important consideration in the development of heterogeneous catalysts.

Hydration of alumina at room temperature is a process which can take weeks for appreciable conversion, and both pH and calcination conditions can have significant effects on which phase is formed.[33-34] One study even reported on hydration at room temperature over the course of 6 months with bayerite as the main product.[35] The formation of boehmite from γ-Al_2O_3 synthesized by the sol-gel method was reported after this material was treated at 200 °C in liquid water under autogeneous pressure for several days.[36] The current study shows that γ-Al_2O_3 based catalysts undergo significant transformations on much shorter time scales.

Reaction kinetics based on quantitative analysis of ^{27}Al MAS NMR spectra showed that the concentration of boehmite formed from the bare γ-alumina support increased linearly over the course of the first 6 h, after which 92% of the material had been converted (Figure 3.3). It is important to note that the XRD peaks after 1 and 2 h of treatment were rather low in intensity indicating the lack of long-range order in the hydrated alumina phases in these samples (Figure 3.1). The formation of first hydrated alumina phases was accompanied by a 14% increase in the surface area. This observation is tentatively assigned to the formation of small patches of boehmite that are attached to the alumina surface. Pitting of the alumina phase due to migration of Al atoms to the boehmite patch may also contribute to the increase in surface area. After 2 h a decrease in the surface area accompanied by a notable increase of the intensity of the XRD peaks indicated the formation of a compact crystalline boehmite phase. The formation of compact particles was also observed in the SEM images (Figure 3.10). Note that an initial

increase of the surface area followed by an eventual decrease was also observed for the phase transformation of gibbsite crystals to boehmite in water vapor.[37] The authors suggested a mechanism including dissolution of aluminum atoms from non equilibrium phase followed by nucleation and growth of stable boehmite (AlOOH) crystals.

3.4.2 Effect of Metal Particles on Boehmite Formation

Although the formation of boehmite has been reported for supported metal catalysts before,[10-11] the effect of metal particles on the kinetics of boehmite formation on this time scale have not been investigated in detail. A recent study of 17 wt% Ni/γ-Al_2O_3 in the temperature range of 90 °C - 150 °C over the course of 48 h concluded that the nickel particles did not affect the hydration of γ-Al_2O_3.[38] Although the influence of treatment time and temperature were investigated, there was no direct comparison of the degree of hydration of the metal loaded sample and the bare support.

The x-ray diffractograms and ^{27}Al MAS NMR spectra in this study indicate that the presence of metal particles results in a significant decrease of the rate of boehmite formation from γ-Al_2O_3. Specifically, the initial rates of boehmite conversion are 0.10 mole fraction$\cdot h^{-1}$ for γ-Al_2O_3, 0.05 mole fraction$\cdot h^{-1}$ for the Pt catalyst, and 0.02 mole fraction$\cdot h^{-1}$ for the Ni catalyst. This effect is quite significant considering the catalysts only contained 1 wt% of Pt and Ni, respectively. Based on the TEM analysis of the untreated 1 wt% Pt/γ-Al_2O_3, the average metal cluster size is approximately 1.0 nm (Figure 3.9). Assuming that the particles consist of a monolayer of metal, the average Pt particles consist of about 13 Pt atoms (Pt atomic radius = 139 pm). At the present metal loading of 1 wt% the Pt particles only cover ca. 2% of the total surface area of γ-Al_2O_3 (BET surface area = 90 m^2/g). The same analysis of Ni/γ-alumina results in about 23

atoms/cluster covering ca. 5.5% of available surface area. Considering that such a small fractional coverage results in a significant change in the kinetics of boehmite formation, it appears that the metal particles cover a relatively small number of specific surface sites that play a critical role in the hydration process.

The ^{1}H NMR spectra clearly show that the addition of metal particles reduces the concentration of surface hydroxyl groups (Figure B.3). It is well established that the metal precursors bind to these sites during wet diffusional impregnation (i.e. wet impregnation).[39-40] The present data indicate that the metal particles remain in these locations after calcinations. Integration of the spectra indicated an 8.3% decrease in overall concentration of OH groups for the platinum catalyst and a 31.8% decrease for the nickel catalyst showing that the number of blocked hydroxyl groups in 1 wt% Ni/γ-Al_2O_3 is ca. 3.8 times higher than in 1 wt% Pt/γ-Al_2O_3. This is in general agreement with the molar ratio of nickel/platinum atoms (3.3) in samples containing 1 wt% metal. It is interesting to note that 1.7 and 1.3 surface hydroxyl groups were consumed per nickel and platinum atom, respectively. Similar observations were reported in a study on grafting molybdates on γ-Al_2O_3 surfaces.[23] Analysis of the ^{1}H MAS NMR spectra shows that platinum particles preferentially bind to the singly coordinated OH group resonating at -0.4 ppm. Incorporation of nickel particles reduced the concentration of all OH species with a slight preference for singly coordinated hydroxyl groups. Note that the singly coordinated species are the most basic surface hydroxyl groups.[41]

Since it appears that the metal particles are associated with surface hydroxyl groups, it is hypothesized that the decrease in the rate of hydration is caused by the decrease in concentration of these hydroxyl groups. There are two possible effects that can explain

these results: (1) metal particles block sites that are important for nucleation of boehmite crystals, or (2) surface bound metal particles prevent hydration of the support.

The first mechanism seems less likely considering that notable boehmite formation occurs even within the first hour of treatment of the metal catalysts as shown by the ^{27}Al MAS NMR analysis. If the metal particles were blocking nucleation sites, a measureable conversion of the support would not be expected. Evidence for the second mechanism is provided by the comparison of surface area to the rate of boehmite formation. For all samples the maximum in the surface area was observed when 23±4% of the support had been converted to boehmite. The subsequent decrease in surface area was accompanied by a notable increase of the XRD peaks. This critical stage occurs significantly later when metal particles are present. Therefore, it is plausible that metal particles effectively hinder the formation of the initial boehmite patches. Since the platinum and nickel catalysts exhibit comparable rates of boehmite formation, and platinum only shows association with basic surface hydroxyl groups, we speculate that these OH groups may play a key role in initiating the hydration.

The chemisorption analysis indicates that metal dispersion remains constant for the first 4 h of the treatment but decreases dramatically when the treatment is extended from 4 to 10 h (Table 3.2). This is attributed to metal sintering as confirmed by TEM analysis. It has been shown that metal particles do not sinter on supports that are stable in hot liquid water,[11] whereas notable sintering occurs on less stable supports.[11,38] Therefore, it is suggested that sintering is triggered by erosion of the support around the metal particles.

3.4.3 Surface Acidity

It is well known that the concentration and strength of acid sites have an enormous influence on the activity and selectivity of catalysts. Some have reported the formation of Brønsted acid sites by dissociative chemisorption of water on α- and γ-alumina.[41-42] Re-calcination of hydrated aluminas has shown an increase in total acidity compared to the original alumina,[36] while others have shown decreases in acid site concentration of re-calcined samples.[34]

In the present study, the concentration of acid sites was probed by adsorption of pyridine followed by IR spectroscopy. This technique allows for identification of pyridine in specific environments (e.g. adsorbed on Brønsted or Lewis acid sites) and, thus, avoids the lack of specificity of surface interaction of ammonia.[43] No Brønsted acid sites were found on untreated γ-Al_2O_3 and boehmite. It was suggested previously that even the most acidic surface OH groups in γ-Al_2O_3 lack the necessary strength to protonate pyridine to form an adsorbed pyridinium ion.[44] The present results indicate that the same is true for surface hydroxyl groups in boehmite and partially hydrated alumina samples.

A decrease in the LAS concentration as a function of treatment time was positively correlated with fraction of γ-alumina converted to boehmite (Figure 3.6). These results are not surprising considering the structural differences between the two materials. γ-Alumina has a defect spinel structure with aluminum cations found in both tetrahedral and octahedral coordination. Lewis acidity requires coordinatively unsaturated species, and the concentration of these depends on the exposed face.[45] Typically, Lewis acid sites are associated with tetrahedrally coordinated Al atoms although they may also be

generated from octahedrally coordinated Al species by desorption of non-bridged terminal hydroxyl groups.[46] During hydration, water dissociatively adsorbs on the Lewis acid sites to form boehmite, which only contains octahedrally coordinated aluminum..[42] Therefore, boehmite would be expected to have a lower concentration of Lewis acid sites.[47] It is interesting to note that the concentration of Lewis acid sites decreased linearly with increasing concentration of boehmite. This observation implies that the hydration of bulk aluminum oxide occurs at the same rate as the consumption of accessible Lewis acid sites.

The acid site analysis also revealed an increase in the LAS concentration for the untreated Pt/γ-Al_2O_3 compared to untreated γ-Al_2O_3. It is suggested that this increase arises from modifications of the surface by residual chlorine anions from the H_2PtCl_6 precursor salt. Treatment of Pt/Al_2O_3 catalyst with NH_4Cl was shown to increase the strength and concentration of Lewis acid sites on the support.[48] Adsorption of trimethylphosphine followed by ^{31}P MAS NMR spectroscopy revealed that the concentration of strong LAS increased while the concentration of weak acid sites decreased after chlorination.[49]

3.4.4 Relevance for Catalyst Design

The transformations observed in the present work are expected to have a significant effect on the performance of heterogeneous catalysts in aqueous phase reactions. For example, Pt/Al_2O_3 catalysts have been used for the production of hydrogen and/or alkanes from biomass-derived oxygenates by aqueous phase reforming.[2,5,50] Alkanes are formed via a combination of acid catalyzed dehydration steps and metal catalyzed hydrogenation. For production of hydrogen, C-C, C-H and O-H bonds are cleaved on

metal sites followed by water-gas shift reaction.[2,5] As expected, the selectivity towards alkanes increases with increasing acidity of the support.[51] Based on the present results, it is expected that a shift in selectivity to hydrogen will occur gradually until the entire support has been converted to boehmite. However, metal sintering should also influence the activity and/or selectivity. It is likely that loss in active metal surface area due to particle sintering will lower overall activity.

The presence of surface hydroxyl groups in boehmite supported catalysts may also have synergistic effects in metal catalyzed reactions. A recent publication reported an increased activity and selectivity for the hydrogenation of methyl propionate over RuPt/boehmite compared to RuPt/γ-Al_2O_3.[52] The authors proposed that the hydroxyl sites polarize the C=O group of the reactant rendering it more susceptible to hydrogenation.

Reclamation of spent alumina catalysts from boehmite is a possibility and has been demonstrated by treatment with caustic soda followed by thermal treatment.[53] Such treatment would result in sintering of metal particles requiring further steps to then dissolve and capture the metals for recycle, increasing energy and unit operation costs. Perhaps a more desirable approach would be to alter the support in an effort to prevent hydration. As we have demonstrated that metal deposition can affect hydration kinetics, so it may be possible to enhance the stability of γ-Al_2O_3 supported catalysts in hot liquid water by eliminating initial hydration sites for boehmite formation. This may be achieved by capping these sites via a post-synthesis treatment. It should also be considered whether boehmite is a good support for specific catalytic reactions in aqueous phase. The use of a thermodynamically stable phase would prevent undesirable changes of the structure and properties of solid catalysts.

3.5 Conclusions

In summary, we have demonstrated that significant transformations of alumina supported catalysts occur in aqueous phase, which can strongly affect their performance in catalytic reactions. Specifically, γ-alumina forms a hydrated boehmite phase with significant changes in surface area and acidity. Note that this transformation may lead to deactivation or enhanced activity for specific reactions. Supported metal particles decrease the rate of the transformation of γ-alumina support to boehmite. We postulate that associated metals hinder initial boehmite formation by effectively blocking surface hydroxyl groups important for hydration. The metal particles also exhibit sintering behavior over the course of treatment, with the most significant sintering happening after 10 h of treatment. In conclusion, structural changes in aqueous environments must be considered in designing efficient catalysts for biomass reforming in aqueous media. We suggest that alteration of the alumina support by blocking surface hydroxyl sites may be a way to design more robust catalysts for such reactions.

3.6 References

[1] Wefers, K.; Misra, C. *Alcoa Technical Paper* **1987**.

[2] Shabaker, J. W.; Davda, R. R.; Huber, G. W.; Cortright, R. D.; Dumesic, J. A. *Journal of Catalysis* **2003**, *215*, 344-352.

[3] Tanksale, A.; Wong, Y.; Beltramini, J. N.; Lu, G. Q. *International Journal of Hydrogen Energy* **2007**, *32*, 717-724.

[4] Shabaker, J. W.; Huber, G. W.; Davda, R. R.; Cortright, R. D.; Dumesic, J. A. *Catalysis Letters* **2003**, *88*, 1-8.

[5] Cortright, R. D.; Davda, R. R.; Dumesic, J. A. *Nature* **2002**, *418*, 964-967.

[6] Fukuoka, A.; Dhepe, P. L. *Angewandte Chemie - International Edition* **2006**, *45*, 5161-5163.

[7] Valenzuela, M. B.; Jones, C. W.; Agrawal, P. K. *Energy & Fuels* **2006**, *20*, 1744-1752.

[8] Holleman, A. F.; Wiberg, E. *Inorganic Chemistry, 34th Edition*; Academic Press, **2001**.

[9] MacDonald, D. D.; Butler, P. *Corrosion Science* **1973**, *13*, 259-274.

[10] Luo, N.; Fu, X.; Cao, F.; Xiao, T.; Edwards, P. P. *Fuel* **2008**, *87*, 3483-3489.

[11] Ketchie, W. C.; Maris, E. P.; Davis, R. J. *Chemistry of Materials* **2007**, *19*, 3406-3411.

[12] Ravenelle, R. M.; Schüβler, F.; D'Amico, A.; Danilina, N.; van Bokhoven, J. A.; Lercher, J. A.; Jones, C. W.; Sievers, C. *The Journal of Physical Chemistry C* **2010**, *114*, 19582-19595.

[13] Datka, J.; Turek, A. M.; Jehng, J. M.; Wachs, I. E. *Journal of Catalysis* **1992**, *135*, 186-199.

[14] Benson, J. E.; Boudart, M. *Journal of Catalysis* **1965**, *4*, 704-710.

[15] Delannay, F., Ed. *Characterization of Heterogeneous Catalysts*; Marcel Dekker: New York, **1984**; Vol. 15.

[16] Linsen, B. G.; Fortuin, J. M. H.; Okkerse, C.; Steggerda, J. J., Eds. *Pysical and Chemical Aspects of Adsorbents and Catalysts*; Academic Press: New York, **1970**.

[17] Pecharroman, C.; Sobrados, I.; Iglesias, J. E.; Gonzalez-Carreno, T.; Sanz, J. *The Journal of Physical Chemistry B* **1999**, *103*, 6160-6170.

[18] Urretavizcaya, G.; Cavalieri, A. L.; López, J. M. P.; Sobrados, I.; Sanz, J. *Journal of Materials Synthesis and Processing* **1998**, *6*, 1-7.

[19] Zhou, R. S.; Snyder, R. L. *Acta Crystallographica Section B-Structural Science* **1991**, *47*, 617-630.

[20] John, C. S.; Alma, N. C. M.; Hays, G. R. *Applied Catalysis* **1983**, *6*, 341-346.

[21] Decanio, E. C.; Edwards, J. C.; Bruno, J. W. *Journal of Catalysis* **1994**, *148*, 76-83.

[22] Knözinger, H.; Ratnasamy, P. *Catalysis Reviews: Science and Engineering* **1978**, *17*, 31-70.

[23] Kraus, H.; Prins, R. *Journal of Catalysis* **1996**, *164*, 260-267.

[24] Emeis, C. A. *Journal of Catalysis* **1993**, *141*, 347-354.

[25] Kondo, J. N.; Nishitani, R.; Yoda, E.; Yokoi, T.; Tatsumi, T.; Domen, K. *Physical Chemistry Chemical Physics* **2010**, *12*, 11576-11586.

[26] Morterra, C.; Emanuel, C.; Cerrato, G.; Magnacca, G. *Journal of the Chemical Society-Faraday Transactions* **1992**, *88*, 339-348.

[27] Wang, S.-L.; Johnston, C. T.; Bish, D. L.; White, J. L.; Hem, S. L. *Journal of Colloid and Interface Science* **2003**, *260*, 26-35.

[28] Bartholomew, C. H.; Pannell, R. B. *Journal of Catalysis* **1980**, *65*, 390-401.

[29] Mustard, D. G.; Bartholomew, C. H. *Journal of Catalysis* **1981**, *67*, 186-206.

[30] Victoria, J. I.-J.; Robert, C. T. S.; Thomas, W. D.; Jennifer, C. S.; Sylvain, S. *Journal of Materials Chemistry* **1996**, *6*, 73-79.

[31] Kasprzyk-Hordern, B. *Advances in Colloid and Interface Science* **2004**, *110*, 19-48.

[32] Lehnert, K.; Claus, P. *Catalysis Communications* **2008**, *9*, 2543-2546.

[33] Carrier, X.; Marceau, E.; Lambert, J.-F.; Che, M. *Journal of Colloid and Interface Science* **2007**, *308*, 429-437.

[34] Rinaldi, R.; Fujiwara, F. Y.; Schuchardt, U. *Applied Catalysis A: General* **2006**, *315*, 44-51.

[35] Lefèvre, G.; Duc, M.; Lepeut, P.; Caplain, R.; Fédoroff, M. *Langmuir* **2002**, *18*, 7530-7537.

[36] Sanchez-Valente, J.; Bokhimi, X.; Hernandez, F. *Langmuir* **2003**, *19*, 3583-3588.

[37] Lopushan, V. I.; Kuznetsov, G. F.; Pletnev, R. N.; Kleshev, D. G. *Refractories and Industrial Ceramics* **2007**, *48*, 378-382.

[38] Li, H.; Xu, Y.; Gao, C.; Zhao, Y. *Catalysis Today* **2010**, *158*, 475-480.

[39] Ertl, G.; Knözinger, H.; Weitkamp, J., Eds. *Preparation of Solid Catalysts*; Wiley-VCH: New York, **1999**.

[40] Bourikas, K.; Kordulis, C.; Lycourghiotis, A. *Catalysis Reviews-Science and Engineering* **2006**, *48*, 363-444.

[41] Yang, X.; Sun, Z.; Wang, D.; Forsling, W. *Journal of Colloid and Interface Science* **2007**, *308*, 395-404.

[42] Raybaud, P.; Digne, M.; Iftimie, R.; Wellens, W.; Euzen, P.; Toulhoat, H. *Journal of Catalysis* **2001**, *201*, 236-246.

[43] Gorte, R. J. *Catalysis Letters* **1999**, *62*, 1-13.

[44] Morterra, C.; Magnacca, G. *Catalysis Today* **1996**, *27*, 497-532.

[45] Digne, M.; Sautet, P.; Raybaud, P.; Euzen, P.; Toulhoat, H. *Journal of Catalysis* **2002**, *211*, 1-5.

[46] Hirva, P.; Pakkanen, T. A. *Surface Science* **1992**, *277*, 389-394.

[47] Men, Y.; Gnaser, H.; Ziegler, C. *Analytical and Bioanalytical Chemistry* **2003**, *375*, 912-916.

[48] Beard, B. C.; Zhang, Z. C. *Catalysis Letters* **2002**, *82*, 1-5.

[49] Guillaume, D.; Gautier, S.; Despujol, I.; Alario, F.; Beccat, P. *Catalysis Letters* **1997**, *43*, 213-218.

[50] Huber, G. W.; Cortright, R. D.; Dumesic, J. A. *Angewandte Chemie - International Edition* **2004**, *43*, 1549-1551.

[51] Davda, R. R.; Shabaker, J. W.; Huber, G. W.; Cortright, R. D.; Dumesic, J. A. *Applied Catalysis B: Environmental* **2005**, *56*, 171-186.

[52] Zhou, Y.; Fu, H.; Zheng, X.; Li, R.; Chen, H.; Li, X. *Catalysis Communications* **2009**, *11*, 137-141.

[53] Al-Sheeha, H.; Marafi, M.; Stanislaus, A. *International Journal of Mineral Processing* **2008**, *88*, 59-64.

CHAPTER 4

METAL PRECURSOR EFFECTS ON γ-AL_2O_3 STABILITY AND ACTIVITY

4.1 Background

4.1.1 Metal precursors

The choice of metal precursor, in the present case platinum, depends on a variety of things including the type of support, synthesis procedure, and salt counter-ion effects. As wet impregnation is the technique utilized in this study, the variables affecting this particular procedure are considered. Foremost, depending on the impregnation solvent used, the solubility and melting point of the corresponding salt are important. If one is trying to facilitate strong electrostatic adsorption, then the ionic character of the metal complex is important. The solution pH (and hence catalyst surface charge) must be changed such that preferential adsorption of anions or cations is facilitated. The support stability/solubility as a function of pH may also dictate synthesis conditions. Therefore, it can easily be demonstrated that different metal precursors are suitable for different synthesis procedures; however, aside from synthesis considerations, the metal salt can alter catalyst activity.

It is well established that the Pt precursor influences the performance of Pt/γ-Al_2O_3 catalysts in many gas phase reactions. For example, Pt/γ-Al_2O_3 prepared by impregnation with platinum acetylacetonate (PtAcac) in toluene showed higher activity for n-pentane cracking/isomerisation than a catalyst prepared by impregnation with H_2PtCl_6 in water.[1] The higher activity was attributed to residual carbonaceous species that may increase

adsorption of organic reactants. Pt/γ-Al_2O_3 synthesized from H_2PtCl_6 had a higher turnover number for toluene hydrogenation compared to Pt/γ-Al_2O_3 synthesized from PtAcac, which was speculated to arise from presence of $Pt^{\delta+}$ species in the former.[2] As discussed in section 3.4.3, the precursor can affect acidity, especially if it contains chlorine (e.x. H_2PtCl_6).[3-4]

In this chapter, the effect of metal precursor on the aqueous phase conversion of cellulose to sorbitol is investigated, as no previous efforts of this nature are found in the literature. In order to better understand how the metal precursor can influence activity for this reaction, the mechanism is discussed in more detail in Section 4.1.2.

4.1.2 Mechanisms of Cellulose Hydrolysis and Hydrogenation by Supported Transition Metal Catalysts

The conversion of cellulose to sugar alcohols is a two-step process (Figure 4.1). The first reaction hydrolyzes cellulose β,1-4 linkages to individual glucose units, with hydrogen playing a proposed catalytic role. Subsequently, the glucose monomers undergo hydrogenation to sugar alcohols, or polyols (C-6 and smaller).

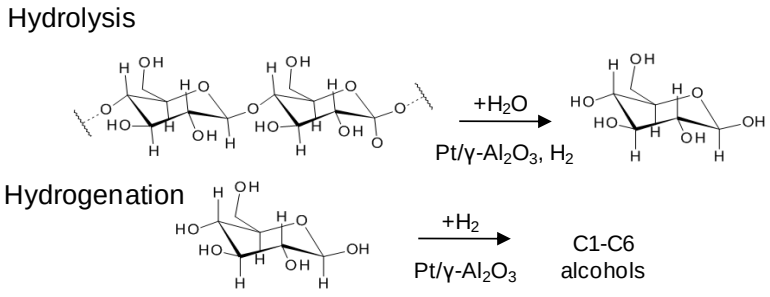

Figure 4.1: The two-step conversion of cellulose to sugar alcohols.

Fukuoka and Dhepe were the first to demonstrate catalytic conversion of cellulose to sugar alcohols such as sorbitol and mannitol in an H_2 pressurized reactor with a variety of supported metal catalysts, including Pt on multiple zeolites, metal oxides and activated carbon.[5] They also investigated Ru, Pd, Rh, Ni and Ir, but the greatest yield was observed utilizing a 2.5 wt% Pt/γ-Al_2O_3 catalyst (approximately 30% sugar alcohols).

The hydrolysis activity of the catalysts in these cases was not attributed to inherent acidity of the catalyst material, but rather in-situ formation of acid sites from dissociatively adsorbed hydrogen as proposed by Hattori et. al.[6] According to this theory, hydrogen molecules are dissociatively adsorbed on metal centers to form hydrogen atoms (Figure 4.2). The hydrogen atoms spill over onto the support and migrate to Lewis acid sites, where the hydrogen atom releases an electron to become a proton which then acts as a catalytically active site for acid-catalyzed reactions. Migration of protons into the bulk solution is potentially feasible from a transport perspective due to the high the mobility of protons in water as compared to other cations.[7] However, there are other concerns which will be addressed.

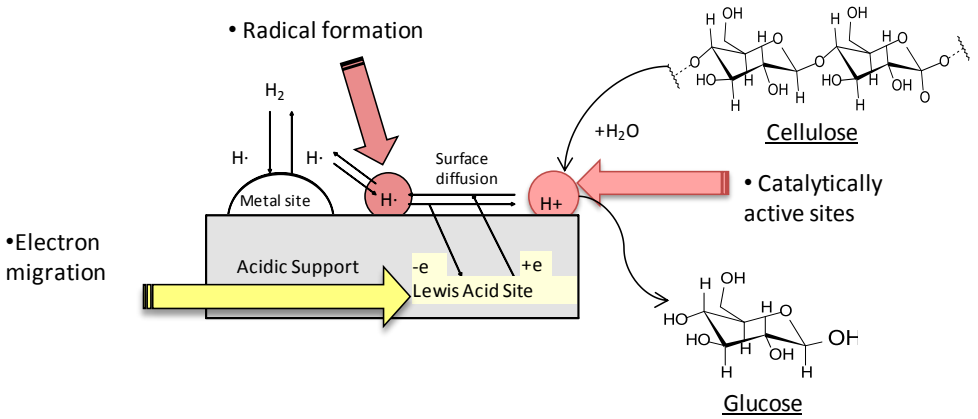

Figure 4.2: Proposed mechanism of H_2 spillover and electron migration to form protons.

The main material investigated in Hattori's study was Pt/SO_4^{-2}-ZrO_2; yet he asserts that the model applies to all metal/solid-acid catalysts where H_2 is present. Hattori's conclusions are based on a short review of hydrogen enhancing the catalytic activity for several reactions: cumene cracking with HZSM-5 and Pt/SiO_2, n-hexane isomerization over $CoMo/SiO_2$-Al_2O_3, and toluene disproportionation with zeolites. [6] However, this proposed model seems less applicable to supports that are not as easily reduced as the ZrO_2 support used in Hattori's study, i.e. alumina in the present case. This mechanism also seems questionable due to a buildup of electrostatic potential. The behavior of the materials tested by Fukuoka and Dhepe also seems to refute this proposed scheme. Similar studies of hydrogen spillover have correlated overall acidic site density to acceptor capacity of the spilt over species, implying that more acidic supports (total acid concentration) facilitate spillover and thus hydrolysis. [8] However, Fukuoka and Dhepe show that the activity of their catalysts do not correspond well with support acidity.[5] Therefore, there is some confusion regarding this reported hydrolysis mechanism while the hydrogenation of sugars by supported transition metals is well understood.

Other groups have suggested an alternative hypothesis for the hydrolysis step. Luo et. al. used ruthenium supported on activated carbon to convert cellulose to polyols.[9] They observed >85% cellulose conversion with a variety of sugar alcohol products formed. The hydrolysis step was proposed to be facilitated by protons from dissociation of water at elevated temperature. This mechanism was also suggested by Ji et. al. who used tungsten carbide as a hydrolysis and hydrogenolysis catalyst with up to 100% conversion of microcrystalline cellulose with a 61% yield to ethylene glycol and 3.9% yield of sorbitol.[10] The results presented in this chapter agree with this latter mechanism;

however, another mechanistic effect related to the catalyst stability, which in turn is related to metal precursor salt, is elucidated.

4.2 Materials and Methods

4.2.1 Catalyst Preparation

The catalysts were prepared via wet impregnation procedure which consists in dissolving the required weight of metal precursor in the final solid with an amount of water to obtain a slurry. The slurry was mechanically stirred to achieve maximum homogeneity throughout. The metal precursors were $H_2PtCl_6 \cdot 6H_2O$ (ACS reagent grade, Sigma Aldrich) and $H_2Pt(OH)_6$ (99.9% metals basis, Alfa Aesar). The γ-Al_2O_3 support (3μm APS powder, 99.97% metals basis, Alfa Aesar) was used as received. The catalysts were then calcined at 500 °C (ramp $1K \cdot min^{-1}$) in air for 4 h followed by reduction in 10% H2/He at 300 °C (ramp $5K \cdot min^{-1}$) for 3 h prior to treatments and catalytic runs. The 1 wt% Pt/γ-Al_2O_3 commercial sample was purchased from Alfa Aesar.

4.2.2 Experimental runs

For structural changes experiments, an amount of catalyst was placed in a Teflon tube with DI water and placed into a preheated oven under constant agitation. After a specific amount of time, the tubes were quenched in an ice bath then filtered and dried prior to further analysis by ^{27}Al MAS NMR spectroscopy.

For dissolution experiments, 100 mL of DI water was charged in a 316 stainless steel 300 mL batch reactor (Parr 5500 series) and purged with reaction gas then heated to the desired reaction temperature. Once the desired temperature was reached (200 °C), an

amount of catalyst in 30 mL of DI water was delivered from an external catalyst chamber by pressurized gas (~25 bar N_2). The chamber was then filled with another 20 mL of water and delivered to the reactor to insure transfer of all solids and the final pressure adjusted to about the vapor pressure of water at 200 °C (autogeneous pressure). After a specific amount of time, liquid samples were taken and filtered (0.45 μm nylon syringe filter) for ICP analysis.

For catalytic experiments, 0.5 g of the catalyst, 0.5 g of microcrystalline cellulose (Avicel, Sigma Aldrich) and 100 mL of water were placed in the reactor and purged with H_2. After heating to 200 °C, the chamber was pressurized to 60 bar with H_2 and stirring was initiated. The reactor was quenched after 4 h and a liquid sample was filtered (0.45 μm nylon syringe filter) for HPLC analysis. The mass conversion was determined by weighing all leftover solids after the reaction.

4.2.3 Solid State NMR Spectroscopy

^{27}Al MAS NMR measurements were performed on a Bruker DSC 400 spectrometer. The samples were packed into a 4 mm zirconia rotor and spun at 12 kHz. The resonance frequency for 27Al was 104.2 MHz. A $\pi/12$ pulse was used for excitation and the recycling delay was 250 msec. For each spectrum, a minimum of 2400 scans were accumulated. Solid $Al(NO_3)_3$ was used as a reference compound (δ = -0.543 ppm). In order to calculate the boehmite fraction, the normalized 27Al spectra were fitted as a linear combination between pure boehmite and pure alumina spectra.

4.2.4 X-ray Photoelectron Spectroscopy (XPS)

X-ray Photoelectron Spectroscopy (XPS) was carried out using a Thermo K-Alpha XPS system with a Monochromated Al K-alpha source giving an incident x-ray energy of

1486.7 eV. The samples were mounted in a nonmagnetic powder sample holder and evacuated to $4x10^{-8}$ mbar before analysis. The pressure during analysis was $3.2x10^{-7}$ mbar. The x-ray spot size was 400 microns, and mixed ion/electron charge compensation was used. Survey scans were taken over an energy range of 0 – 1350 eV binding energy with a pass energy of 200 eV. High resolution scans were taken for O, Al, Cl, Ni, and Pt each with a pass energy of 50 eV, a step size of 0.01 eV and a dwell time of 50 ms per step. Quantification was done by subtracting a Shirley background and correcting the resulting peak areas for analysis depth and X-ray cross-section using the TPP-2M and Scofield sensitivity factors, respectively.

4.2.5 Chromatography

Carbohydrate analysis was performed on an Agilent 1200 series HPLC equipped with an Evaporative Light Scattering detector and Prevail Carbohydrate ES column (5 μm, 250 mm x 4.6 mm, Grace Davison). Analysis was performed on 20 μL injections in isocratic mode with 75/25% v/v acetonitrile/water mobile phase at a flow rate of 1 mL/min. The column and detector were held at 40 °C and 30 °C, respectively. Standards of cellobiose, glucose, sorbitol, xylitol, erythritol and glycerol were prepared for quantitative assessment.

4.2.6 Dispersion analysis

Hydrogen chemisorptions experiments were performed on a Micromeritics AutoChem II Chemisorption Analyzer equipped with a thermal conductivity detector. The samples were first treated at 200 °C for 1 h with argon as carrier gas to eliminate adsorbed water. Then the temperature was cooled to ambient after which the sample was ramped to 300 °C (5 K/min) under 10% H_2/Ar. After reduction, the sample was brought to 40 °C and

dosed 20 times with 4% H_2/Ar followed by dosing with 10% O_2/He. A final dosing of 4% H_2/Ar was performed and used for the dispersion analysis. An H_2/Pt surface stoichiometry of 1.5 was assumed according to the proposed titration reactions.[11-12]

$$(4)\ Pt + (1/2)H_2 \rightarrow Pt\text{-}H$$

$$(5)\ Pt + (1/2)O_2 \rightarrow Pt\text{-}O$$

$$(6)\ Pt\text{-}O + (3/2)H_2 \rightarrow Pt\text{-}H + H_2O$$

4.2.7 Inductively Coupled Plasma Spectroscopy

Dissolved metals were analyzed with a Perkin Elmer Optima 7300 DV ICP Optical Emission Spectrometer. An aliquot of sample filtrate was combined with trace metal grade nitric acid and allowed to digest for 30 minutes. The samples were then diluted to 10 mL with DI water prior to analysis. Standards of Al and Pt were prepared from a commercial stock solution for quantitative assessment.

4.3 Results and Discussion

Herein, it is shown that specific metal precursors can have a dramatic effect on the performance of Pt/γ-Al_2O_3 catalysts for conversion of cellulose in aqueous phase under high pressure hydrogen. In this reaction, sugar alcohols are formed by acid catalyzed hydrolysis of cellulose followed by metal catalyzed hydrogenation of the glucose intermediate (Figure 4.1). Sugar alcohol yields of up to 31% were reported over Pt/γ-Al_2O_3, and hydrogen spillover was suggested as the primary source for Brønsted acidic protons that catalyze the hydrolysis step.[5] However, the authors did not comment on potential mass transfer limitation of bulky sugar oligomers to the catalyst surface. It was also postulated that support acidity may play a role in hydrolysis, but no correlation to

experimental data was found.[5] Therefore, the question remains what the active site for this reaction is.

Table 4.1: Catalyst characterization and reactivity results.

Catalyst	Conversion / % [a]	Sugar alcohol yield / % [b]	PZC [c]	Metal dispersion / % [d]
Pt-Com	18	3	8.8	58
γ-Al_2O_3	26	-	6.6	-
Pt-OH	31	11	6.0	76
Control	27	-	5.8[e]	-
Pt-Cl	31	21	4.8	70
Pt-Com-HCl	33	17	4.5	50

[a] Based on mass loss cellulose, [b] Carbon molar basis, [c] Measured at room temperature with loading 10,000 m^2/L, [d] Measured via H_2/O_2 titration, [e] pH of DI water used.

Cellulose conversion and sugar alcohol yield of catalysts synthesized with 1 wt% metal loading from H_2PtCl_6 (Pt-Cl) and $H_2Pt(OH)_6$ (Pt-OH) salts were compared to a commercial 1 wt% Pt/γ-Al_2O_3 (Pt-Com). The conversion for Pt-Cl and Pt-OH were comparable to the control reaction, while Pt-Com was much lower (Table 4.1). The sugar alcohol yield decreased in the order Pt-Cl > Pt-OH > Pt-Com, and the sorbitol selectivity followed the same trend (Figure C.1). No clear correlation was observed between the metal dispersion and either conversion or yield (Table 4.1).

An important consideration for reactions under the present conditions is that γ-Al_2O_3 can be hydrated and that boehmite (AlOOH) is thermodynamically favoured over γ-Al_2O_3 and gibbsite ($Al(OH)_3$) in water above 150 °C.[13] The formation of boehmite results

in loss of surface area and Lewis acid site concentration along with sintering of supported metal particles.[14]

Significant differences were observed for the rate of boehmite formation from different alumina samples (Figure 4.3). However, the rates for Pt-Cl and Pt-OH were comparable over the first 4 h, which is the duration of a catalytic run. Therefore, this cannot explain the differences in activity (Table 4.1).

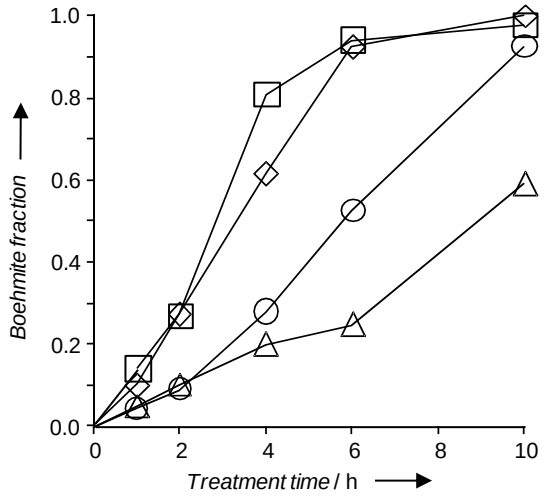

Figure 4.3: Kinetics of boehmite formation during treatment in liquid water at 200 °C: ◊ = γ-Al_2O_3, ○= Pt-OH, Δ = Pt-Cl, □ = Pt-Com.

A significant difference between these samples is that a considerable amount of dissolved aluminum was detected in solution when the Pt-Cl catalyst was treated in liquid water at 200 °C (Figure 4.4). In contrast, no dissolved aluminum was detected for bare γ-Al_2O_3, Pt-OH and Pt-Com indicating dissolution is independent of the phase transformation to boehmite. It is suggested that the dissolution is caused by the formation of water soluble AlOCl and $AlCl_3$ species during calcination of Pt-Cl.[15] The residual chlorine content of Pt-Cl was determined by XPS to be 1.9 mol% indicating that chlorine

facilitates dissolution. The effect of chlorine was further probed by treating γ-Al_2O_3 with HCl (Al-Cl) followed by calcination/reduction. This treatment resulted in enhanced dissolution compared to bare γ-Al_2O_3 (Figure 4.4). Additionally, the presence of 60 bar H_2 enhanced support dissolution (Figure C.3) and may be a consequence of hydrogen spillover modifying the oxide surface by exposing Al^{3+} acid sites.[16] The dissolution profiles also suggest that dissolved aluminum eventually precipitates, supposedly as stable boehmite.

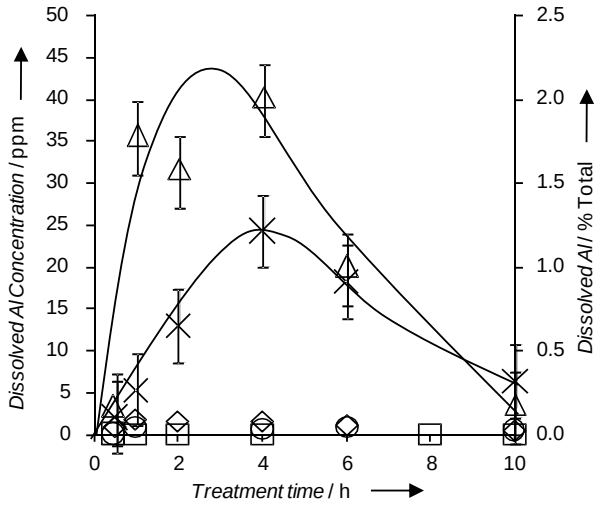

Figure 4.4: Dissolution of γ-Al_2O_3 supported catalysts in liquid water at 200 °C and autogeneous pressure: ◊ = γ-Al_2O_3, ○ = Pt-OH, Δ = Pt-Cl, □ = Pt-Com, X = Al-Cl.

The release of aluminum into solution is of particular interest with respect to hydrolysis and could explain the comparatively higher alcohol yield from Pt-Cl. The catalytic activity of Al^{3+} cations was probed by converting microcrystalline cellulose in an aqueous $Al(NO_3)_3$ solution (Figure 4.5). In the presence of 30 ppm Al^{3+}, a cellulose conversion of 42% and a glucose yield of 12% were achieved compared to 62% cellulose conversion and ca. 4% glucose yield with 360 ppm Al^{3+}. Comparison with the control

clearly demonstrates the catalytic effect of the Al^{3+} cations. It is proposed that Lewis acidic Al^{3+} interact with OH^- ions shifting the dissociation equilibrium of water. This increases the concentration of protons and, thus, the hydrolysis activity. This effect was verified by monitoring the pH of the solution. Both Al^{3+} containing solutions had lower pH compared to the control (Figure C.4). We suggest that the higher concentration of aluminium ions (i.e. lowest pH) in the experiment with 360 ppm Al^{3+} leads to the formation of glucose degradation products and lower glucose yield as observed by HPLC analysis (Figure C.5). It was previously reported that metal salts of phosphotungstic acid can hydrolyze cellulose in aqueous phase at 150 °C.[17]

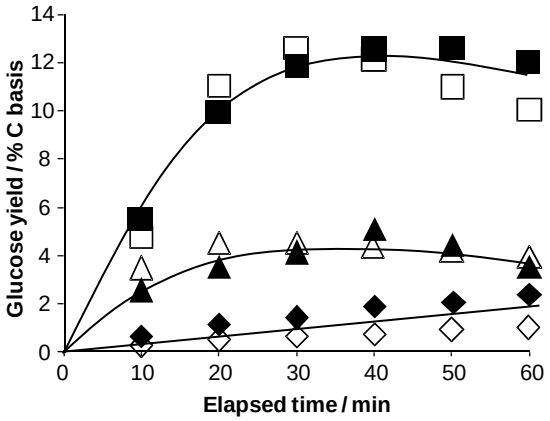

Figure 4.5: Glucose yield (initial mole $C_6H_{10}O_5$ basis) from microcrystalline cellulose (500 mg) and $Al(NO_3)_3$ salt in 100 mL H_2O at 200 °C and 60 bar H_2: ◊ = Control, Δ = 360ppm of Al^{3+}, □ = 30ppm of Al^{3+} (filled and empty symbols indicate results from separate experiments).

In addition to the acidity originating from dissolved species, solids can influence the acidity of an aqueous medium by buffering the pH at their point of zero charge (PZC). The PZC can be influenced by the structure of the oxide including defects and impurities as well as adsorbed ions.[18-19] In the present study, conversion and sugar alcohol yield increased with decreasing point of zero charge of the catalyst measured at room

temperature (Table 4.1). In particular, when Pt-Com was treated with HCl (Pt-Com-HCl) followed by calcination/reduction, the PZC decreased from 8.8 to 4.5 along with significant increases of the cellulose conversion and sugar alcohol yield. Note that the PZC had a stronger influence on the sugar alcohol yield than on the conversion. This observation suggests that cellulose is converted to soluble oligomers even in a medium with relatively low acidity. In contrast, more acidic conditions appear to be necessary for complete hydrolysis to glucose, which must be formed as an intermediate for the formation of sugar alcohols. We attribute the low PZC of Pt-Cl and Pt-Com-HCl to ion exchange of chloride with the most basic surface hydroxyl groups.[20] Additionally, surface bound chlorine can interrupt the hydrogen bonding network of surface hydroxyl groups and thereby increase the lability of the OH bonds resulting in enhanced Brønsted acidity.[21] We observed no effect on the measured PZC of Pt-Cl after washing with 500 mL water.

4.4 Conclusions

These results highlight the influence of metal precursors on the performance of catalysts for aqueous phase conversion of cellulose to sugar alcohols. The precursor choice influences catalyst dissolution and the PZC of the support, both of which shift the dissociation equilibrium of water to increase the solution acidity rendering higher activity for hydrolysis. These phenomena must be considered in aqueous phase reforming reactions to avoid erroneous conclusions with regard to reaction mechanisms.

4.5 References

[1] Dolev, A.; Gelman, V.; Shter, G. E.; Grader, G. S. *Catalysis Letters* **2003**, *89*, 169-178.

[2] Reyes, P.; Oportus, M.; Pecchi, G.; Frety, R.; Moraweck, B. *Catalysis Letters* **1996**, *37*, 193-197.

[3] Guillaume, D.; Gautier, S.; Despujol, I.; Alario, F.; Beccat, P. *Catalysis Letters* **1997**, *43*, 213-218.

[4] Beard, B. C.; Zhang, Z. C. *Catalysis Letters* **2002**, *82*, 1-5.

[5] Fukuoka, A.; Dhepe, P. L. *Angewandte Chemie - International Edition* **2006**, *45*, 5161-5163.

[6] Hattori, H.; Shishido, T. *Catalysis Surveys from Japan* **1997**, *1*, 205-213.

[7] Han, J.; Zhou, X.; Liu, H. *Journal of Power Sources* **2006**, *161*, 1420-1427.

[8] Benseradj, F.; Sadi, F.; Chater, M. *Applied Catalysis A: General* **2002**, *228*, 135-144.

[9] Luo, C.; Wang, S.; Liu, H. *Angewandte Chemie International Edition* **2007**, *46*, 7636-7639.

[10] Na Ji, T. Z., Mingyuan Zheng, Aiqin Wang, Hui Wang, Xiaodong Wang, Jingguang G. Chen, *Angewandte Chemie International Edition* **2008**, *47*, 8510-8513.

[11] Benson, J. E.; Boudart, M. *Journal of Catalysis* **1965**, *4*, 704-710.

[12] Delannay, F., Ed. *Characterization of Heterogeneous Catalysts*; Marcel Dekker: New York, **1984**; Vol. 15.

[13] MacDonald, D. D.; Butler, P. *Corrosion Science* **1973**, *13*, 259-274.

[14] Ravenelle, R. M.; Copeland, J. R.; Kim, W. G.; Crittenden, J. C.; Sievers, C. *ACS Catalysis* **2011**, *1*, 552-561.

[15] Réti, F.; Bertóti, I.; Mink, G.; Székely, T. *Reactivity of Solids* **1987**, *3*, 329-336.

[16] Maret, D.; Pajonk, G. M.; Teichner, S. J. Spillover of Adsorbed Species. In *Studies in Surface Science and Catalysis*; Pajonk, G. M., Teichner, S. J., Germain, J. E., Eds.; Elsevier: Amsterdam, **1983**; Vol. 17; pp 215-231.

[17] Shimizu, K.; Furukawa, H.; Kobayashi, N.; Itaya, Y.; Satsuma, A. *Green Chemistry* **2009**, *11*, 1627-1632.

[18] Trueba, M.; Trasatti, S. P. *European Journal of Inorganic Chemistry* **2005**, *2005*, 3393-3403.

[19] Korah, J.; Spieker, W. A.; Regalbuto, J. R. *Catalysis Letters* **2003**, *85*, 123-127.

[20] Vordonis, L.; Koutsoukos, P. G.; Lycourghiotis, A. *Journal of Catalysis* **1986**, *101*, 186-194.

[21] Digne, M.; Raybaud, P.; Sautet, P.; Guillaume, D.; Toulhoat, H. *Journal of the American Chemical Society* **2008**, *130*, 11030-11039.

CHAPTER 5

SURFACE SILYLATION OF γ-AL_2O_3 SUPPORTED CATALYSTS FOR IMPROVED HYDROTHERMAL STABILITY

5.1 Background

5.1.1 Methods to Increase Alumina Stability

The results discussed in Chapters 3 & 4 illustrate that the transformation of alumina supported catalysts to hydroxide phases in water at 200 °C occurs within hours, and it has been demonstrated that γ-Al_2O_3 completely transforms to boehmite (AlOOH) in water at 200 °C after about six hours. The transformation to boehmite results in loss in Lewis acid site concentration and surface area as well as sintering of metal particles. Additionally, the alumina support can dissolve which can have potential catalytic activity. Therefore, it is clear that γ-Al_2O_3 must be stabilized before it can be used as a support for catalytic processes in hot liquid water, such as aqueous phase reforming.

Alumina is commonly used as a membrane material, and some methods of stabilizing alumina membranes against hot liquid water have been explored. These include doping with Ga^{3+} and La^{3+} as well as CeO_2 and ZrO_2.[1-2] Dip-coating of alumina supported catalysts in polytetrafluoroethylene fibers has been shown effective in slowing the formation of bohemite.[3] The stabilization effect was attributed to increased hydrophobicity. Silylation of alumina based catalysts has been used to increase stability in gas phase upgrading such as Fischer-Tropsch.[4-6] However, liquid phase stability studies of supported alumina catalysts are not as common.

5.1.2 Silicon Deposition

In Chapter 2, it was found that hydrothermal stability of zeolites in water is dependent on the concentration of resilient Si-O-Al bonds. Chapter 3 illustrates that capping specific surface hydroxyl groups of basic nature with metal particles results in hindered boehmite transformation. With these findings in mind, it is hypothesized that addition of silicon species to alumina surface (i.e. formation of Si-O-Al) and the deposition of this silicon on basic hydroxyl sites will result in increased hydrothermal stability in hot water.

One method of silicon deposition onto alumina is by chemical vapor deposition (CVD). This method consists of contacting the alumina powder with a silicon vapor generated from a precursor such as tetramethoxysilane (TMOS) or tetraethoxysilane (TEOS).[7-8] Another method is chemical liquid deposition (CLD) where silicon is deposited on the support in a solvent containing silicon precursor. The CLD procedure has been applied to a variety of supports with different precursors. Liquid deposition of TEOS has been used to coat Fe_2O_3 particles with silicon layers,[9] and this precursor has also been applied to alumina.[10] The CLD on zeolites with TEOS and polydimethylsiloxane (PDMS) have also been explored.[11-13] These precursors interact with surface hydroxyl groups, and subsequent calcination leaves silicon species bound on the surface (Figure 5.1).

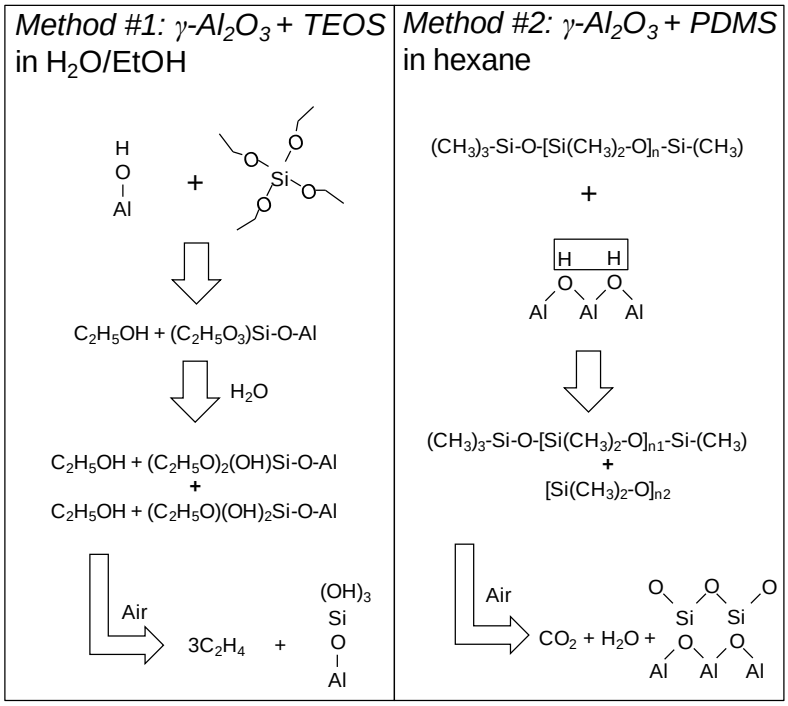

Figure 5.1: Si deposition on alumina surface with TEOS and PDMS precursors.

In this chapter, it is demonstrated that CLD of silicon is a viable method to increase the hydrothermal stability of 1 wt% Pt/γ-Al_2O_3 in hot liquid water. The presence of surface silicon species drastically slows the formation of boehmite. It is also shown that supported metal particles also have increased stability as a result of silylation. In addition to investigating the stability, the catalyst activity for production of H_2 from 5 wt% sorbitol is examined. It is important to note that methods applied to alumina supports may be applicable to other support materials.

5.2 Materials and Methods

5.2.1 Catalyst Preparation

The Pt/γ-Al_2O_3 catalysts were prepared via wet impregnation to achieve 1 wt% metal and the slurry was mechanically stirred to achieve maximum homogeneity over 24 h. The

metal precursor was $H_2PtOH_6 \cdot 6H_2O$ and the support was γ-Al_2O_3 (3μm APS powder, 99.97% metals basis, Alfa Aesar). The catalysts were dried in a vacuum oven, then calcined in air at 500 °C (ramp $1K \cdot min^{-1}$) for 4 h followed by reduction in 10% H_2/He at 300 °C (ramp $5K \cdot min^{-1}$) for 3 h prior to silylation treatments.

Catalysts were silylated according to two different methods available in the literature. The first method consisted of silylation with tetraethyl orthosilicate (TEOS, 98% Alfa Aesar) in a solution of ethanol and distilled water for 4 h at 40 °C.[10] The second silylation procedure was performed in a solution of hexane and poly-dimethylsiloxane (PDMS, MW 2000, Alfa Aesar) for 12 h at room temperature.[13] The quantity of precursor added corresponded to the amount of silicon necessary to achieve loadings of 10%, 20% and 40% silicon by weight, and actual loadings were measured by ICP-AES. Following all silylation treatments, the samples were calcined and reduced according to the same procedure described above.

5.2.2 ICP/AES

ICP analysis was performed with a Spectro Ciros Vision, Radial Viewing (SOP) instrument. Aluminum adsorption wavelengths utilized were 167.078, 396.152 and 394.401 nm. The concentration of aluminum was determined based on the average of the absorbances at the three wavelengths. Silicon concentration was determined by the average absorbance at wavelengths 251.612 and 288.158 nm.

Prior to analysis, approximately 0.1 gram of material was fused with 1 gram of sodium tetraborate (decahydrate) and 3 grams of sodium carbonate, anhydrous in a platinum crucible. The cooled fusion was digested using 20 mL of concentrated HCl. An aliquot of the digestion solution was diluted to a volume of 500 mL and analyzed for silicon and

another aliquot (approximately 0.5g diluted to 10g) was analyzed for aluminum. Blanks and standards were made with the same proportion of HCl, sodium tetraborate, and sodium carbonate as the samples. Subsequent dilutions for the aluminum analysis were done with the reagent blank solution.

5.2.3 X-ray Diffraction

Powder X-ray diffraction (XRD) patterns were measured on a Philips X'pert diffractometer equipped with an X'celerator module using Cu Kα radiation. Diffractograms were obtained from $2\theta = 5°$ to 70° with a step size of 0.0167°.

5.2.4 MAS NMR Spectroscopy

All MAS NMR measurements were performed on a Bruker DSC 400 spectrometer. The samples were packed into 4 mm zirconia rotors. For ^{27}Al MAS NMR the spinning rate was 12 kHz, and the resonance frequency for ^{27}Al was 104.2 MHz. A $\pi/12$ pulse was used for excitation and the recycling delay was 250 msec. For each spectrum, a minimum of 2400 scans were accumulated. Solid $Al(NO_3)_3$ was used as a reference compound (δ = -0.543 ppm). To calculate the boehmite fraction, the normalized ^{27}Al spectra were fitted as a linear combination of the spectra of pure boehmite and pure alumina according to previous methods.[14] ^{29}Si MAS NMR direct polarization measurements were performed with spinning rate of 10 kHz and resonance frequency for ^{29}Si at 79.4 MHz. For each spectrum, a minimum of 6000 scans were accumulated. Solid 4,4-dimethyl-4-silapentane-1-sulfonic acid (DSS) was used as a reference compound (δ = 0 ppm). ^{1}H MAS NMR measurements were performed with adamantane as a reference compound (δ = 1.756 ppm). Prior to analysis, the samples were dried under vacuum at 200 °C overnight and

packed into 4 mm zirconia rotors in a dry box. Samples were spun at 12 kHz for a total number of 64 scans. The obtained spectra were normalized by the sample mass. Difference spectra were obtained by subtracting the spectrum of mass normalized Pt/γ-Al_2O_3 from the normalized spectra of silyated samples.

5.2.5 IR Spectroscopy

IR spectra were collected on a Nicolet 8700 FT-IR spectrometer with a MCTA detector and 128 scans at 4 wavenumber resolution. Each catalyst was pressed into a self supported wafer and loaded into a stainless steel vacuum chamber with Teflon sealed ZnSe windows. The sample was activated at 500 °C for 1 h at ca. 10^{-6} bar to remove water. The temperature was then decreased to 150 °C to record spectra. After measuring these spectra, the sample was dosed with 0.1 mbar of pyridine vapor. The sample was then evacuated for 30 minutes, and the relevant peaks were integrated to give total acid site concentration using the molar extinction coefficients reported by Datka.[15] The wafer densities were obtained by weighing a circular section of the wafer (¼" in diameter) after the experiment. The mass of this section was used to normalize the spectra. Difference spectra were obtained by subtracting the spectrum of mass normalized Pt/γ-Al_2O_3 from the normalized spectra of silyated samples.

5.2.6 Nitrogen Physisorption

Physisorption measurements were performed on a Quantachrome Quadrasorb SI surface area and pore volume analyzer at the temperature of liquid nitrogen (-203 °C). Prior to analysis, samples were degassed at 200 °C for two hours under vacuum. The surface area was calculated utilizing the multi-point BET method from the adsorption isotherm in the relative pressure range ($0.05 \leq P/P_0 \leq 0.3$).

5.2.7 H_2/O_2 Titration

Hydrogen chemisorption experiments were performed on a Micromeritics AutoChem II Chemisorption Analyzer equipped with a thermal conductivity detector. The samples were first treated at 200 °C for 1 h with argon as carrier gas to eliminate adsorbed water. Then the temperature was cooled to ambient after which the sample was ramped to 300 °C (5 K/min) under 10% H_2/Ar. After reduction, the sample was brought to 40 °C and dosed 20 times with 4% H_2/Ar followed by dosing with 10% O_2/He. A final dosing of 4% H_2/Ar was performed and used for the dispersion analysis. An H_2/Pt surface stoichiometry of 1.5 was assumed according to the proposed titration reactions.[16-17]

$$(7)\ Pt + (1/2)H_2 \rightarrow Pt\text{-}H$$

$$(8)\ Pt + (1/2)O_2 \rightarrow Pt\text{-}O$$

$$(9)\ Pt\text{-}O + (3/2)H_2 \rightarrow Pt\text{-}H + H_2O$$

5.2.8 STEM

STEM images were acquired with an aberration corrected Nion UltraSTEM scanning transmission electron microscope using a high-angle annular dark field detector. This mode gives a Z-contrast image, where the intensity is roughly proportional to the square of the atomic number and the thickness. Samples were dried at 100 °C in vacuum to remove contamination.

5.2.9 Catalyst Stability and Activity

In order to investigate hydrothermal stability, catalyst treatments were performed similar to methods found elsewhere.[18] Briefly, 0.5 g of the solid was suspended in 30 ml of deionized water. Each mixture was poured in an autoclave with a Teflon liner, which was placed in a preheated oven at 200 °C under constant agitation. After a specific

amount of time, the reaction was quenched by placing the autoclave in an ice bath. The mixture was filtered (0.45 μm Nylon filter), and the solids were allowed to dry at room temperature in air for at least 24 h prior to characterization.

To test for catalytic activity for aqueous phase reforming, 0.1 g of catalyst was placed in 100 mL of 5 wt% sorbitol in a batch reactor and pressurized to 5 bar with nitrogen. The contents were then heated to 225 °C at which time stirring was initiated. After 4 h, the reactor was quenched in a water bath and gas samples withdrawn from a septum port and analyzed via gas chromatography.

5.3 Results

5.3.1 ICP/AES

The actual amount of silicon deposited by the silylation procedures was significantly less than the amount added during the silylation procedures (Figure 5.2). The TEOS precursor was more effective in attaching silicon to the catalyst surface compared to the PDMS precursor. The maximum amount of silicon deposited by TEOS was 3.00% by mass compared to 0.98% with PDMS. Samples are herein referred to by the silylation method and measured percent Si loading according to the following example: PtAl-TEOS-1.37 is 1 wt% Pt/γ-Al_2O_3 silylated with TEOS/ethanol/water at a loading of 1.37% silicon by mass. Similarly, catalysts silylated with PDMS/hexane are denoted as PtAl-PDMS-xx.

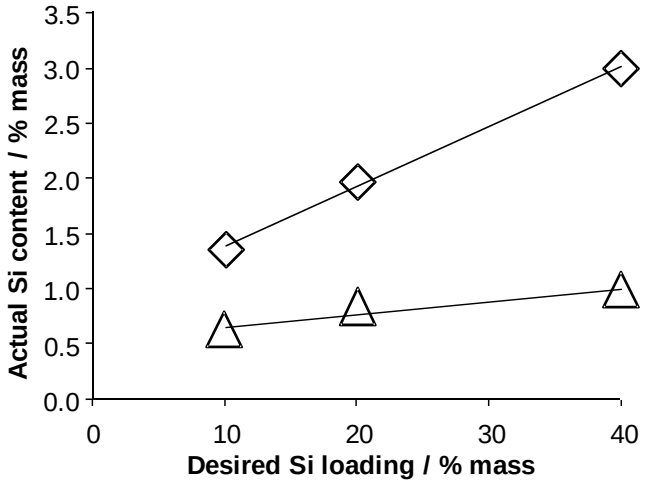

Figure 5.2: Actual silicon content as determined by ICP/AES analysis compared to the amount of silicon added during liquid deposition.

5.3.2 XRD

Untreated Pt/γ-Al_2O_3 shows the characteristic diffraction pattern of the defective spinel structure of the alumina support with the two main peaks located at 2θ = 45.8° and 67° corresponding to the (400) and (440) crystal planes, respectively (Figure 5.3).[19] There were no reflections corresponding to metallic platinum indicating that the platinum particles are well dispersed. After 10 h of treatment in water at 200 °C, the alumina support is converted to a crystalline material consistent with previous investigations.[14] The crystal phase is identified as boehmite through comparison to a standard reference diffractogram with the main peaks located at 2θ = 14.5°, 28.2°, 38.3°, 49° and 49.3° corresponding to the (020), (120), (140, 031), (051) and (200) crystal planes, respectively (Figure 5.3b).[19-20]

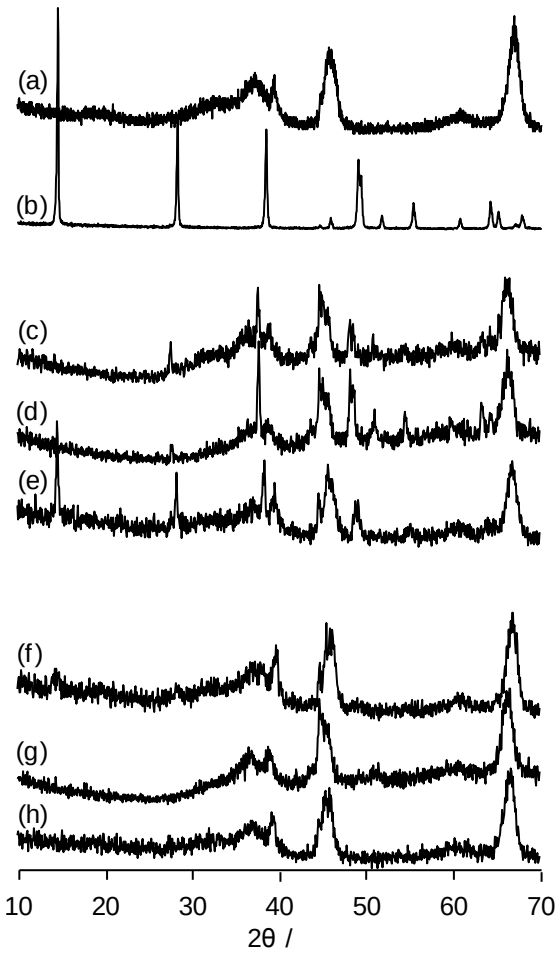

Figure 5.3: X-ray diffractograms of Pt/γ-Al_2O_3 (a) and Pt/γ-Al_2O_3 treated for 10 h at 200 °C (b), and silylated catalysts following 10 h treatment at 200 °C in water: Pt-Al-PDMS-0.61 (c), Pt-Al-PDMS-0.82 (d), Pt-Al-PDMS-0.98 (e), PtAl-TEOS-1.37 (f), PtAl-TEOS-1.97 (g), PtAl-TEOS-3.00 (h).

The x-ray diffractograms of the silylated catalysts did not exhibit any evidence of structural changes during the silylation procedure, nor did silica phase give rise to peaks (Figure D.1). After 10 h of hot water treatment, the samples modified by PDMS showed evidence of boemite formation although the extent of crystallization appeared to be less than that of Pt/γ-Al_2O_3 after the same treatment (Figure 5.3c-e). The PtAl-TEOS-1.37 catalyst treated for 10 h showed small peaks at 2θ = 14.5° and 28.2° attributable to boehmite while the higher weight loadings showed no evidence of boehmite formation.

5.3.3 ^{27}Al NMR

The ^{27}Al MAS NMR spectrum of Pt/γ-Al_2O_3 contains resonances at 8 ppm and 70 ppm, which are attributed to octahedrally and tetrahedrally coordinated aluminum species, respectively (Figure 5.4a).[21-22]

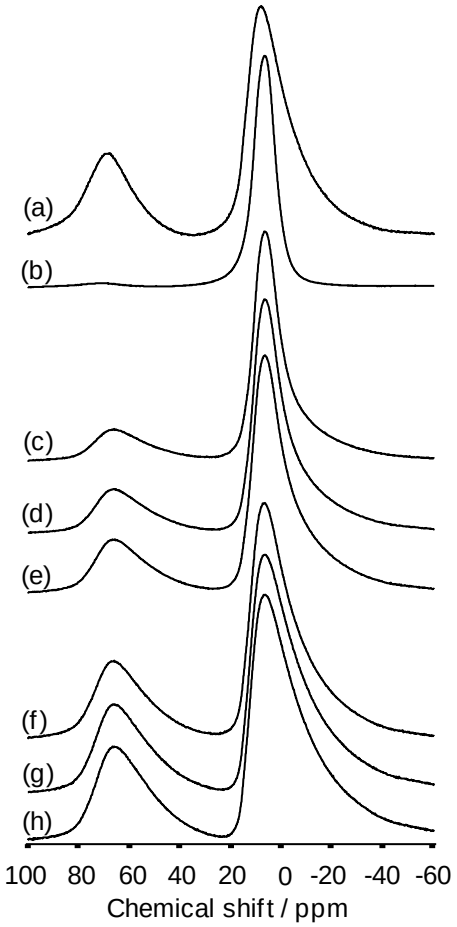

Figure 5.4: ^{27}Al NMR spectra of Pt/γ-Al_2O_3 (a) and Pt/γ-Al_2O_3 treated for 10 h at 200 °C (b), and silylated catalysts following 10 h treatment at 200 °C in water: Pt-Al-PDMS-0.61 (c), Pt-Al-PDMS-0.82 (d), Pt-Al-PDMS-0.98 (e), PtAl-TEOS-1.37 (f), PtAl-TEOS-1.97 (g), PtAl-TEOS-3.00 (h).

After 10 h of treatment in liquid water at 200 °C, the spectrum of Pt/γ-Al_2O_3 exhibits only a single sharp resonance at 8 ppm indicating that the γ-Al_2O_3 support was quantitatively converted to boehmite, as this material only contains octahedrally coordinated aluminum. The changes in the spectra of silylated Pt/γ-Al_2O_3 samples treated under the same conditions were less drastic. By fitting the spectra as a linear combination of the spectra of γ-Al_2O_3 and boehmite, the fraction of boehmite in the samples after the hot water treatment was determined, and the boehmite conversion was compared to the amount of silicon in the sample (Figure 5.5).[14]

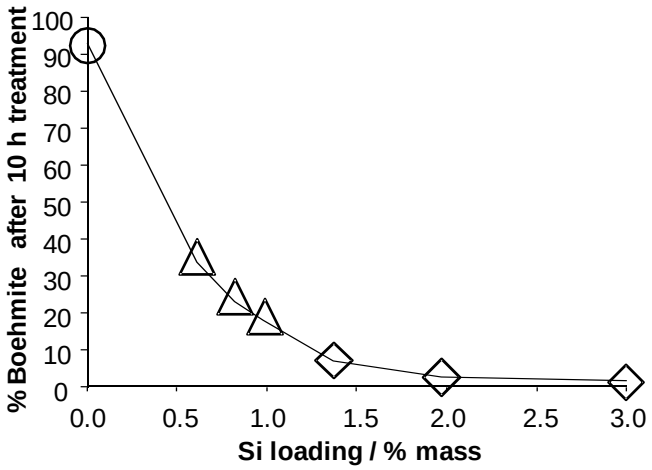

Figure 5.5: Calculated boehmite fraction after 10 h treatment in liquid water at 200 °C as a function of silicon loading: Pt/Al_2O_3 catalyst (○) and catalysts derived from PDMS (Δ) and TEOS (◊) precursor.

The samples prepared from PDMS precursor exhibit higher conversion to boehmite than the respective materials derived from TEOS precursor. Note that the conversion of all silylated samples was significantly lower than that of the original Pt/γ-Al_2O_3. In

general, the concentration of boehmite formation decreased with increasing silicon content.

5.3.4 ^{29}Si NMR

The ^{29}Si NMR spectra of both PtAl-PDMS-0.82 and PtAl-TEOS-1.97 exhibit a broad peak centered at around -100 ppm (Figure 5.6).

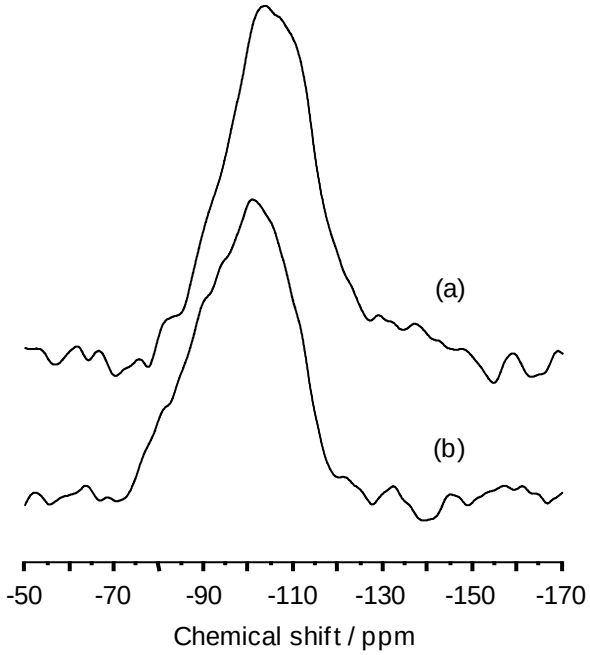

Figure 5.6: ^{29}Si NMR spectra of PtAl-TEOS-1.97 (a) and PtAl-PDMS-0.82 (b).

This signal is assigned to surface silicon attached to three silicate tetrahedra and a hydroxyl group (HO-Si-$(OSi_T)_3$).[7,23] A large neighboring peak centered around -110 ppm was observed for PtAl-TEOS-20 which is assigned to silicon coordinated to 4 silicate tetrahedra. It should be noted that an increasing degree of condensation of silicate tetrahedral leads to high field shifts while substitution of Si ions with Al ions results in low field shifts (Table 5.1).[7] The spectrum of PtAl-PDMS-0.82 contained a broad

shoulder in the range of 80-100 ppm indicating less Si with surrounding Si neighbors and more coordination of silicon to aluminum.

Table 5.1: ^{29}Si chemical shifts and attributed silicon species.

Chemical Shift / ppm	Attributable Species
-75	Si-(Al,3H)
-80	Si-(Si,3H), Si-(2Al,2H)
-85	Si-(Si,Al,2H), Si-(3Al,H)
-90	Si-(2Si,2H), Si-(2Al,Si,H), Si-(4Al)
-95	Si-(Al,2Si,H), Si-(3Al,Si)
-100	Si-(3Si,H), Si-(2Al,2Si)
-105	Si-(Al,3Si)
-110	Si-(4Si)

5.3.5 ^{1}H MAS NMR Spectroscopy

The ^{1}H NMR spectra of γ-Al_2O_3 has 6 peaks located at 5.8 ppm, 4.0 ppm, 2.4 ppm, 1.5 ppm, 0.7 ppm, -0.1 and -0.4 ppm (Figure 5.7).

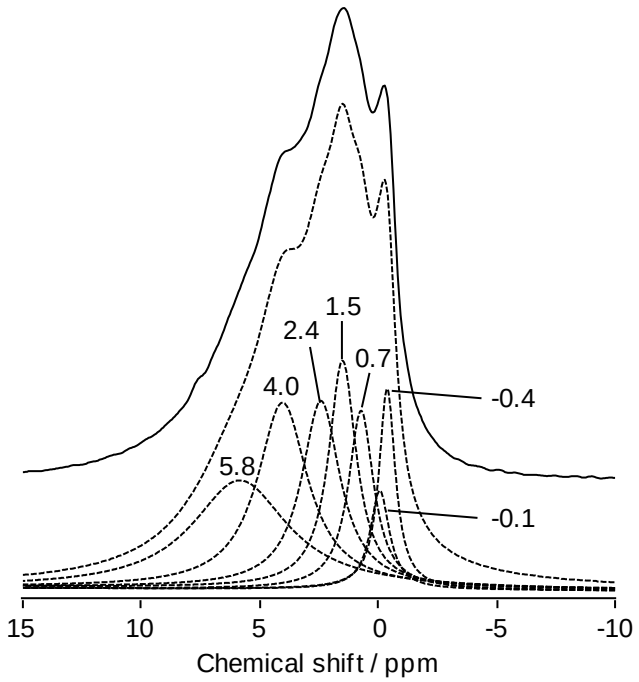

Figure 5.7: Normalized ^{1}H NMR spectra of untreated γ-Al_2O_3 (solid line) and peak deconvolution (dashed lines).

The peaks at 5.8 and 4.0 ppm are attributed to adsorbed water.[24] The high field signals at -0.4 and -0.1 ppm correspond to hydroxyl groups attached to a single Al atom, whereas the resonances at 0.7 and 1.5 ppm are attributed to Al-OH-Al species and the peak at 2.4 ppm is assigned to an OH coordinated to three Al atoms.[24] Comparing the total integral of hydroxyl group resonances to that of an adamantane reference, the concentration of hydroxyl groups was found to be 0.89 $mmol \cdot g^{-1}$ or 5.9 $OH \cdot nm^{-2}$, which is slightly lower than other investigations of dehydrated alumina (8.5 $OH \cdot nm^{-2}$).[25]

In order to investigate changes to surface hydroxyl concentration upon silicon loading, the ^{1}H NMR spectrum of the parent Pt/γ-Al_2O_3 catalysts was subtracted from the normalized spectra of the silylated catalysts (Figure 5.8). The spectra of all the silylated samples exhibited a sharp peak at 1.6 ppm, which is attributed to silanol groups.[26] The

intensity of this peak increased with increasing silicon loading from TEOS (Figure 5.8a), though the 0.82% Si sample from PDMS had higher peak intensity than the other samples. All of the difference spectra also contained a large negative peak centered at 0.7 ppm indicating losses in the most basic singly coordinated OH groups (-0.1 and -0.4 ppm) and double coordinated OH (0.7 ppm) groups compared to Pt/γ-Al_2O_3, suggesting these as the primary silicon bonding sites. A shoulder at 2.9 ppm was observed for the intermediate and highest weight loadings for both precursors. This feature is attributed to hydroxyl groups in close proximity to aluminum atoms as opposed to the silanol groups distant from aluminum.[27]

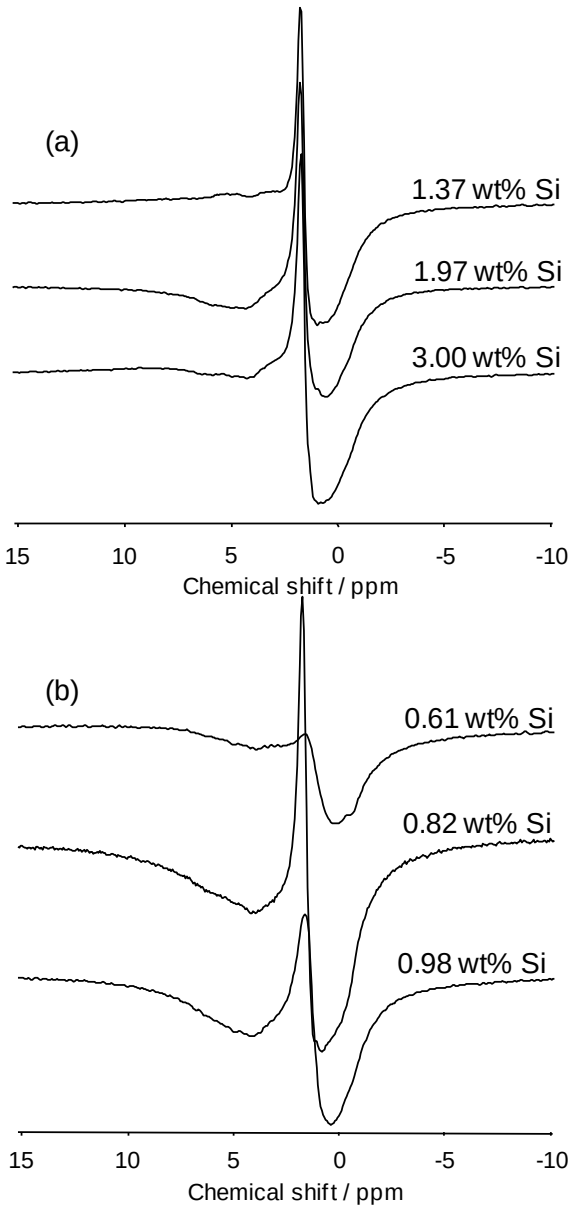

Figure 5.8: ^{1}H NMR difference spectra obtained by subtracting the spectrum of mass normalized Pt/γ-Al_2O_3 from mass normalized PtAl-TEOS (a) and PtAl-PDMS (b) catalysts with different weight loadings of Si.

For the PtAl-PDMS catalysts, the 10 wt% material showed a small silanol peak at 1.6 ppm while the sample contaning 20 wt% Si had the largest silanol concentration of all samples (Figure 5.8b). Similar to the catalysts silylated with TEOS, significant losses in the basic hydroxyl groups was observed. The losses in intensity of the peaks

corresponding to adsorbed water (~4 ppm) were more significant in the spectra of the PDMS treated samples which suggests that these samples are more hydrophobic compared those prepared from TEOS.

5.3.5 IR Spectroscopy

The IR spectra of 1wt% Pt/γ-Al_2O_3 showed 4 peaks located at 3765, 3725, 3677, and 3576 cm^{-1} (Figure 5.9a).

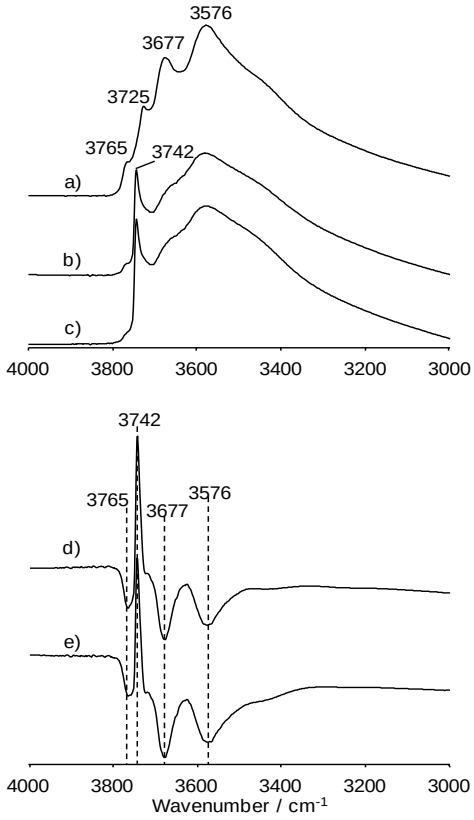

Figure 5.9: Normalized IR spectra of 1wt% Pt/γ-Al_2O_3 (a), PtAl-PDMS-0.82 (b), PtAl-TEOS-1.97 (c), and difference spectra obtained by subtracting the spectrum of mass normalized Pt/γ-Al_2O_3 from mass normalized spectra of both PtAl-PDMS-0.82 (d) and PtAl-TEOS-1.97 (e).

The peak at 3765 cm^{-1} is assigned to single coordinated OH groups, while the peak at 3725 cm^{-1} corresponds to double coordinated OH groups.[28-29] The band located at 3677 cm^{-1} corresponds to triple coordinated species. The broad peak at 3576 cm^{-1} is due to hydrogen bonded OH groups and possibly overlaps with the peak corresponding to triple coordinated species.[28] A comparison of the density normalized IR spectra shows that the spectra of the silylated samples exhibit a sharp peak at 3742 cm^{-1} indicative of silanol groups,[30] and this band is attributed to isolated silanols.[31] The difference spectra illustrate a decrease in OH species at 3765, 3677 and 3576 cm^{-1} relative to the non silylated 1wt% $Pt/\gamma\text{-}Al_2O_3$ catalyst suggesting interactions between the silica layer and hydroxyl groups on the alumina surface.

Pyridine adsorption followed by IR spectroscopy indicated that only Lewis acid sites (LAS) were present in the $Pt/\gamma\text{-}Al_2O_3$ catalyst (Table 5.2). However, upon addition of silicon using TEOS, Brønsted acidic sites (BAS) were formed. This is concluded from the observation of a peak located at ca. 1540 cm^{-1}, which is assigned to the ring vibrations of the pyridinium ion (Figure D.2). For the samples prepared with the PDMS precursor, BAS were observed once the silicon loading reached 0.82 wt%. Despite the appearance of BAS, the total acid site concentration of the silylated samples was significantly lower than that of $Pt/\gamma\text{-}Al_2O_3$.

Table 5.2: Acid site concentration as measured by adsorption of pyridine followed by IR spectroscopy.

Catalyst	Acid Site Concentrations		
	C_{Total} / mmole·g^{-1}	Brønsted / mmole·g^{-1}	Lewis / mmole·g^{-1}
Pt/ γ-Al_2O_3	1.0 x 10^{-1}	0	1.0 x 10^{-1}
PtAl-TEOS-1.37	4.2 x 10^{-2}	2.0 x 10^{-2}	2.2 x 10^{-2}
PtAl-TEOS-1.97	2.6 x 10^{-2}	5.0 x 10^{-3}	2.1 x 10^{-2}
PtAl-TEOS-3.00	8.5 x 10^{-2}	3.4 x 10^{-2}	5.1 x 10^{-2}
PtAl-PDMS-0.61	2.5 x 10^{-2}	0	2.5 x 10^{-2}
PtAl-PDMS-0.82	1.8 x 10^{-2}	7.2 x 10^{-3}	1.1 x 10^{-2}
PtAl-PDMS-0.98	3.0 x 10^{-2}	6.0 x 10^{-3}	2.4 x 10^{-2}

5.3.6 Nitrogen physisorption

The initial Pt/γ-Al_2O_3 catalyst had a BET surface area of ca. 70 $m^2 \cdot g^{-1}$ (Figure 5.10). The BET surface area remained essentially unchanged for the 0.61% and 0.82% Si PtAl-PDMS catalysts while a slight increase was observed for the sample containing 0.98% Si. In the case of the samples that were modified using TEOS, there was a slight increase in surface area to 80 $m^2 \cdot g^{-1}$ for the sample with 1.37% silicon and ~85 $m^2 \cdot g^{-1}$ for the samples with 1.97% and 3.00% Si.

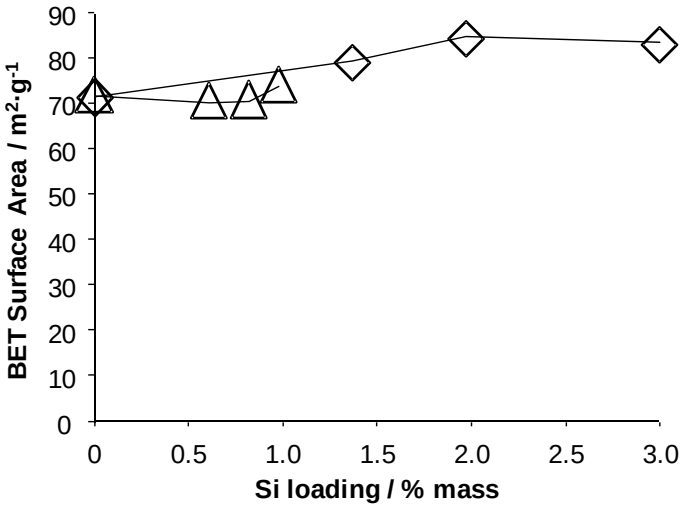

Figure 5.10: Surface area as measured by N_2 physisorption as a function of silicon loading for PtAl-PDMS (Δ) and PtAl-TEOS (◊).

5.3.7 H_2/O_2 Titration

The active or accessible metal surface area of the silylated platinum catalysts was measured by pulsed chemisorption of hydrogen (Figure 5.11). A 54 % decrease in active metal surface area was observed for the lowest Si loading with TEOS compared to a 43% decrease with the lowest Si loading from PDMS. Further silicon loading with TEOS showed little change in metal surface area while subsequent loading with PDMS resulted in a 60% loss for the highest loading of 0.98% Si.

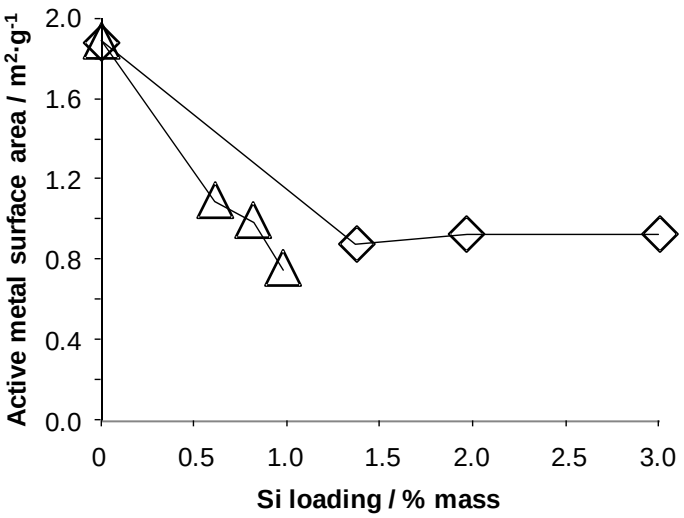

Figure 5.11: Active platinum surface area as measured by H_2/O_2 titration as a function of silicon loading for PtAl-PDMS (Δ) and PtAl-TEOS (◊).

The fraction of accessible metal of Pt/γ-Al_2O_3, PtAl-PDMS-0.82 and PtAl-TEOS-1.97 before and after 10 h of treatment in liquid water at 200 °C are also compared (Table 5.3). The treatment reduced the accessible platinum surface area, but both silicon containing materials had accessible Pt surface areas that were approximately twice that of Pt/γ-Al_2O_3 catalyst after 10 h in liquid water at 200 °C.

Table 5.3: Summary of metal particle characteristics for synthesized catalysts and after treatment for 10 h at 200 °C and saturation pressure in liquid water.

Catalyst	Dispersion / %	Metallic surface area / $m^2 \cdot g^{-1}$	Active particle diameter / nm
Pt/γ-Al_2O_3	76	1.88	1.5
Pt/γ-Al_2O_3, 10 h	10	0.23	11.9
PtAl-PDMS-0.82	48	0.98	2.4
PtAl-PDMS-0.82, 10 h	27	0.55	4.3
PtAl-TEOS-1.97	45	0.93	2.5
PtAl-TEOS-1.97, 10 h	27	0.55	4.2

5.3.8 Electron Microscopy

High resolution scanning transmission electron microscopy revealed that the majority of platinum particles of the parent Pt/γ-Al_2O_3 were in the size range of 0.5 – 1.0 nm with an average size of 1.1 nm (Figures 5.12, 5.13a). After treatment at 200 °C in water for 10 h, the size distribution shifted to larger particles with the average size increasing to 1.5 nm, and some particles were observed that were larger than 2.5 nm.

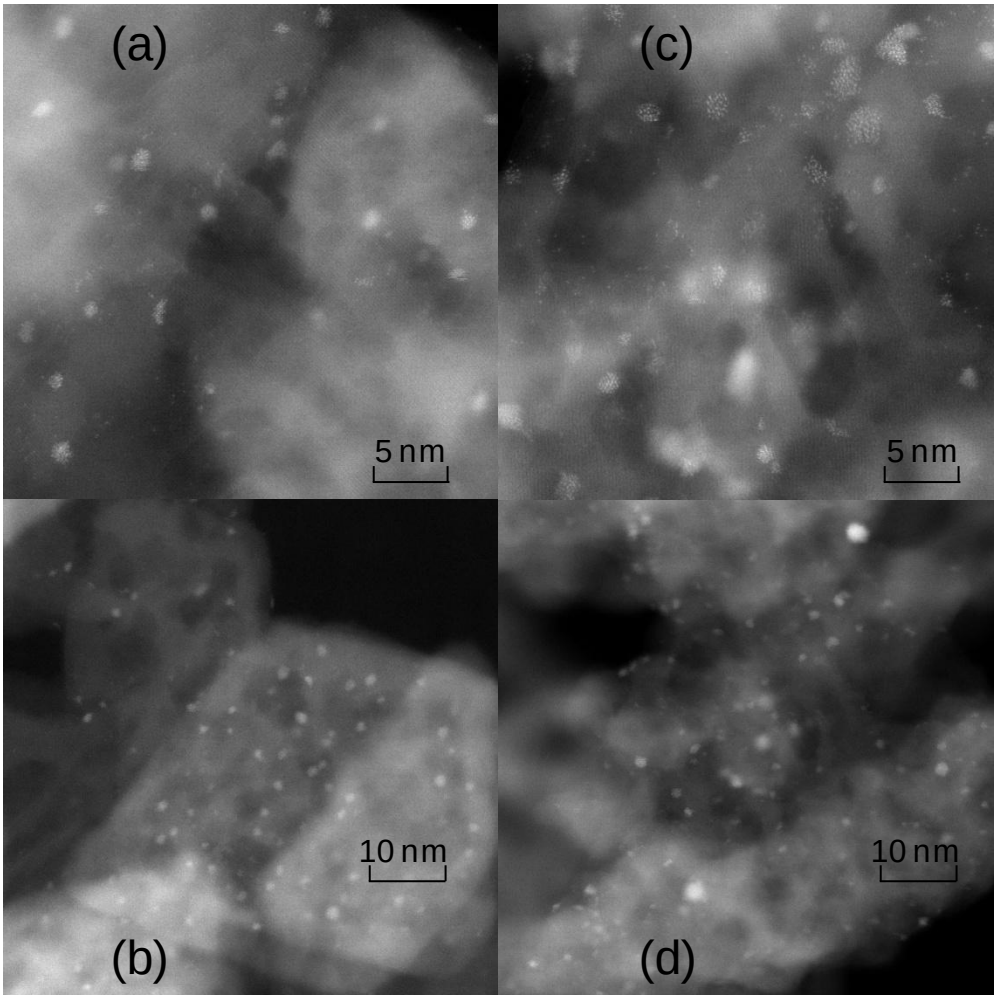

Figure 5.12: HADF TEM micrographs of Pt/γ-Al_2O_3 (a) and (b), and Pt/γ-Al_2O_3 treated for 10 h in liquid water at 200 °C (c) and (d) at different magnifications.

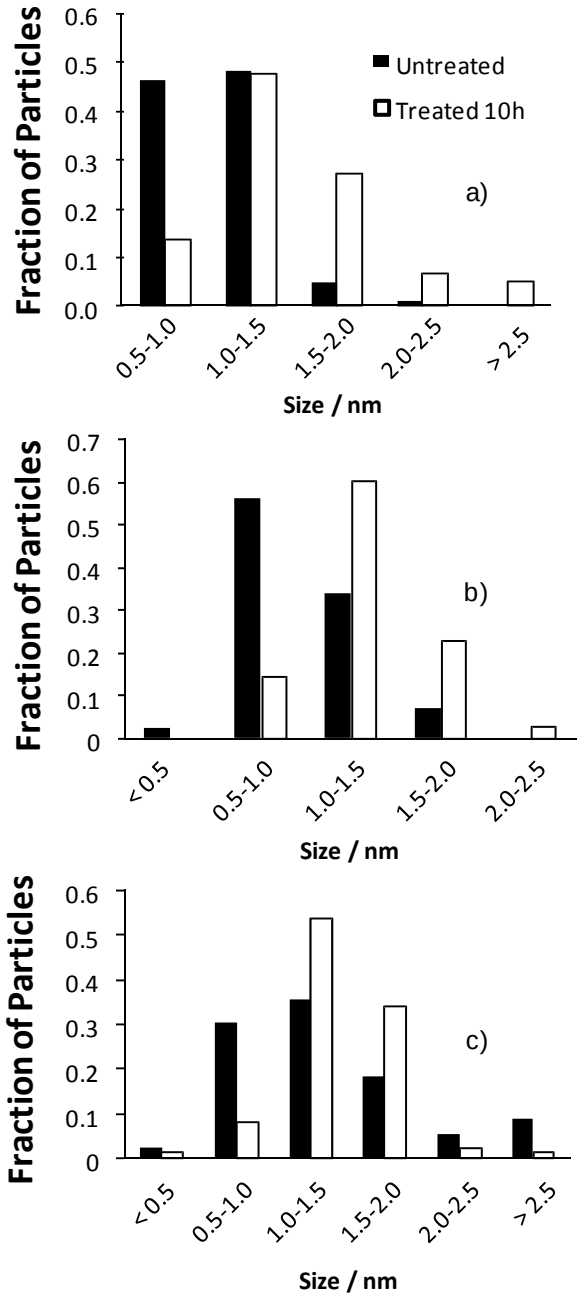

Figure 5.13: Particle size distributions of catalysts before and after treatment in liquid water at 200 °C for 10 h: Pt/γ-Al_2O_3 a), PtAl-PDMS-0.82 b), and PtAl-TEOS-1.97 c).

The particle size distributions as measured from the STEM images illustrate that the PtAl-PDMS-0.82 catalyst had a slightly smaller particle size distribution compared to the original Pt/γ-Al_2O_3 though the average size was the same as Pt/γ-Al_2O_3 at 1.1 nm

(Figures 5.13b, D.3). After the 10 h hot water treatment, the particle size distribution shifted to larger size with an average size of 1.3 nm.

The size distribution of PtAl-TEOS-1.97 was shifted to larger particle diameter compared to the original Pt/γ-Al_2O_3 with an average size of 1.5 nm (Figures 5.13c, D.4). In addition, a significant fraction of large metal particles was observed, with some on the order of 4 nm. After the 10 h hot water treatment, the particle size distribution shifted to larger size though the average size was 1.4 nm, and few particles over 2.5 nm were observed.

5.3.9 Catalyst Performance

Pt/γ-Al_2O_3 and silylated Pt/γ-Al_2O_3 samples were used for aqueous phase reforming of sorbitol to hydrogen according to equation 5.1:

$$6H_2O+C_6H_{14}O_6 \rightarrow 6CO_2 + 13H_2 \qquad [5.1]$$

It is important to mention that aqueous phase reforming can also be tailored for selective production of alkanes when acidic supports are used.

As the catalysts were silylated, the relative turnover number (TON) for hydrogen production (mole H_2 formed/mole active Pt) increased (Figure 5.14). For the TEOS derived catalysts, a maximum in turnover was reached with 1.37 % Si while the catalyst silylated with PDMS precursor had a maximum at 0.82%

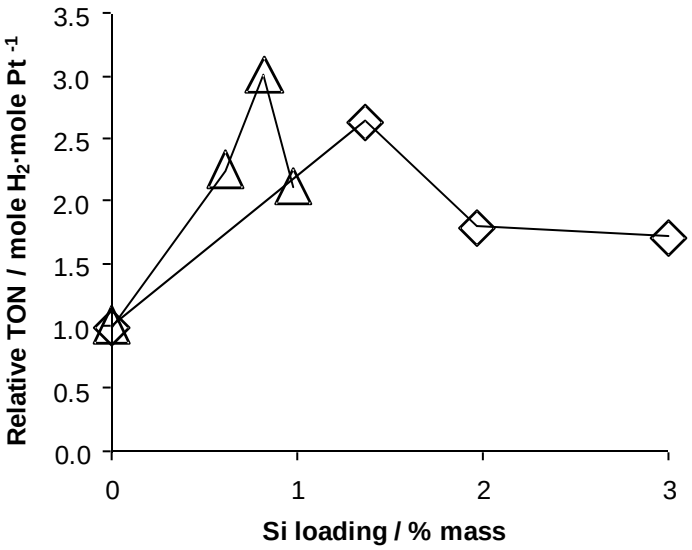

Figure 5.14: Relative turnover number (TON) from aqueous phase reforming of 5 wt% sorbitol with PtAl-PDMS (Δ) and PtAl-TEOS (◊) catalysts.

The yield of CO_2 increased for PtAl-TEOS-1.37 and PtAl-PDMS-0.82 catalyst in addition to higher hydrogen yield (Figure 5.15). The methane yield slightly increased but still remained less than 0.5 %.

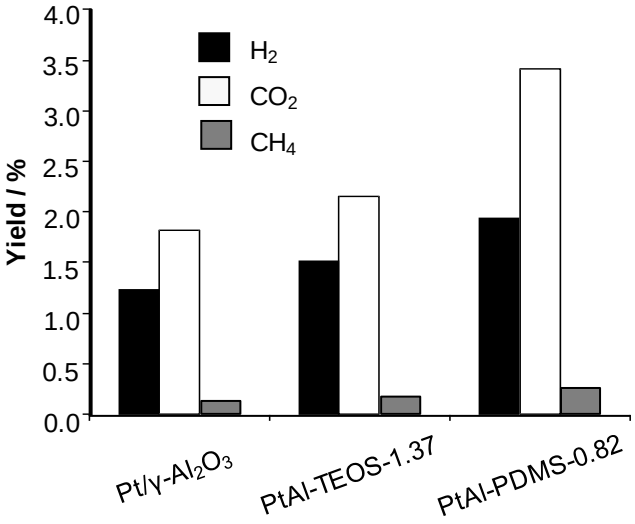

Figure 5.15: Yields of H_2, CO_2 and CH_4 from Pt/γ-Al_2O_3, PtAl-TEOS-1.37 and PtAl-PDMS-0.82 catalysts.

The H_2/CO_2 ratios of Pt/γ-Al_2O_3, PtAl-TEOS-1.37 and PtAl-PDMS-0.82 were 1.5, 1.5 and 1.2, respectively. It should be noted that according to equation [5.1], the molar ratio of H_2/CO_2 would be 2.2 if aqueous phase reforming were the sole reaction pathway of sorbitol.

5.4 Discussion

5.4.1 The Effect of Silica Layers on Hydrothermal Stability of Alumina-Supported Catalysts

5.4.1.1 Stabilization of γ-Al_2O_3

When γ-Al_2O_3 is placed in water, it will hydrate to form either gibbsite ($Al(OH)_3$) or boehmite (AlOOH), with boehmite being the thermodynamically preferred phase at temperatures above 150 °C.[32-33] As a consequence of this phase transformation, the oxide sinters and loses surface area concomitant with a decrease in Lewis acid site concentration.[14] It was shown that the presence of metal particles delays the transformation of alumina to boehmite in hot liquid water. This inhibition was attributed to metal particles adsorbed to basic surface hydroxyl groups, which are also the point of attack for boehmite formation.[14] This conclusion infers that "capping" surface hydroxyl groups, specifically those of basic nature (i.e. singly coordinated hydroxyls), is a viable method to protect alumina from detrimental phase changes in hot liquid water environment. Therefore, the current study considers capping with silicon and the subsequent effect on catalyst hydrothermal stability.

The first objective in the present investigation was to verify that the silylation procedures were effective in depositing silicon on the catalyst surface. The presence of

silicon was verified by ICP/AES analysis, though the silicon loading was significantly less than the amount of silicon added during the liquid deposition procedure (Figure 5.2). Silicon deposition with TEOS resulted in higher loadings compared to PDMS, and this is attributed easier attachment of smaller TEOS moieties compared to bulky PDMS polymeric species. Additionally, TEOS deposition was performed in ethanol/water solution compared to hexane with PDMS thereby making contact with hydrophilic alumina surface more favorable.

The loss of Al-OH groups after silylation treatment was evidenced by both IR and ^{1}H NMR difference spectra indicating the presence of surface species (Figures 5.8 and 5.9). These species are identified as silanol groups both by IR spectroscopy by the peak at 3742 cm^{-1} (Figure 5.9) and by ^{1}H NMR spectroscopy by the peak at 1.6 ppm (Figure 5.8). In addition, silicon species with different degrees of condensation are observed with ^{29}Si MAS NMR spectroscopy (Figure 5.6). The ^{29}Si MAS NMR spectra indicate that the microstructure of surface silicon is affected by the precursor which influences the effective silicon loading. It should be noted that in ^{29}Si NMR spectroscopy, the more adjacent silicon that a given silicon atom is coordinated to, the higher upfield the resonance. As adjacent silicon are substituted by Al or OH groups, the resonance shifts downfield (Table 5.1).[7] By comparison of the ^{29}Si NMR spectra of PtAl-TEOS-1.97 and PtAl-PDMS-0.82, the PDMS sample shows more evidence of formation of Si-O-Al linkages. This is illustrated by the broad shoulder in the low field area (~ 80 – 95 ppm) indicative of Si-O-Al coordination.[7] In contrast, the TEOS precursor seems to facilitate a higher degree of Si-O-Si coordination as seen by the shoulder in the high field area (~ -110 ppm). This indicates formation of multiple silica layers with the TEOS precursor as

the coordination of silicon to neighboring silicon atoms would increase as layers begin to form on top of each other. This is expected as the silicon content of the catalyst from TEOS precursor is about 2.4 times that from PDMS which would facilitate silicon layering. The nitrogen physisorption analysis demonstrates that the surface area of the silylated catalysts does not decrease, therefore attachment of silicon species does not sterically block pores or form a dense layer around the alumina surface (Figure 5.10). Slight increases in surface area were observed and may be due to formation of extended silicon columns or mounds. The increase in SA was more prominent for the TEOS samples and is consistent with the formation of multiple layers or stacking evidenced in the ^{29}Si NMR spectrum.

The stabilizing effect of the silica layers is illustrated by comparison of x-ray diffractograms and ^{27}Al MAS NMR spectra before and after treatment in hot liquid water. X-ray diffraction clearly shows that Pt/γ-Al_2O_3 is converted into a crystalline material within 10 h treatment in hot water. This material is identified as boehmite by comparison to a standard reference (Figure 5.3b).[19] In addition, the ^{27}Al NMR spectrum of Pt/γ-Al_2O_3 treated for 10 h primarily contain peaks of octahedrally coordinated aluminum species, consistent with the structure of boehmite. The fraction of boehmite was determined to 93% by linear combination method of the ^{27}Al NMR spectra of alumina and boehmite.[22] These results are expected at the given reaction conditions, as it was shown that over 60% of γ-Al_2O_3 is converted to boehmite in about 4 hours in liquid water at 200 °C.[14] The sample that contained 0.61% Si from PDMS and subsequently treated for 10 h in hot water had 34% conversion to boehmite while the sample with 1.37% Si from TEOS had 7% conversion. A correlation between the amount of silicon loaded and the fraction of

boehmite formed shows that ~ 2% silicon is enough to effectively inhibit boehmite formation at the given conditions (Figure 5.5).

The inherent stability of the silylated alumina is attributed primarily to the integrity of the Si-O-Al linkage in hot liquid water. This is in agreement with previous investigations of zeolite stability in water, where it was demonstrated that Si-O-Al bonds are more resistant to cleavage compared to Si-O-Si.[18,34] This is supported by the observation that the addition of alumina to silica surface drastically reduced silica solubility in water even with relatively low aluminum loading (~ 5% of the surface).[35] Furthermore, the silylation procedures are effective in capping the most basic surface hydroxyls as indicated by ^{1}H NMR analysis (Figure 5.8), which have been identified as playing a key role in the formation of boehmite.[14] Therefore, these procedures form resilient Si-O-Al linkages at sites that would otherwise be open to water attack responsible for the phase change to boehmite.

Increased hydrophobicity has previously been attributed to increased stability of alumina supported catalysts. It was shown that dip-coating a CuO/Al_2O_3 catalyst in polytetrafluoroethylene fibers prevented formation of cuprous species and minimized solubilization of Cu^{2+} while preventing formation of boehmite in aqueous phase phenol oxidation at 140 °C.[3] It stands to reason that as the surface becomes hydrophobic, water adsorption and subsequent support hydration are hindered. Therefore, one could propose the enhanced stability in the current study arises from an increase in hydrophobicity due to the addition of silicon species. It is well known that when silica is evacuated at high temperature (i.e. calcination at 500 °C), the surface becomes highly hydrophobic.[36] This hydrophobicity arises from the presence of siloxane bridges and isolated silanols which

are assigned to the band at 3742 cm^{-1} in the IR spectra, whereas hydrophilicity corresponds to the presence of adjacent interacting hydroxyls and would be located in the region of 3640-3680 cm^{-1}.[31] Isolated silanols are classified as hydrophobic due to the fact they can interact with water via only one hydrogen bond with an enthalpy of interaction below the enthalpy of liquefaction of water (44 kJ/mol), while adjacent interacting silanols can interact with water via two hydrogen bonds at higher interaction enthalpies.[31] Supporting evidence of hydrophobic nature can also be seen by lower amount of residual water observed by ^{1}H MAS NMR spectroscopy (peak at ~4 ppm), especially for the higher silicon weight loading PDMS samples. Despite this evidence of increased hydrophobicity, the increased stability is not attributed to this phenomenon. This is because of the fact that hydrophobic sites (e.g. Si-O-Si) can be hydrolyzed in water despite their hydrophobic nature,[37] and significant hydrolysis can occur with extended exposure to water at temperatures as low as 60 °C.[38] It was found that faujasite with large Si/Al ratios degrades more readily in hot liquid water than aluminum rich samples which is the opposite trend compared to stability in steam.[18] The structure of the silicon rich sample completely collapsed within 6 h in water at 200 °C. It is also known that the amount of water adsorbed on a zeolite (i.e. hydrophilicity) increases with decreasing Si/Al ratio, where Al content is related to the number of OH groups that can interact with water.[39] Therefore, it has been demonstrated that the more hydrophilic the aluminosilicate material is, the more stable it is in hot liquid water. For this reason, the hydrothermal stability of the catalysts in this study is attributed mainly to the presence of Si-O-Al bonds which is in agreement with the conclusion of the previous investigation on zeolites in hot water.[18]

An alternative hypothesis to explain the increased hydrothermal stability is that it arises from bulk structural modification of the alumina support. For example, the use of dopants is known to have positive effects on hydrothermal stability of alumina in the presence of steam. ConocoPhillips has explored enhancing hydrothermal stability of alumina based catalysts for Fischer-Tropsch synthesis by use of dopants including silicon, cobalt, magnesium and others.[4-6] Similarly, mesoporous γ-Al_2O_3 membranes doped with Ga^{3+} and La^{3+} as well as CeO_2 and ZrO_2 showed improved hydrothermal stability in steam.[1-2] It has been proposed that the additives hamper diffusion of aluminum and oxygen ions and hence resist phase transformation, and it has been shown that dopants can modify the surface energy.[40-42] It should be noted, however, that many doping methods involve addition of the specified dopant during the alumina synthesis procedure or via impregnation, and therefore the stability arises from bulk structural incorporation. In the present study, a comparison of the x-ray diffractograms of the parent catalyst and the silylated samples shows no evidence of structural modification of the alumina (Figure D.1). For example, incorporation of Ga^{3+} into alumina ($\geq$ 5 mol%) was shown to shift the peaks at $2\theta = 45.8°$ and 67° toward lower angles which was not observed in the present case.[1] However, it is possible that smaller amounts of dopant may not result in changes observable via x-ray diffraction. In addition, the ^{27}Al NMR spectra of the parent and silylated catalysts were very similar without peaks corresponding to pentahedrally coordinated aluminum species, which are typically observed in bulk silica-alumina materials.[29] Therefore, it is concluded that bulk silica-alumina is not present, but rather is only found at or near the catalyst surface.

As a final observation, it is seen that TEOS is more effective in preventing the formation of boehmite compared to PDMS which is attributed to more effective silicon deposition (Figure 5.5).

5.4.1.2 Accessibility and Stability of Metal Particles

Before the effect of silicon on metal particle stability can be considered, it is necessary to discuss how silicon deposition initially affects the metal. The possibility of interaction of between metal and silicon and steric hindrance by grafted species has potential to reduce the number of accessible active sites. For example, surface silylation of cobalt based Fischer-Tropsch synthesis (FTS) catalysts resulted in the presence of CoO species that were difficult to reduce due to a strong interaction between CoO and Si-OH groups,[43] and surface silylation with hexamethylsilazane of a Co/SBA-15 catalyst decreased FTS activity which was attributed to steric hindrance of cobalt by grafted silicon species.[44]

The dispersion analysis by H_2/O_2 titration of the silylated catalysts in this study indicates about half of the active metal surface area is lost after the lowest silicon loading and subsequent calcination (Table 5.3). Analysis of the TEM micrographs of the silylated catalysts indicate that the initial size distributions are close to the original Pt/γ-Al_2O_3 (Figure 5.13), and therefore the loss in metal area measured by hydrogen chemisorption is attributed to partial coverage or encapsulation of metal particles. It is of interest to note that PtAl-TEOS-1.97 had larger particles compared to Pt/γ-Al_2O_3. For both silicon precursors, the main loss in active metal surface area occurs at the lowest loading and remains relatively constant afterward. This illustrates that any additional silicon tends not to bond to metal. It is likely that some additional silicon bonds to surface bound silicon, especially in the case of the TEOS precursor which shows evidence of multilayer

formation (*vida supra*). However, the bulk of additional silicon above the lowest loading likely interacts with exposed hydroxyls, and it is readily observed in the ^{1}H NMR analysis that a larger silicon resonance corresponds with a larger decrease in hydroxyl group concentration (Figure 5.8).

These exposed hydroxyl groups are readily available as silylation sites on the metal impregnated alumina. The TEM analysis shows that the average platinum cluster size is 1.1 nm for Pt/γ-Al_2O_3 (Figure 5.13a). Assuming a monolayer, each cluster contains roughly 16 atoms (Pt atomic radius = 139 pm). At the present metal loading of 1 wt%, the Pt particles therefore cover only ~2% of the total surface area of γ-Al_2O_3 (BET surface area = 90 m^2/g). The leftover hydroxyl groups can then interact with silicon species. Therefore, it is concluded that the silicon "fills in" the exposed alumina surface between the metal particles essentially isolating them. The TEM micrograph of the unsilylated Pt/Al_2O_3 catalyst shows initially well dispersed metal particles, which insures that the isolated particles are evenly distributed over the surface (Figure 5.12). One could also envision performing metal impregnation after silylation treatment which would prevent the covering of active metal surface area. It was shown that silylation with dichlorodimethylsilane of a supported Pd/SiO_2 catalyst resulted in blocking about 50% of active sites compared to metal impregnation after silyation of the support.[45] However, it may be difficult to then control where platinum is deposited. It is generally concluded that the thermal stability of a given metal is greater on Al_2O_3 than on SiO_2, therefore enhanced sintering on silica might be expected and deposition on alumina is preferred.[46] The amount of silicon deposited and dispersion would also have to be well controlled, as it was shown that platinum impregnated on TEOS loaded alumina support exhibited

different sintering behavior with silicon loading. A thin layer of silica (i.e. monolayer) was effective in preventing particle sintering while multiple layers did not prevent sintering because of bulk silica-like character.[47]

Now that a sense of the deposited silicon layer is established, the consequence on hydrothermal stability is discussed. The agglomeration of metal particles is detrimental to catalyst activity as the active metal surface area effectively decreases. For example, the deactivation of Ru/Al_2O_3 catalyst for glucose hydrogenation has been attributed to Ru crystal growth in addition to crystallization of the support (e.g. formation of boehmite).[48] The formation of boehmite and sintering of metal particles has been shown to contribute to deactivation of alumina supported Ni and Co catalysts for aqueous phase reforming of glycerol, although no deactivation of $Pt/\gamma\text{-}Al_2O_3$ catalyst was observed despite the support phase change and sintering.[49] These results are somewhat surprising, and may indicate that activity for APR of glycerol in this case was not limited by the number of metal sites as the catalyst weight loading was relatively high ($\geq$ 4 wt%). However, sustained sintering will reduce the accessible metal surface area and thus lead to deactivation.

The sintering of platinum particles can occur via multiple mechanisms, although two are considered in this study. The first consists of support degradation whereby crystallization or deformation of the support forces metal particles to come into close proximity with each other and coalesce, or the formation of crystalline material encapsulates or blocks access to metal sites. The second mechanism is migration of platinum particles or crystallites across the support surface followed by coalescence.

Therefore, any attempt to prevent sintering would have to address both of support stabilization and surface mobility of metal particles.

After hydrothermal treatment, sintering was observed for both Pt/γ-Al_2O_3 and the silylated catalysts as measured both by hydrogen titration and TEM. The titration method shows that PtAl-TEOS-1.97 and PtAl-PDMS-0.82 retained more than twice the amount of active metal surface area after 10 h treatment in hot water as compared to Pt/γ-Al_2O_3. The change in particle size distribution for all samples measured by microscopy showed that particles grew in size; however, they were significantly smaller than the sizes calculated from the hydrogen chemisorption analysis. This is especially apparent for the treated Pt/γ-Al_2O_3 catalyst where the average calculated metal particle size was 12 nm compared to an average size of 1.5 nm as measured by TEM (Table 5.3, Figure 5.13a). This large discrepancy indicates that the change in support morphology significantly contributes to loss in active metal surface area. This is speculated to arise from hindered access or encapsulation of metal sites as a result of boehmite formation. Since the silylation treatments result in less formation of boehmite, active metal surface area is preserved for a longer period of time as demonstrated by chemisorption analysis. The TEM results also indicate that particle growth is somewhat inhibited for both PDMS and TEOS silylated catalysts. When Pt/γ-Al_2O_3 was treated for 10 h, over 10% of metal particles were larger than 2 nm with an average size of 1.5 nm. Meanwhile, the treated silylated catalysts had ca. 3% of the larger particles with average sizes of 1.3 and 1.4 nm for the PDMS and TEOS precursors, respectively. Therefore, the treated silyated samples had slightly smaller average particle sizes as well as a smaller fraction of large metal particles (> 2 nm) compared to the Pt/γ-Al_2O_3. These results indicate that the silylation

treatment may actually slow or prevent sintering by hindering metal particle mobility and coalescence during immersion in hot liquid water. This seems plausible considering that silicon acts to form a barrier between metal clusters, and similar results of reduced sintering were observed with a silylated Pt/ZSM-5 catalyst.[50] Therefore, the increase in overall metal particle stability is attributed to two mechanisms. The first is prevention of boehmite formation which can block access to active sites, and the second is hindered metal particle mobility on the surface.

5.4.2 The Effect of Silicon on Catalyst Performance

Surface silylation and its effect on activity of supported catalysts has been considered for a variety of reactions including Fischer-Tropsch synthesis, [4-6,43-44] Suzuki coupling of aryl halides and arylboronic acids,[51] and hydrogenation of aromatic ketones and methyl acrylate.[45,52] To the authors' knowledge, there is no such investigation of this type for aqueous phase reforming catalysts.

As illustrated in Figure 5.14, the turnover number of the silylated catalysts increases relative to the parent Pt/γ-Al_2O_3. This is attributed to two main factors, namely the preservation of active metal surface area and changes to the surface acidity with silicon loading. As previously discussed, silylation treatment preserves the metal particle accessibility over time, where the silylated catalysts retain about twice the active metal surface area after hydrothermal treatment compared to Pt/γ-Al_2O_3. Therefore, it is expected that a given platinum cluster is active for a longer period of time resulting in increased turnover. This conclusion is in line with recent results showing that metal sintering is prevented by deposition of Al_2O_3 layers on Pt/SiO_2 which increased the activity for methanol decomposition.[53] It is interesting to note that there are different

maxima in relative TON depending on the precursor. As it has already been discussed that these precursors result in different actual silicon loading and hence different silicon microstructures, it is suggested that different stabilization and catalytic properties according to silicon loading arise between the two precursors.

In terms of acidity, it has been established that silylation changes acidic characteristics which in turn affects the overall activity and/or selectivity of the catalyst. The acidity of silica coated oxide particles coated by liquid deposition of TEOS increased up to a loading of 400 $mg \cdot g_{alumina}^{-1}$ after which it decreased, and these changes were attributed to the difference in silica structure with weight loading.[10] The 400 $mg \cdot g_{alumina}^{-1}$ loading contained primarily tri-layered silica and subsequent layering resulted in loss of acid sites, though the nature of the active acid sites was not discussed. The activity of these catalysts for acid-catalyzed cumene cracking at 450 °C correlated well to the changes in the acidity.[10] Another investigation of alumina coated with silica by chemical vapor deposition of TEOS showed a maximum in cumene cracking activity at 468 °C at 20 wt% silicon with increased activity again correlating to Brønsted acidity.[7] Silicon weight loadings above 20% formed $Si\text{-}(O\text{-}Si)_4$ species which were speculated to contribute to decreased acidity and hence activity. ZSM-5 coated multiple times with 10% PDMS/hexane solution resulted in decreased acidity with each successive silylation treatment.[13] The decrease was attributed to the elimination of external acid sites and silanol hydroxyls, however no analysis of the resulting silicon layers was performed making a comparison to the previously cited investigations difficult. However, the nature of the precursor and support must play a role. ZSM-5 has inherent Brønsted acidic sites which may interact with PDMS resulting in the observed decreased acidity.[13]

All of the silylated catalysts in this investigation showed a decrease in total acid site concentration at the lowest silicon weight loading compared to the original catalyst (Table 5.2). No Brønsted acidity was detected for bare alumina and Pt/γ-Al_2O_3, and it has been suggested that alumina does not contain OH groups capable of protonating pyridine.[54] However, Brønsted acid sites were detected for all TEOS silylated catalysts and for PDMS silylated catalysts at 0.82 and 0.98 wt% silicon loading. These acid sites are attributed to Si-OH-Al groups and Brønsted acidity can also arise from silanol groups with aluminum atom neighbors.[55] When considering the pathways for aqueous phase reforming of sorbitol, a decrease in total acid site concentration favors hydrogen production (Figure 5.16).[56]

.

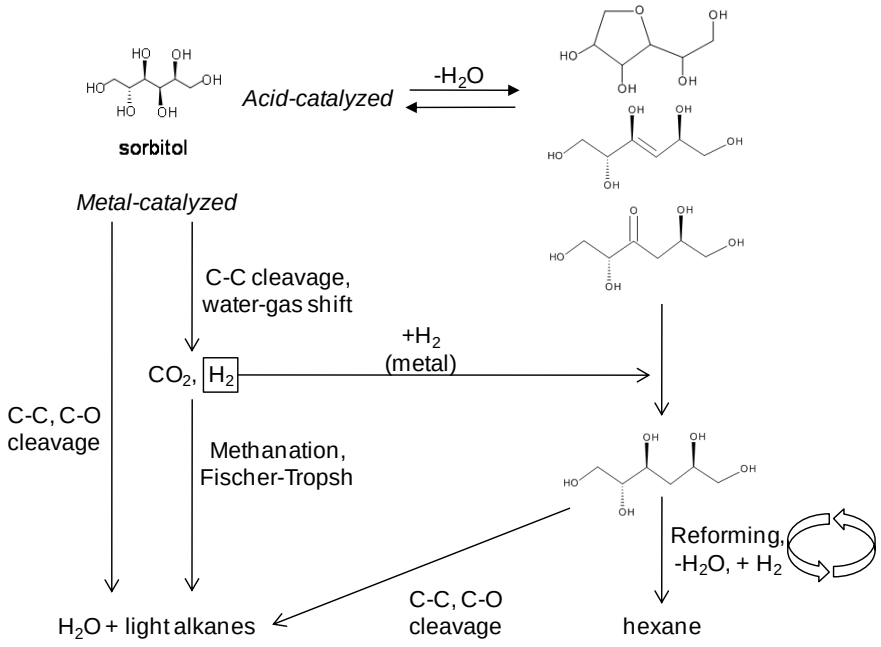

Figure 5.16: Metal and acid catalyzed routes of sorbitol reforming.

This is because lower acidity avoids dehydration and therefore favors purely metal catalyzed reaction pathways. It was directly demonstrated that selectivity is shifted away from hydrogen as the concentration of solid acid sites increases by adding SiO_2-Al_2O_3 to Pt/Al_2O_3 in reforming of a 5wt% sorbitol solution.[56]

In addition to stabilization of active metal sites and decreased acidity, changes in the surface polarity may play a role in increased hydrogen yield. It has been demonstrated that increased hydrophobicity of catalyst surfaces can increase adsorption of organic reactants and hence the overall activity. For example, the rate of esterification of long chain fatty acids increased with increasing catalyst hydrophobicity.[57] It has also been shown that catalytic activity of supported Pd catalysts for Suzuki coupling is linked to support hydrophobicity due to increased concentration of the organic substrate near the catalyst surface.[51] Silylation of Pd/SiO_2 catalyst affected the hydrophobic character of the catalyst consequently increasing adsorption of organic reactants and thus activity for selective hydrogenation of aromatic ketones.[52] Therefore, with increased hydrophobicity it is feasible that sorbitol adsorption on the surface becomes more favorable and hence increases the local concentration of reactant near catalytically active metal sites.

According to equation [5.1], the molar ratio of H_2/CO_2 would be 2.2 if aqueous phase reforming were the sole reaction pathway of sorbitol. As all of these ratios are smaller than the expected value, it is apparent that sorbitol takes part in additional reaction pathways that yield carbon dioxide. It is of no surprise that sorbitol undergoes multiple reaction pathways during aqueous phase processing as investigations of both the liquid and gas phase products of sorbitol APR with Pt/Al_2O_3-SiO_2 have shown a large variety of reaction products.[58-59] Methane formation occurs via C-O bond scission followed by

hydrogenation and subsequent hydration/dehydrogenation and also by hydrogenation/dehydration of adsorbed CO.[60] Therefore, in order to prevent methanation, the catalyst should promote removal of CO by WGS. The low formation of methane in the current study indicates promotion of WGS (Figure 5.15). This is expected since platinum has been shown to have the highest selectivity for H_2 production among transition metals. In addition, Pt supported on alumina shows higher H_2 TOF compared to platinum on SiO_2-Al_2O_3 which is in turn higher than platinum on SiO_2.[60] The increased turnover of hydrogen production from the silylated catalysts is different than what is expected for Pt supported on bulk SiO_2-Al_2O_3 compared to just Al_2O_3 illustrating unique properties obtained by surface silylation.

5.5 Conclusions

A Pt/γ-Al_2O_3 catalyst was modified via a liquid phase surface silylation procedure utilizing two different silicon precursors (tetraethylorthosilicate and polydimethylsiloxane) in an attempt to increase hydrothermal stability in aqueous phase reforming environments. It was demonstrated that both silylation procedures effectively hinder transformation of γ-Al_2O_3 to crystalline boehmite in water at 200 °C. This increase in catalyst structural stability is mainly attributed to the formation of stable Si-O-Al bonds. The addition of silicon did not significantly alter the catalyst parent structure and did not result in decreased surface area, but active metal surface area was seen to decrease with the lowest silicon loading (10 wt%) which is attributed to partial coverage of platinum species. The metal particles sinter on Pt/γ-Al_2O_3 after 10 h treatment in 200 °C water, and there is indication that silylation may slow this process. In addition to sintering, metal surface area on the Pt/γ-Al_2O_3 catalyst is lost due to encapsulation by

crystalline boehmite whereas this phenomenon is mitigated by support stabilization from silica. Catalyst performance based on turnover number showed that activity for hydrogen production increased depending on the amount of silicon loaded and the precursor used despite the loss of active metal species, and this can be attributed to decrease in support acidity, preservation of active sites and increased hydrophobicity resulting in increased organic molecule adsorption. These results present a promising approach to modify alumina based catalysts for use in aqueous phase reforming environments.

5.6 References

[1] Zahir, M. H.; Sato, K.; Mori, H.; Iwamoto, Y.; Nomura, M.; Nakao, S.-i. *Journal of the American Ceramic Society* **2006**, *89*, 2874-2880.

[2] Zahir, M. H.; Ikuhara, Y. H.; Fujisaki, S.; Sato, K.; Nagano, T.; Iwamoto, Y. *Journal of Materials Research* **2007**, *22*, 3201-3209.

[3] Massa, P.; Ivorra, F.; Haure, P.; Fenoglio, R. *Catalysis Communications* **2009**, *10*, 1706-1710.

[4] Espinoza, R.; Jothimurugesan, K.; Jin, Y.; Ortego, J., J. Dale; Fjare, K.; Ortego, B. C. Stabilized Boehmite-Derived Catalyst Supports, Catalysts, Methods of Making and Using; ConocoPhillips Company: USA, **2008**; pp 1-46.

[5] Jin, Y.; Espinoza, R. L.; Srinivasan, N.; Ionkina, O. P. Stabilized Transition Alumina Catalyst Support from Boehmite and Catalysts Made Therefrom; ConocoPhillips Company: USA, **2008**; pp 1-21.

[6] Jin, Y.; Jothimurugesan, K.; Fjare, K. A.; Ortego, J., J. Dale; Ortego, B. C.; Espinoza, R. L. Stabilized Boehmite-Derived Catalyst Supports, Catalysts, Methods of Making and Using; ConocoPhillips Company: USA, **2008**.

[7] Sato, S.; Sodesawa, T.; Nozaki, F.; Shoji, H. *Journal of Molecular Catalysis* **1991**, *66*, 343-355.

[8] Kodakari, N.; Tomita, K.; Iwata, K.; Katada, N.; Niwa, M. *Langmuir* **1998**, *14*, 4623-4629.

[9] Sato, S.; Takahashi, R.; Sodesawa, T.; Tanaka, R. *Bulletin of the Chemical Society of Japan* **2003**, *76*, 217-223.

[10] Sato, S.; Takahashi, R.; Sodesawa, T.; Shin, D.; Ichikawa, N.; Ogura, K. *Bulletin of the Chemical Society of Japan* **2006**, *79*, 649-655.

[11] Zheng, S.; Heydenrych, H. R.; Roger, H. P.; Jentys, A.; Lercher, J. A. *Topics in Catalysis* **2003**, *22*, 101-106.

[12] O'Connor, C. T.; Moller, K. P.; Manstein, H. *Cattech* **2001**, *5*, 172-182.

[13] Zhu, Z.; Xie, Z.; Chen, Q.; Kong, D.; Li, W.; Yang, W.; Li, C. *Microporous and Mesoporous Materials* **2007**, *101*, 169-175.

[14] Ravenelle, R. M.; Copeland, J. R.; Kim, W. G.; Crittenden, J. C.; Sievers, C. *ACS Catalysis* **2011**, *1*, 552-561.

[15] Datka, J.; Turek, A. M.; Jehng, J. M.; Wachs, I. E. *Journal of Catalysis* **1992**, *135*, 186-199.

[16] Benson, J. E.; Boudart, M. *Journal of Catalysis* **1965**, *4*, 704-710.

[17] Delannay, F., Ed. *Characterization of Heterogeneous Catalysts*; Marcel Dekker: New York, **1984**; Vol. 15.

[18] Ravenelle, R. M.; Schüβler, F.; D'Amico, A.; Danilina, N.; van Bokhoven, J. A.; Lercher, J. A.; Jones, C. W.; Sievers, C. *The Journal of Physical Chemistry C* **2010**, *114*, 19582-19595.

[19] Wefers, K.; Misra, C. *Alcoa Technical Paper* **1987**.

[20] Linsen, B. G.; Fortuin, J. M. H.; Okkerse, C.; Steggerda, J. J., Eds. *Pysical and Chemical Aspects of Adsorbents and Catalysts*; Academic Press: New York, **1970**.

[21] Pecharroman, C.; Sobrados, I.; Iglesias, J. E.; Gonzalez-Carreno, T.; Sanz, J. *The Journal of Physical Chemistry B* **1999**, *103*, 6160-6170.

[22] Urretavizcaya, G.; Cavalieri, A. L.; López, J. M. P.; Sobrados, I.; Sanz, J. *Journal of Materials Synthesis and Processing* **1998**, *6*, 1-7.

[23] Maciel, G. E.; Sindorf, D. W. *Journal of the American Chemical Society* **1980**, *102*, 7606-7607.

[24] Decanio, E. C.; Edwards, J. C.; Bruno, J. W. *Journal of Catalysis* **1994**, *148*, 76-83.

[25] Kraus, H.; Prins, R. *Journal of Catalysis* **1996**, *164*, 260-267.

[26] Mastikhin, V. M.; Mudrakovsky, I. L.; Nosov, A. V. *Progress in Nuclear Magnetic Resonance Spectroscopy* **1991**, *23*, 259-299.

[27] Crepeau, G.; Montouillout, V.; Vimont, A.; Mariey, L.; Cseri, T.; Mauge, F. *Journal of Physical Chemistry B* **2006**, *110*, 15172-15185.

[28] Liu, X.; Truitt, R. E. *Journal of the American Chemical Society* **1997**, *119*, 9856-9860.

[29] Williams, M. F.; Fonfe, B.; Sievers, C.; Abraham, A.; van Bokhoven, J. A.; Jentys, A.; van Veen, J. A. R.; Lercher, J. A. *Journal of Catalysis* **2007**, *251*, 485-496.

[30] Brunner, E. *Catalysis Today* **1997**, *38*, 361-376.

[31] Bolis, V.; Fubini, B.; Marchese, L.; Martra, G.; Costa, D. *Journal of the Chemical Society, Faraday Transactions* **1991**, *87*, 497-505.

[32] Holleman, A. F.; Wiberg, E. *Inorganic Chemistry, 34th Edition*; Academic Press, **2001**.

[33] MacDonald, D. D.; Butler, P. *Corrosion Science* **1973**, *13*, 259-274.

[34] Lutz, W.; Toufar, H.; Kurzhals, R.; Suckow, M. *Adsorption-Journal of the International Adsorption Society* **2005**, *11*, 405-413.

[35] Iler, R. K. *Journal of Colloid and Interface Science* **1973**, *43*, 399-408.

[36] Okuhara, T. *Chemical Reviews* **2002**, *102*, 3641-3666.

[37] Castricum, H. L.; Sah, A.; Kreiter, R.; Blank, D. H. A.; Vente, J. F.; ten Elshof, J. E. *Journal of Materials Chemistry* **2008**, *18*, 2150-2158.

[38] Imai, H.; Morimoto, H.; Tominaga, A.; Hirashima, H. *Journal of Sol-Gel Science and Technology* **1997**, *10*, 45-54.

[39] Olson, D. H.; Haag, W. O.; Lago, R. M. *Journal of Catalysis* **1980**, *61*, 390-396.

[40] Church, J. S.; Cant, N. W.; Trimm, D. L. *Applied Catalysis A: General* **1993**, *101*, 105-116.

[41] Ozawa, M.; Kimura, M.; Isogai, A. *Journal of the Less Common Metals* **1990**, *162*, 297-308.

[42] Castro, R. H. R.; Ushakov, S. V.; Gengembre, L.; Gouvêa, D.; Navrotsky, A. *Chemistry of Materials* **2006**, *18*, 1867-1872.

[43] Xie, R.; Li, D.; Hou, B.; Wang, J.; Jia, L.; Sun, Y. *Catalysis Communications* **2011**, *12*, 589-592.

[44] Jia, L.; Jia, L.; Li, D.; Hou, B.; Wang, J.; Sun, Y. *Journal of Solid State Chemistry* **2011**, *184*, 488-493.

[45] Omota, F.; Dimian, A. C.; Bliek, A. *Applied Catalysis A: General* **2005**, *294*, 121-130.

[46] Bartholomew, C. H. *Applied Catalysis A: General* **2001**, *212*, 17-60.

[47] Hayashi, K.; Horiuchi, T.; Suzuki, K.; Mori, T. *Catalysis Letters* **2002**, *78*, 43-47.

[48] Arena, B. J. *Applied Catalysis A: General* **1992**, *87*, 219-229.

[49] Wen, G.; Xu, Y.; Ma, H.; Xu, Z.; Tian, Z. *International Journal of Hydrogen Energy* **2008**, *33*, 6657-6666.

[50] Kanazawa, T. *Catalysis Letters* **2006**, *108*, 45-47.

[51] Soomro, S. S.; Röhlich, C.; Köhler, K. *Advanced Synthesis & Catalysis* **2011**, *353*, 767-775.

[52] Quintanilla, A.; Bakker, J. J. W.; Kreutzer, M. T.; Moulijn, J. A.; Kapteijn, F. *Journal of Catalysis* **2008**, *257*, 55-63.

[53] Feng, H.; Lu, J.; Stair, P.; Elam, J. *Catalysis Letters* **2011**, *141*, 512-517.

[54] Morterra, C.; Magnacca, G. *Catalysis Today* **1996**, *27*, 497-532.

[55] Xu, B.; Sievers, C.; Lercher, J. A.; van Veen, J. A. R.; Giltay, P.; Prins, R.; van Bokhoven, J. A. *The Journal of Physical Chemistry C* **2007**, *111*, 12075-12079.

[56] Huber, G. W.; Cortright, R. D.; Dumesic, J. A. *Angewandte Chemie - International Edition* **2004**, *43*, 1549-1551.

[57] Satyarthi, J. K.; Srinivas, D.; Ratnasamy, P. *Energy & Fuels* **2010**, *24*, 2154-2161.

[58] Li, N.; Huber, G. W. *Journal of Catalysis* **2010**, *270*, 48-59.

[59] Kirilin, A. V.; Tokarev, A. V.; Murzina, E. V.; Kustov, L. M.; Mikkola, J.-P.; Murzin, D. Y. *ChemSusChem* **2010**, *3*, 708-718.

[60] Huber, G. W.; Dumesic, J. A. *Catalysis Today* **2006**, *111*, 119-132.

CHAPTER 6

FINAL CONCLUSIONS AND RECOMMENDATIONS

It is the intent of this dissertation to have illustrated the importance of considering catalyst material stability in high temperature aqueous environments. The field of aqueous phase heterogeneously catalyzed conversion of biomass derived compounds is relatively young, and a host of new catalysts will likely be examined in years to come. With the interest of finding new and highly active/selective catalysts, it is imperative that researchers consider issues of material stability under realistic reforming conditions. This kind of investigation is critical to find stable, reusable catalysts that can usher in the utilization of biomass to produce fuels and commodity chemicals.

It is shown in Chapter 2 that the hydrothermal stability of solid acid materials in water can be unique as compared to typical hydrothermal stability studies in air or steam. While investigating the stability of zeolites Y and ZSM-5, it was discovered that ZSM-5 was quite stable compared to Y, which is consistent with steaming investigations. However, it was discovered that low Si/Al ratios in zeolite Y led to higher stability, which is opposite of the trend in steaming. It was proposed that in liquid environment, Si-O-Si hydrolysis is the primary degradation mechanism whereas dealumination is responsible for collapse in steam. This is an excellent illustration of the importance in studying material stability under real reaction conditions (i.e. liquid water).

In Chapter 3, many of the techniques from Chapter 2 were utilized to explore hydrothermal stability of alumina based catalysts in hot water environment. Alumina is one of the most widely used catalyst supports, and has been used in a variety of aqueous phase conversion processes. It was found that alumina converts to a crystalline hydrate

material (boehmite) with a concomitant loss in surface area and Lewis acid site concentration. These results are not surprising, as it is well established that this alumina hydroxide phase is thermodynamically preferred under the given conditions. However, the results of this study are unique in that it was demonstrated this transformation occurs on the order of hours under these conditions. Additionally, the presence of metal particles was seen to significantly slow the transformation kinetics compared to bare γ-Al_2O_3. By investigating where these metal particles sit on the catalyst surface, it was deduced that a certain species of surface hydroxyl group (i.e. "basic" hydroxyls) are responsible for boehmite formation and could potentially offer a route to effectively stabilize the material.

The effect of platinum precursor as it relates to stability and catalyst activity for production of sugar alcohols from cellulose was the subject of investigation in Chapter 4. The rate of boehmite formation was dependent on the precursor, and it was seen that catalysts derived from H_2PtCl_6 exhibited higher cellulose conversion. The chlorine containing precursor also resulted in significant catalyst dissolution, and it was directly shown that dissolved aluminum species have catalytic activity for the hydrolysis of cellulose implying catalyst dissolution as one explanation for the higher activity. This observation is important in that catalyst stability is shown to have direct influence on reaction mechanisms which has not been previously considered.

The aim of Chapter 5 was to utilize knowledge gained from the preceding investigations of alumina to design a catalyst with high hydrothermal stability. To do this, alumina supported catalysts were coated with a silicon layer via chemical liquid deposition. The result was that catalyst stability, or the resistance to boehmite formation,

was greatly increased. Analysis of the deposited silicon species showed that basic hydroxyl groups had been effectively blocked, further strengthening the case for these as initial boehmite formation sites. In addition to increased support stability, the turnover frequency of hydrogen production from aqueous phase reforming of sorbitol increased, which is attributed to longer activity of metal particles due to increased stability.

With the above mentioned results, the investigations contained in this dissertation have identified some important details relevant to the field. The mechanisms of hydrothermal degradation of common catalytic materials have been elucidated, and some unexpected effects of catalyst instability were observed (i.e. dissolution resulting in increased activity). Using information gathered from these studies, a more stable catalyst was created that even exhibited enhanced activity. These findings establish some starting points for the design of solid catalysts under such aqueous reforming conditions. However, the results thus presented are by no means complete as there are many investigations that are still needed. With this idea in mind, some recommendations for future work are discussed.

The first recommendation is to extend these stability studies to solutions that are more representative of reforming medium. For example, the effect of common biomass compounds such as glucose, sugar alcohols, organic acids etc. on catalyst degradation characteristics would be highly relevant. Some preliminary work has shown that addition of sugar alcohols with different chain lengths can alter boehmite formation kinetics (Figure 6.1). This is likely due to different adsorption capacities on the support which effectively inhibit water attack and subsequent boehmite formation. It was also observed that a collapse of zeolite Y41 was delayed in 1M glucose solution compared to solutions

of glycerol, and acetic acid, which is likely due to glucose coking on the surface (Figure 6.2). This information may potentially be useful when considering what kinds of feedstocks are favorable purely from a stability standpoint.

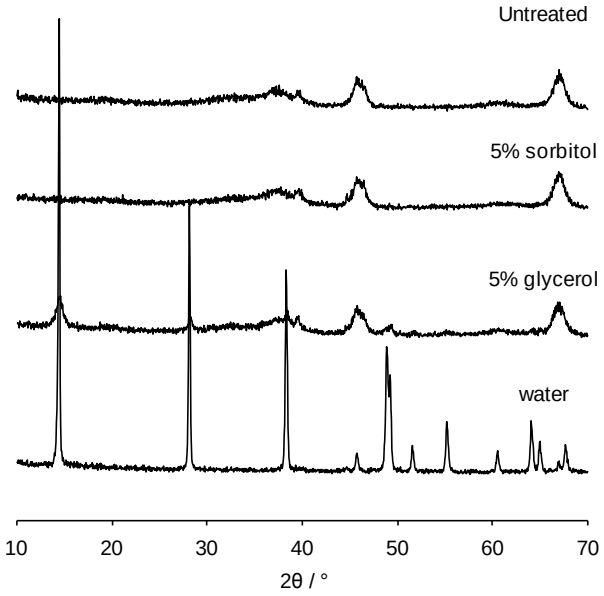

Figure 6.1: X-ray diffractograms of Pt/γ-Al_2O_3 catalyst treated for 10 h at 225 °C in model biomass solutions.

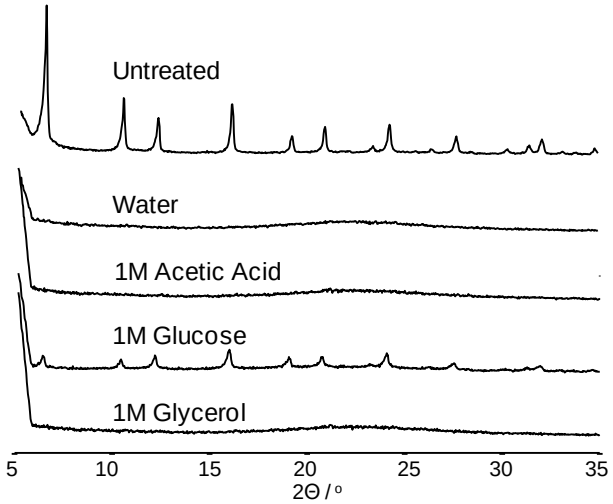

Figure 6.2: X-ray diffractograms of zeolite Y41 treated for 10 h at 200 °C in model biomass solutions.

In addition to exploring the effects of different liquid compositions, some comprehensive stability studies on more common support materials should be performed. This would include activated carbon and other metal oxides (e.g. ZrO_2, CeO_2). For example, TiO_2 anatase phase is highly unstable in aqueous environment and it has been shown that after 105 minutes in 200 °C water the surface roughens which is attributed the hydrolysis and subsequent partial dissolution of anatase.[1] Similarly, hydrothermal treatment of ZrO_2 can result in the phase transformation of tetragonal to monoclinic which is accompanied by surface cracking and spalling because of the volume increase from tetragonal to monoclinic phase.[2] Therefore, it would be worthwhile to know more about the stability of these materials before using them as catalyst supports. After identifying inherently more stable supports, investigations on how to increase activity/selectivity could then be performed.

Another recommendation for future work directly applied to alumina is to explore different capping agents in addition to silicon. Grafting of organometallics onto surface hydroxyls may be a promising route as it has been shown that grafting of $GeBu_4$ to surfaces of mordenites is thermally stable up to 400 °C.[3] These could essentially play the same role as silicon and block water attack. In addition to increasing stability, the grafted species may also exhibit interesting catalytic properties as it has been shown that zirconium grafted on silica is active for hydrogenolysis of simple alkanes at mild temperatures.[4]

In closing, there is great potential for heterogeneously catalyzed processes to usher in the use of lignocellulosics to produce fuels and chemicals. The field is growing rapidly and many advances have been made in recent years. I hope that the work presented in this

dissertation proves useful to other researchers by providing some foundational studies on catalyst material stability under lignocellulosic reforming conditions.

6.1 References

[1] Yang, X. H.; Li, Z.; Sun, C.; Yang, H. G.; Li, C. *Chemistry of Materials* **2011**, *23*, 3486-3494.

[2] Adair, J. H.; Krarup, H. G.; Venigalla, S.; Tsukada, T. *MRS Online Proceedings Library* **1996**, *432*, null-null.

[3] Nédez, C.; Choplin, A.; Corker, J.; Basset, J.-M.; Joly, J.-F.; Benazzi, E. *Journal of Molecular Catalysis* **1994**, *92*, L239-L244.

[4] Corker, J.; Lefebvre, F.; Lécuyer, C.; Dufaud, V.; Quignard, F.; Choplin, A.; Evans, J.; Basset, J.-M. *Science* **1996**, *271*, 966-969.

APPENDIX A

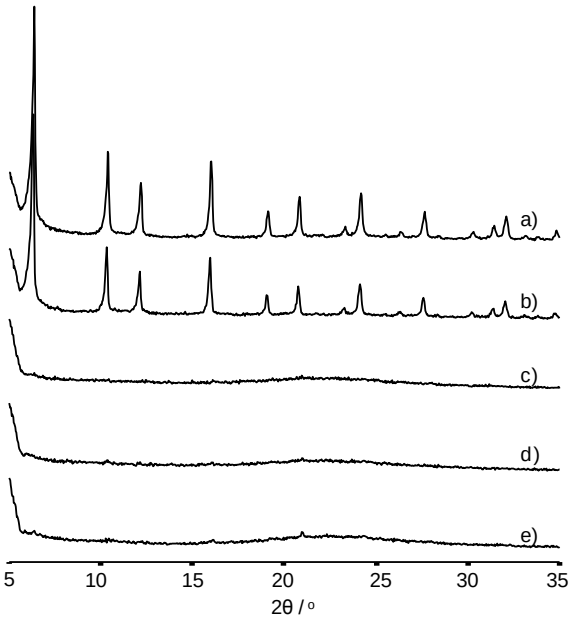

Figure A.1: X-ray diffractograms of zeolite Y41 treated at 150 °C: a) untreated, b) 1 h, c) 2 h, d) 4 h, e) 6 h.

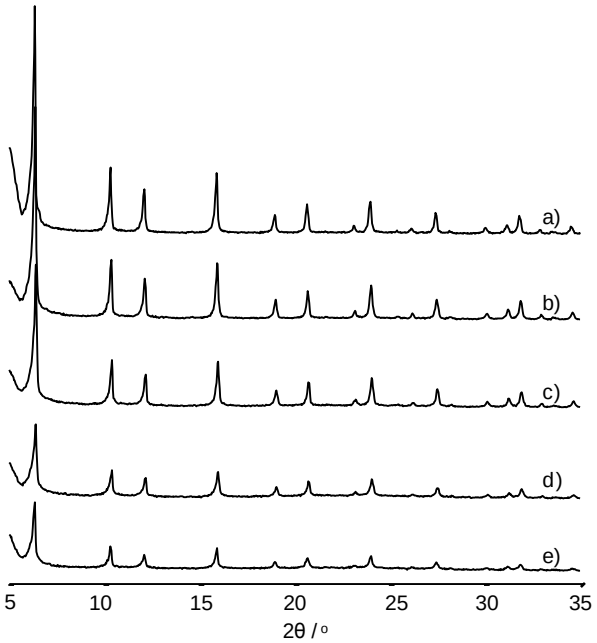

Figure A.2: X-ray diffractograms of zeolite Y14 treated at 200 °C: a) untreated, b) 1 h, c) 2 h, d) 4 h, e) 6 h.

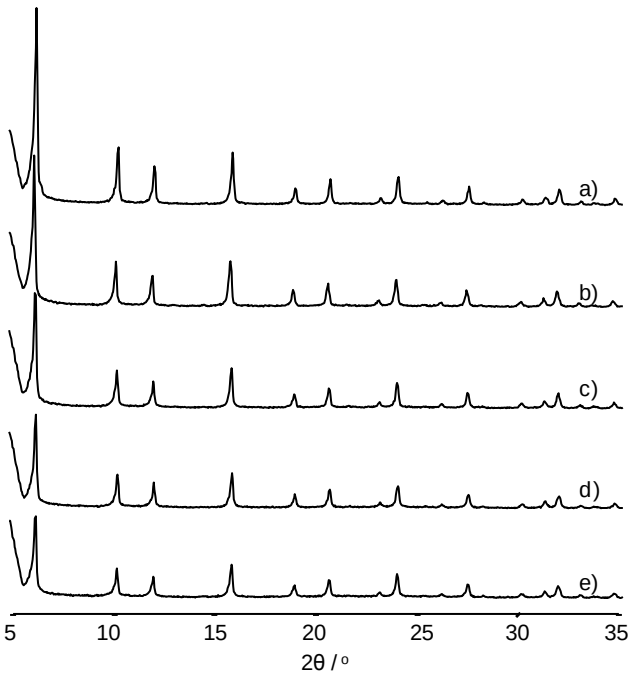

Figure A.3: X-ray diffractogram of zeolite Y14 treated at 150 °C: a) untreated, b) 1 h, c) 2 h, d) 4 h, e) 6 h.

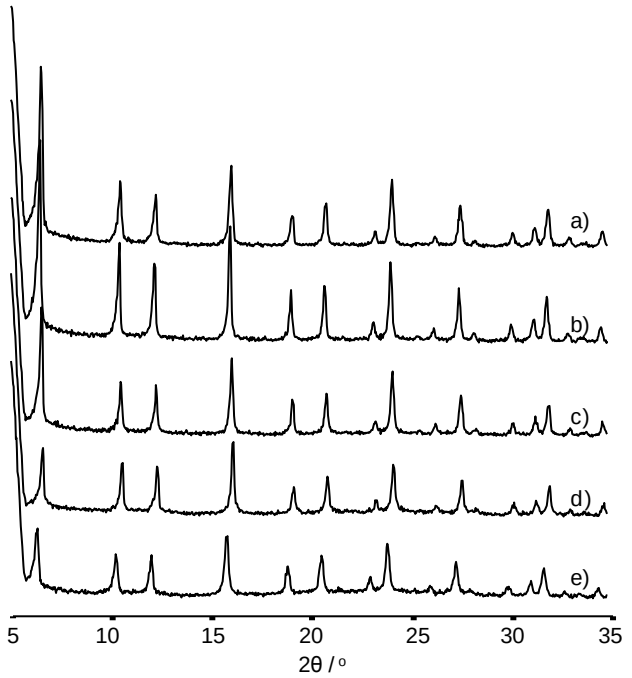

Figure A.4: X-ray diffractograms of zeolite Y5 treated at 200 °C: a) untreated, b) 1 h, c) 2 h, d) 4 h, e) 6 h.

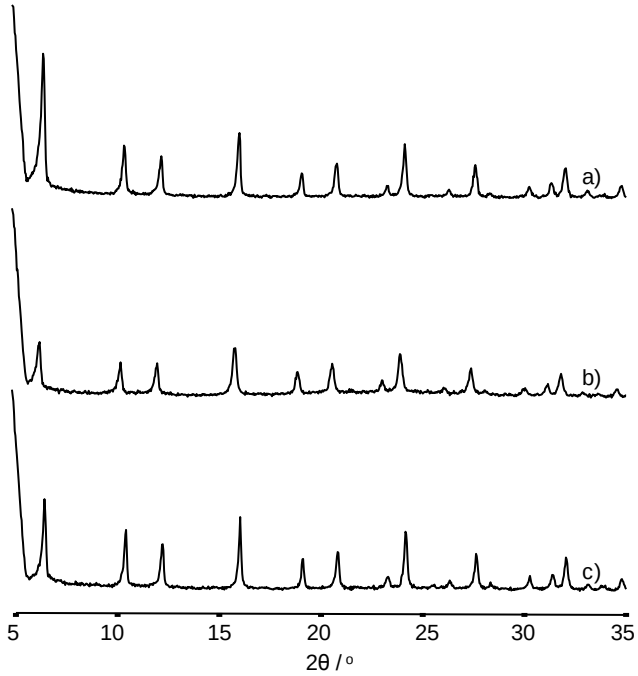

Figure A.5: X-ray diffractogram of zeolite Y5: a) untreated, b) treated at 200 °C for 6 h, c) treated at 150 °C for 6 h.

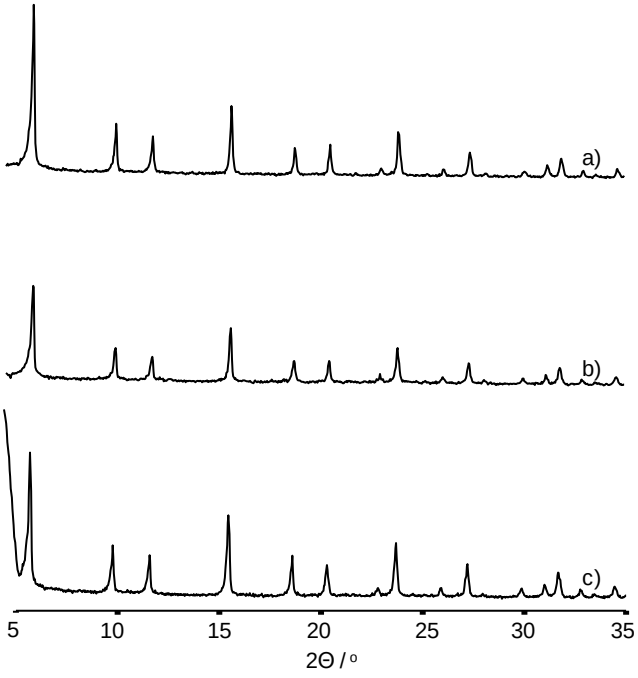

Figure A.6: X-ray diffractograms of zeolite LaY5: a) untreated, b) treated at 200 °C for 6 h, c) treated at 150 °C for 6 h.

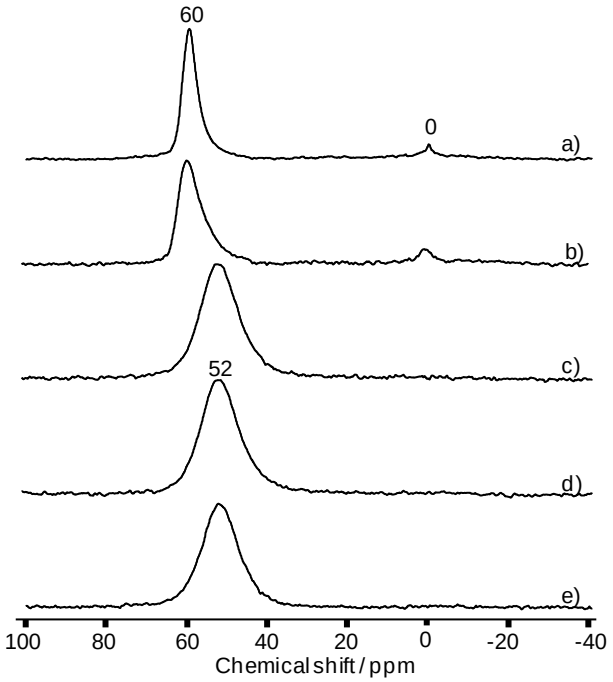

Figure A.7: ^{27}Al MAS NMR spectra of zeolite Y41 treated at 150 °C: a) untreated, b) 1 h, c) 2 h, d) 4 h, e) 6 h.

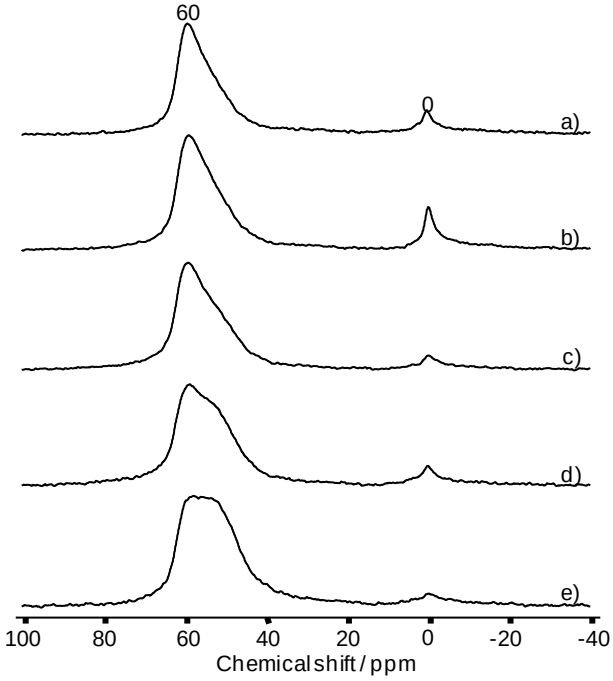

Figure A.8: ^{27}Al MAS NMR spectra of zeolite Y14 treated at 200 °C: a) untreated, b) 1 h, c) 2 h, d) 4 h, e) 6 h.

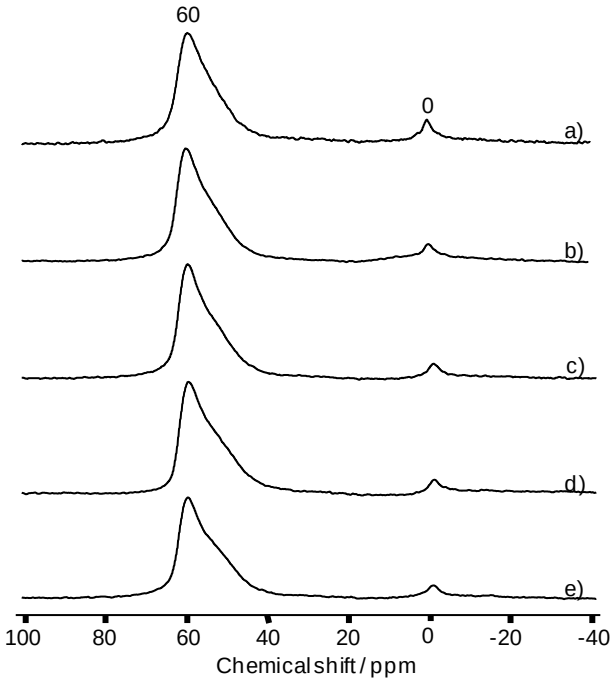

Figure A.9: ^{27}Al MAS NMR spectra of zeolite Y14 treated at 150 °C: a) untreated, b) 1 h, c) 2 h, d) 4 h, e) 6 h.

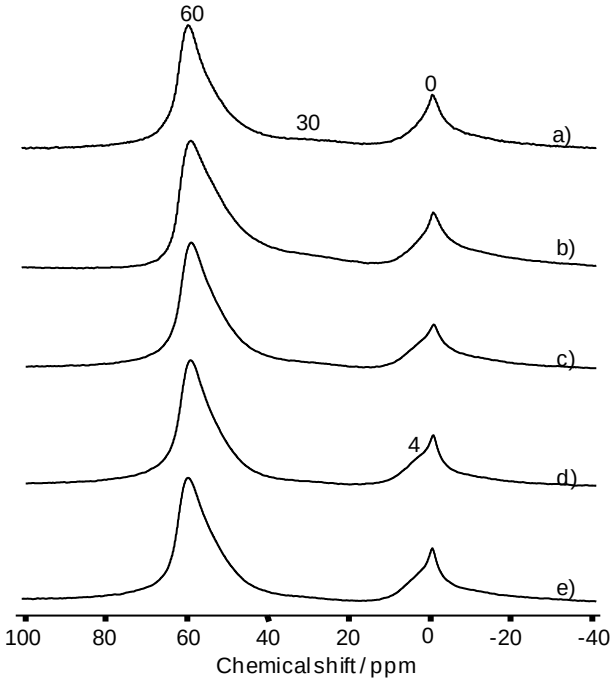

Figure A.10: ^{27}Al MAS NMR spectra of zeolite Y5 treated at 150 °C: a) untreated, b) 1 h, c) 2 h, d) 4 h, e) 6 h.

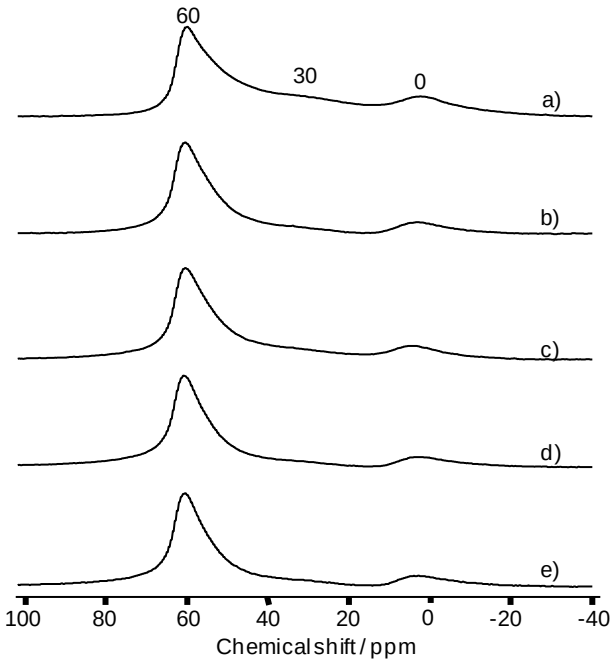

Figure A.11: ^{27}Al MAS NMR spectra of zeolite LaY5 treated at 150 °C: a) untreated, b) 1 h, c) 2 h, d) 4 h, e) 6 h.

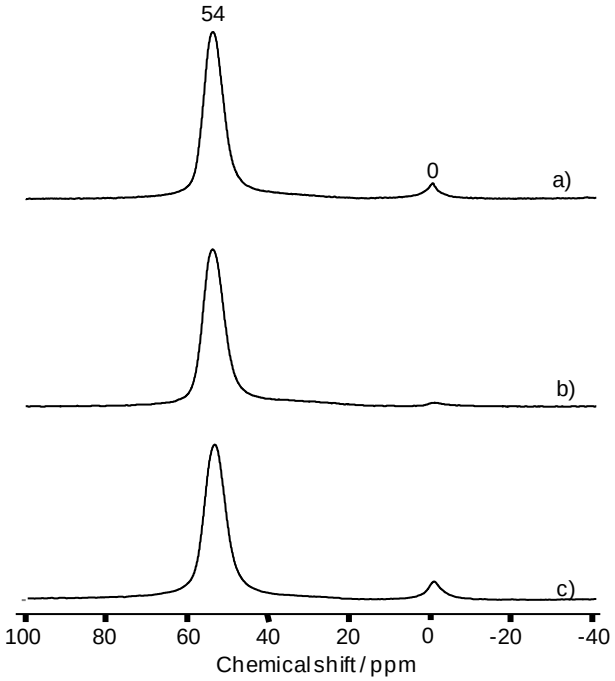

Figure A.12: ^{27}Al MAS NMR spectra of zeolite ZSM-5-15: a) untreated, b) treated at 200 °C for 6 h, c) treated at 150 °C for 6 h.

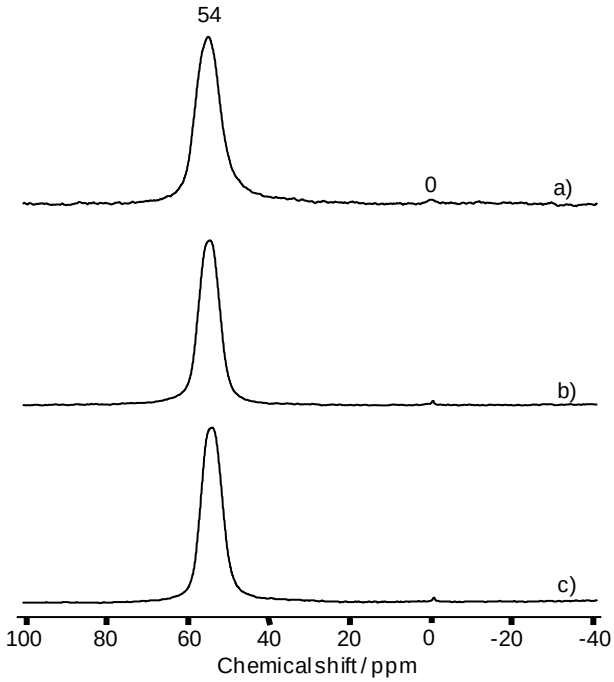

Figure A.13: ^{27}Al MAS NMR spectra of zeolite ZSM-5-40: a) untreated, b) treated at 200 °C for 6 h, c) treated at 150 °C for 6 h.

APPENDIX B

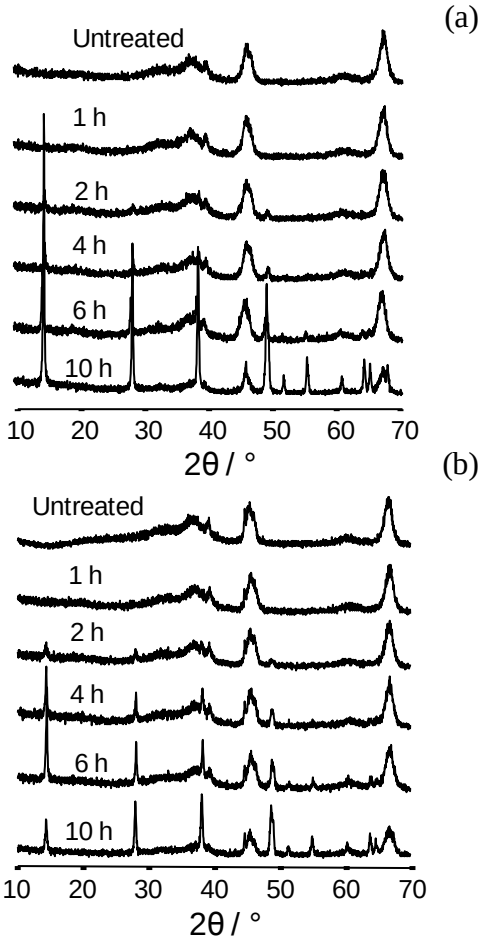

Figure B.1: X-ray diffractograms of 1 wt% Ni/γ-Al_2O_3 (a) and 1 wt% Pt/γ-Al_2O_3 (b) treated at 200 °C and saturation pressure for various durations.

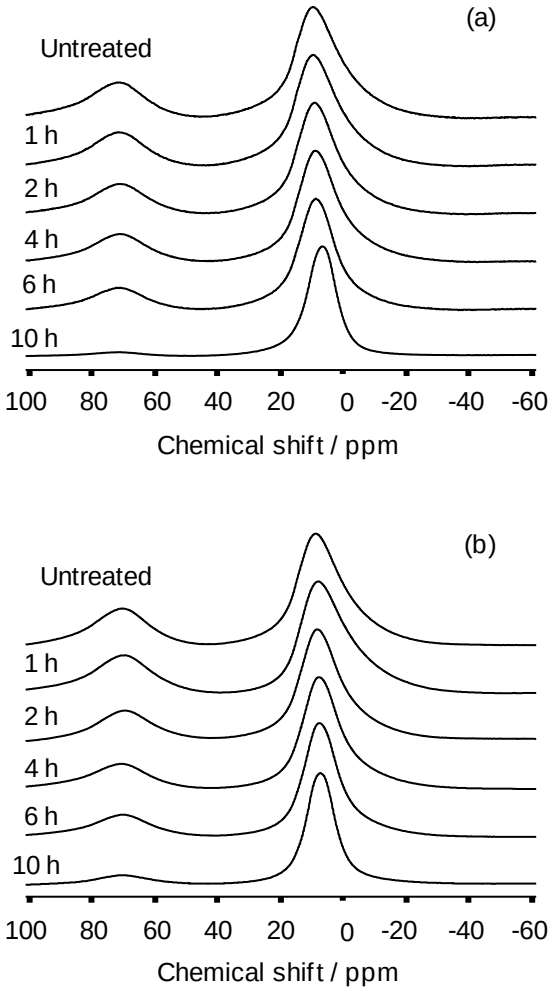

Figure B.2: ^{27}Al NMR spectra of 1 wt % Ni/γ-Al_2O_3 (a) and 1 wt% Pt/γ-Al_2O_3 (b) treated at 200 °C and saturation pressure for various durations.

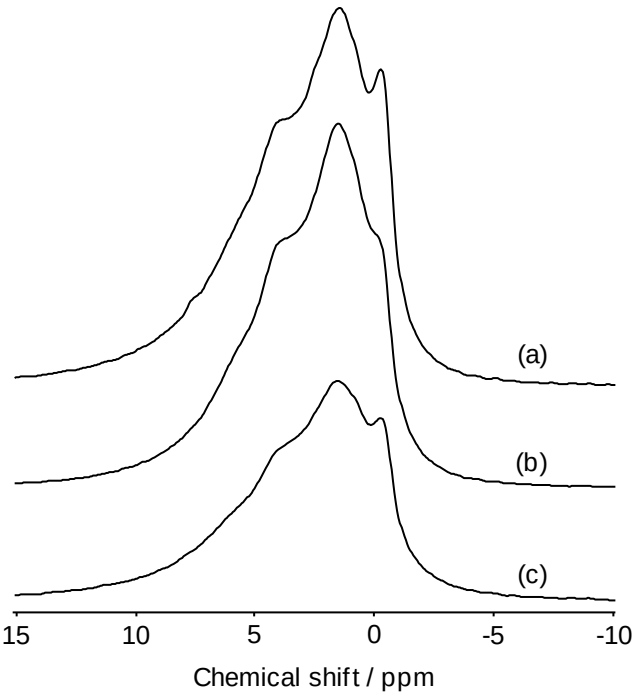

Figure B.3: Mass normalized ^{1}H MAS NMR spectra of untreated γ-Al_2O_3 (a), 1 wt% Pt/γ-Al_2O_3 (b), and 1 wt% Ni/γ-Al_2O_3 (c).

Thermogravimetric Analysis

Thermogravimetric analysis (TGA) experiments were performed on a TA Instruments SDT Q600 TGA. The sample temperature was ramped from room temperature to 800 °C at a rate of 10 K/min under a 100 mL/min flowrate of nitrogen sweep gas. An analysis of three repeats indicated an experimental standard deviation of +/- 1.5 %.

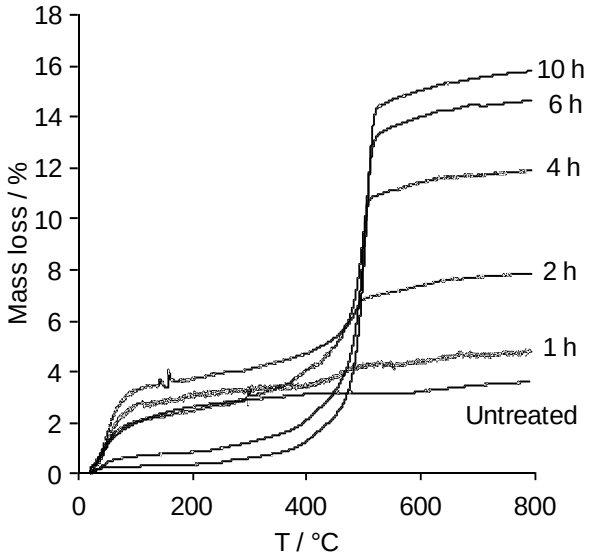

Figure B.4: Thermogravimetric analysis of untreated γ-Al_2O_3 and samples treated for various durations.

Table B.1: Comparison of % boehmite calculated from TGA method and ^{27}Al NMR MAS spectroscopy method.

Sample	% Mass loss for T > 210 °C	% Boehmite TGA *	% Boehmite ^{27}Al NMR MAS spectroscopy
γ-Al_2O_3 1 h	1.69	11.25	10.10
γ-Al_2O_3 2 h	4.10	27.31	27.28
γ-Al_2O_3 4 h	9.39	62.53	61.58
γ-Al_2O_3 6 h	13.79	91.83	92.44
γ-Al_2O_3 10 h	15.43	102.79	100

* Calculated boehmite fraction based on mass lass for T > 210 °C according to equation: % AlOOH = (% H_2O / M_{H2O}) x 2 x M_{AlOOH}

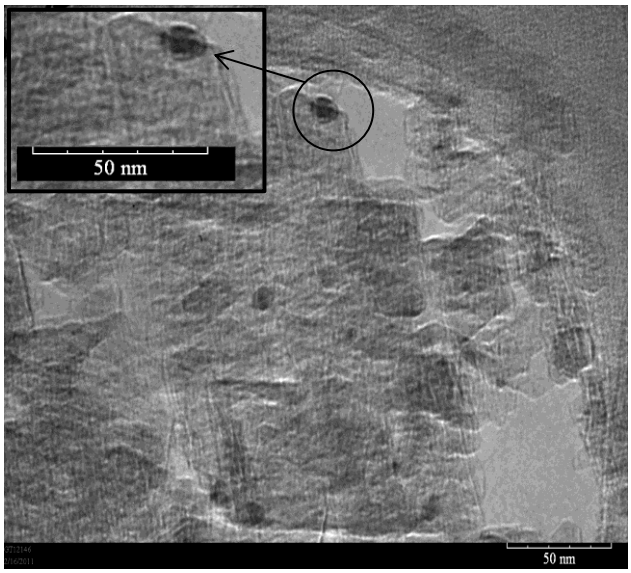

Figure B.5: TEM image 1 wt% Pt/ γ-Al_2O_3 treated for 10 h at 200 °C and saturation pressure.

APPENDIX C

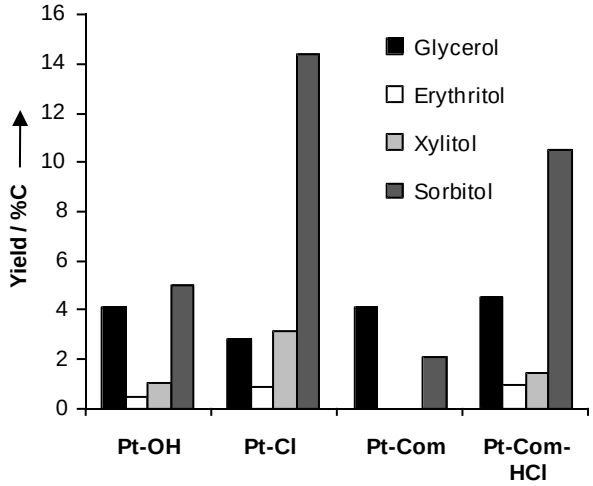

Figure C.1: Sugar alcohol yields from different catalysts after 4 h at 200 °C in 60 bar H_2. Catalyst loading of 0.5 g with 0.5 g of microcrystalline cellulose (Avicel) as reactant.

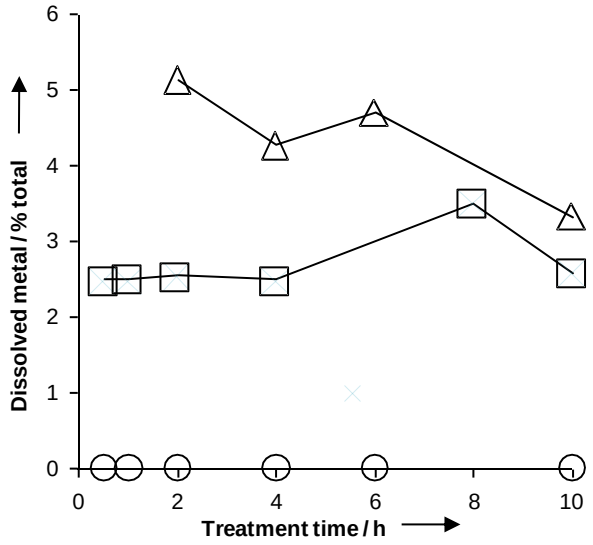

Figure C.2: Amount of leached platinum as a function of treatment time in liquid water at 200 °C under autogeneous pressure. Results are given as percentage of available metal based on wt% loading: ○ = Pt-OH, Δ = Pt-Cl, □ = Pt-Com.

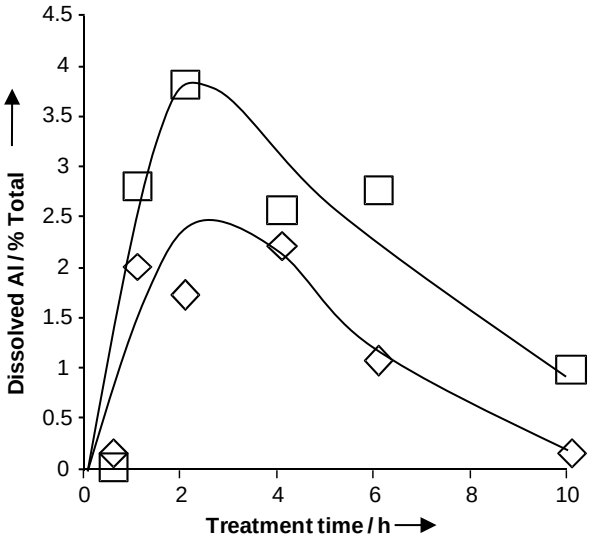

Figure C.3: Dissolved aluminum from Pt-Cl catalyst as a function of treatment time in liquid water at 200 °C with different atmospheres: □ = Pt-Cl in 60 bar H_2, ◊ = Pt-Cl in N_2.

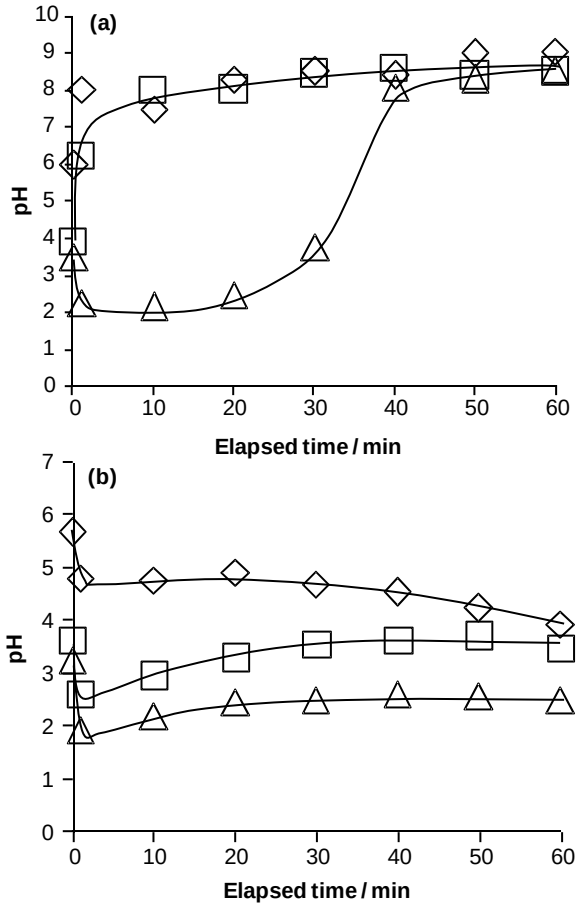

Figure C.4: pH measurements of Al^{3+} in water (a) and Al^{3+} in water with 500 mg of microcrystalline cellulose (b) over time at 200 °C and 60 bar H_2: □ = 30 ppm Al^{3+}, Δ = 360 ppm of Al^{3+}, ◊ = control (no aluminum salt).

The pH measurements were performed on liquid aliquots after cooling to room temperature. Upon addition of 30 ppm Al^{3+} and 360 ppm Al^{3+}, the pH of water dropped from 6.0 to values of 3.9 and 3.5, respectively (Figure C.4a). When heated to 200 °C, the pH of water increased, which is attributed to decreased solubility of carbon dioxide. The 30 ppm Al^{3+} solution exhibited similar behavior to the control when heated. In contrast, a markedly lower pH was observed for the first 40 minutes when 360 ppm Al^{3+} were present (Figure C.4a). In the presence of cellulose a lower pH was observed compared to pure water (Figure C.4b). This is likely caused by formation of organic acids in solution.

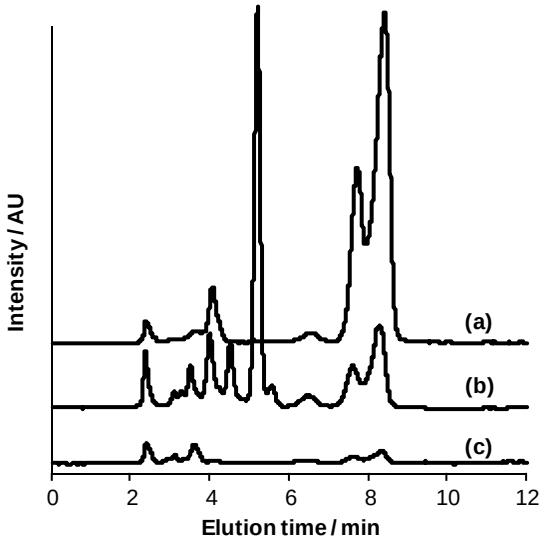

Figure C.5: HPLC chromatograms of microcrystalline cellulose hydrolysis experiments after 60 minutes elapsed time: (a) 30 ppm Al^{3+}, (b) 360 ppm Al^{3+}, (c) control (no aluminum salt).

The HPLC chromatograms show two glucose peaks around 8 min due to the α and β forms in solution. Trace (b) corresponds to the hydrolysis experiment in the presence of 360 ppm Al^{3+} and shows a large peak at ~ 5.2 ppm which is assigned to a glucose degradation product. Common glucose dehydration products were compared including: hydroxymethylfurfural, gluconic acid, itaconic acid, levulinic acid and levoglucosan. However, none of these compounds exhibited the same elution time. Therefore, this peak remains unidentified.

APPENDIX D

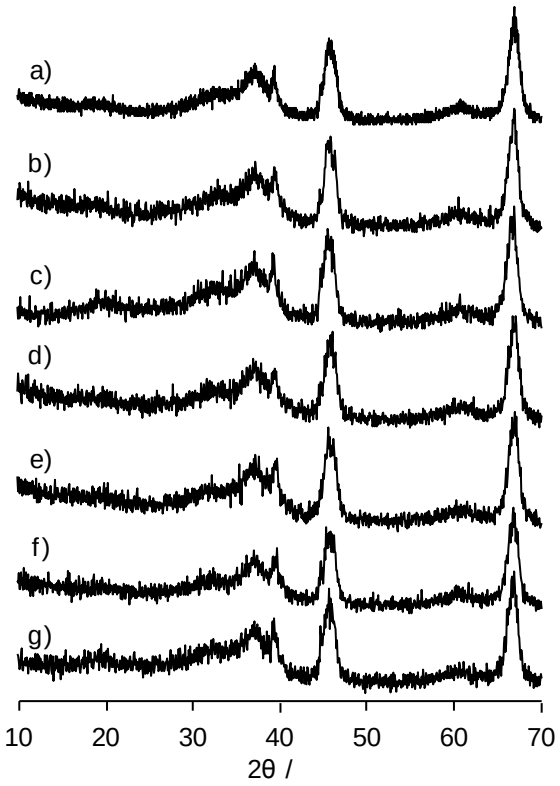

Figure D.1: X-ray diffractograms of Pt/γ-Al_2O_3 (a), PtAl-PDMS-10 (b), PtAl-PDMS-20 (c), PtAl-PDMS-40 (d), PtAl-TEOS-10 (e), PtAl-TEOS-20 (f), and PtAl-TEOS-40 (g).

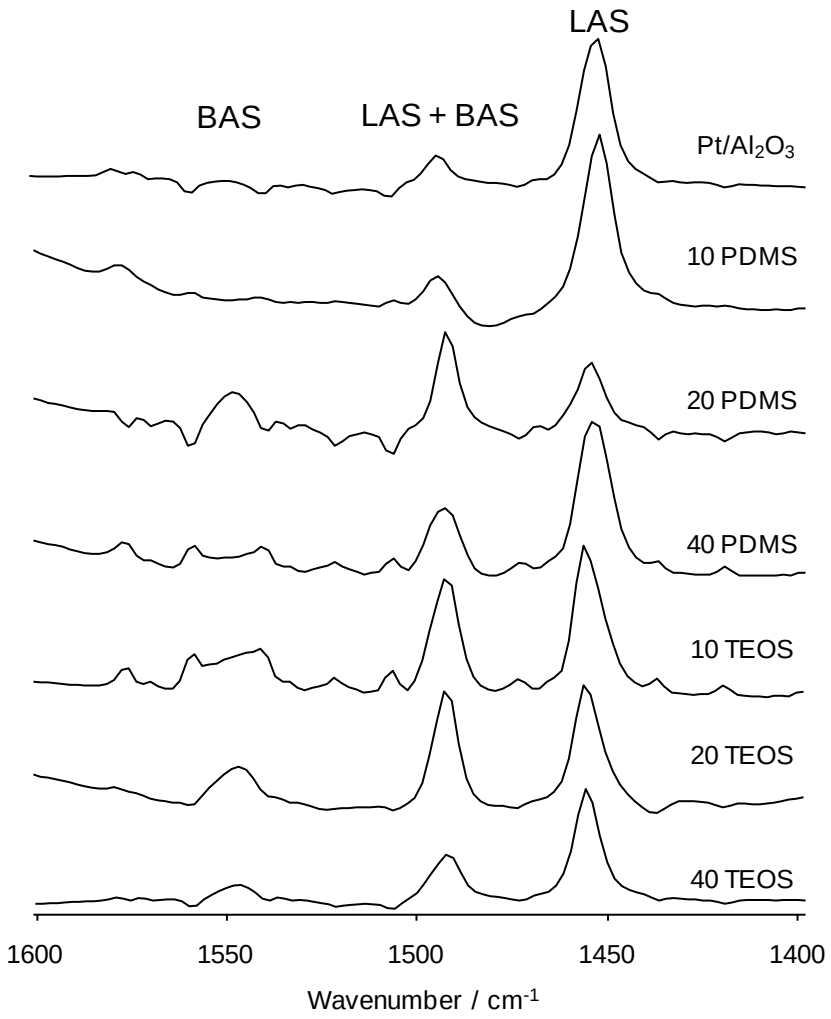

Figure D.2: IR spectra of all catalysts post pyridine adsorption.

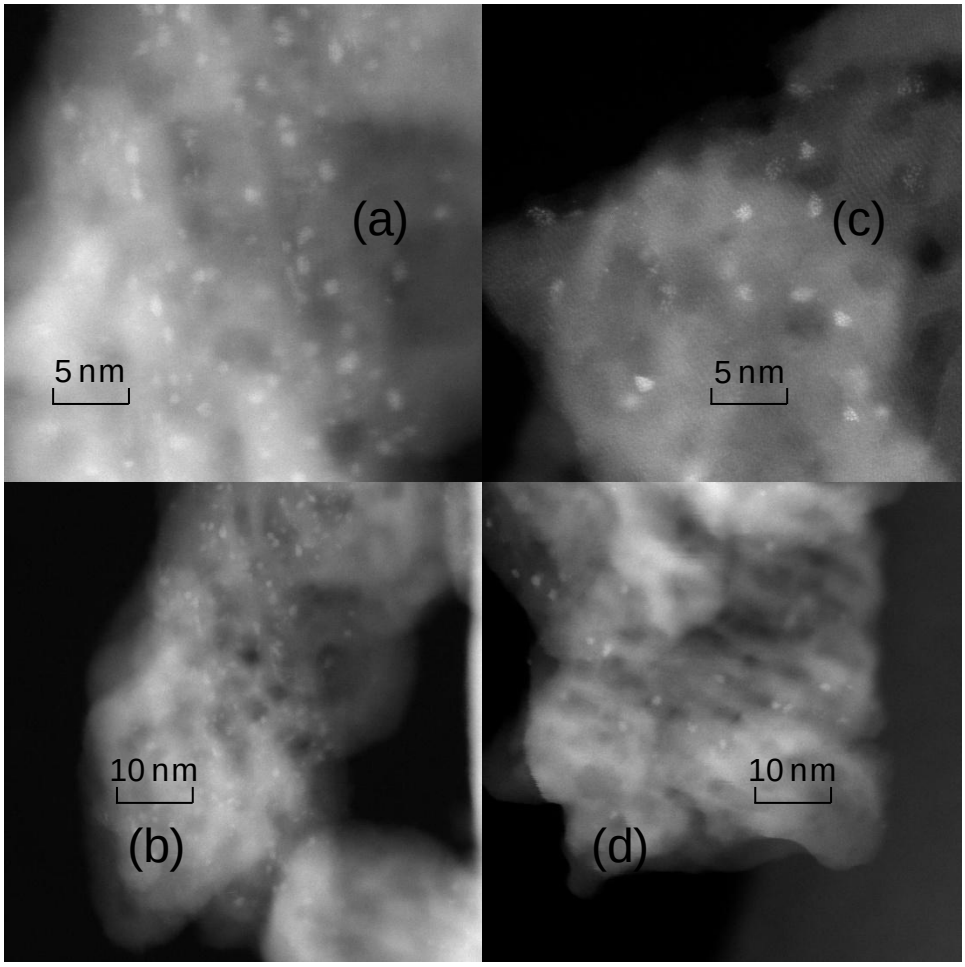

Figure D.3: HADF TEM micrographs of PtAl-PDMS-20 (a) and (b), and PtAl-PDMS-20 treated for 10 h in liquid water at 200 °C (c) and (d) at different magnifications.

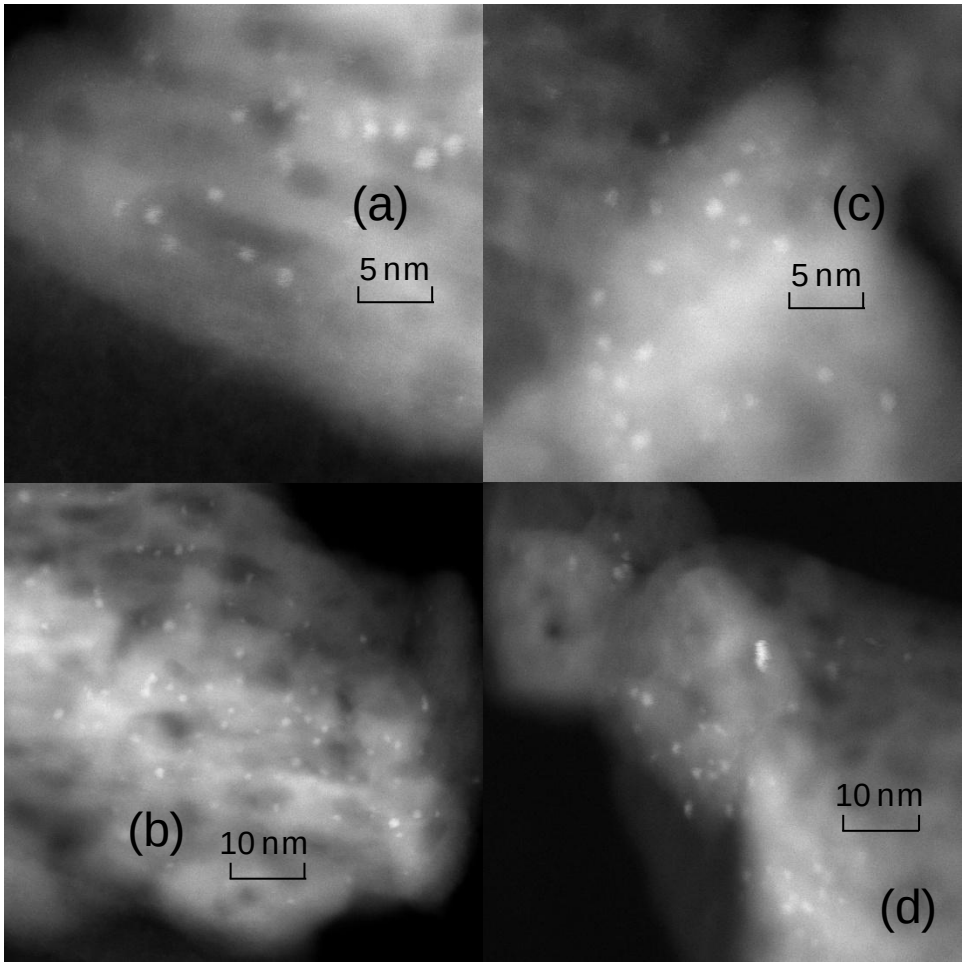

Figure D.4: HADF TEM micrographs of PtAl-TEOS-20 (a) and (b), and PtAl-TEOS-20 treated for 10 h in liquid water at 200 °C (c) and (d) at different magnifications.

VITA

Ryan Michael Ravenelle

Ryan was born on April 10, 1984 in San Jose, California to parents Michael Ravenelle and Sally Lednicky. In 1987, his family moved to Carson City, NV shortly after the birth of his sister Sarah. There he attended public school until graduating from Carson High School in 2002. While in high school, Ryan was afforded the opportunity to move to Spain for a semester exchange. He lived in the small town of Azkoitia in the northern Basque country and made lifelong friends with his host family, the Balbás family. After graduating high school, he made a short move to Reno, Nevada where he received a B.S. in Chemical Engineering from the University of Nevada in spring of 2006. He matriculated into the chemical engineering graduate program at Arizona State University in Tempe, Arizona in Fall 2006 where he studied until Spring 2009 at which point he transferred to Georgia Tech at the request of his advisor, Dr. John C. Crittenden, to complete the Ph.D. program in Chemical & Biomolecular Engineering. When he is not working on his research, Ryan enjoys pursuing outdoor activities and playing guitar in a rock and roll band.